

~~CONFIDENTIAL~~

RM A52A31

APR 30 1952



RESEARCH MEMORANDUM

WING LOAD DISTRIBUTION ON A SWEEP-WING AIRPLANE
IN FLIGHT AT MACH NUMBERS UP TO 1.11,
AND COMPARISON WITH THEORY

By L. Stewart Rolls and Frederick H. Matteson

Ames Aeronautical Laboratory
Moffett Field, Calif.

CLASSIFICATION CHANGED

UNCLASSIFIED

To _____

By authority of _____

Date _____

477 2-12-58

CLASSIFIED DOCUMENT

This material contains information affecting the National Defense of the United States within the meaning of the espionage laws, Title 18, U.S.C., Secs. 793 and 794, the transmission or revelation of which in any manner to an unauthorized person is prohibited by law.

NATIONAL ADVISORY COMMITTEE
FOR AERONAUTICS

WASHINGTON

April 14, 1952

NACA LIBRARY

~~CONFIDENTIAL~~

LANGLEY AERONAUTICAL LABORATORY
Langley Field, Va.



NATIONAL ADVISORY COMMITTEE FOR AERONAUTICS

RESEARCH MEMORANDUM

WING LOAD DISTRIBUTION ON A SWEEP-WING AIRPLANE
IN FLIGHT AT MACH NUMBERS UP TO 1.11,
AND COMPARISON WITH THEORY

By L. Stewart Rolls and Frederick H. Matteson

SUMMARY

Flight tests were conducted to determine the pressure distribution over the wing of a swept-wing jet-propelled airplane over the flight range of lift coefficients for Mach numbers up to 1.11.

At a constant normal-force coefficient the principal effect of increasing Mach number on the chordwise distribution of pressure was the reduction of the peak pressures near the leading edge. At subsonic speeds the wing was subject to stalling, which progressed inboard from the tip. The lift coefficient at which stall first occurred decreased with increasing Mach number to 0.3 at 0.9 Mach number. At supersonic speeds the lift effectiveness of the outer portion of the wing was very low. Tuft studies showed the flow to be separated over the trailing edge of this portion of the wing.

The spanwise distribution of additional loading at subsonic speeds was compared with that calculated by the Weissinger method. Up to the stall the agreement with theory was fair. The Weissinger method could be used to obtain a satisfactory approximation to the spanwise loading for structural design purposes. After the tip stalled the loading shifted inboard, departing well from the theoretical loading. At supersonic speeds the experimental spanwise distribution of loading was compared with that calculated from linearized supersonic theory. The agreement was not good because of the excessively low loading on the tip portion of the wing. In this case, the span load distribution calculated simply by the Weissinger method for Mach number of zero could be used for structural design purposes throughout the entire speed range.

Large trailing-edge loads, both up and down, were encountered particularly when the flow was separated.

CONFIDENTIAL

INTRODUCTION

Of prime importance in the design of aircraft for flight in the transonic speed range is the distribution of the airload on the wing, both from the standpoint of structural design and of stability and control.

Theories are available for calculating the spanwise distribution of load on swept wings at subsonic and at supersonic speeds. The applicability of these theories for the calculation of loading at transonic speeds must be checked both because of the possible violation of the assumptions underlying the theories and because of the powerful effects of boundary-layer shock-wave interaction.

Flight testing of aircraft at high altitude provides a means of determining loads at large values of the Reynolds number over a wide range of speed and angle of attack. The NACA has investigated wing loads in flight at high speed on straight-winged airplanes (references 1, 2, and 3). Tests of an F-86A airplane have provided an extension of these investigations to a 35° swept-back wing. The magnitude and distribution of forces were measured during transition from subsonic to supersonic speeds. These tests have enabled a check to be made on the applicability of inviscid, linearized theory for predicting for a comparatively thick wing the spanwise distribution of loading in the transonic region.

SYMBOLS

b wing span

c section chord in streamwise direction

c_{av} average chord $\left(\frac{S}{b}\right)$

\bar{c} mean aerodynamic chord $\left(\frac{2 \int_0^{b/2} c^2 dy}{S}\right)$

C_{Na} airplane normal-force coefficient

c_n section normal-force coefficient

c_{n70} normal-force coefficient of aft 30 percent of section chord

with respect to that length of chord

$$\left(\frac{\int_{0.7}^{1.0} (P_l - P_u) dx}{0.3c} \right)$$

M Mach number

M_n nominal Mach number for a run

P local pressure coefficient

P_l pressure coefficient on lower surface

P_u pressure coefficient on upper surface

R Reynolds number based on \bar{c}

S wing area

x,y,z Cartesian coordinates

x_c distance in streamwise direction from line of quarter chords to panel center of pressure

α angle of attack

α_u measured angle of attack uncorrected for wing upwash

$\delta_{a_{left}}$ left aileron angle

$\Delta\delta_{a_f}$ change due to floating in the average aileron angle from that at lowest lift coefficients

DESCRIPTION OF AIRPLANE

The tests reported herein were performed on the YF-86A airplane shown in figures 1 and 2. The quarter-chord line of the wing is swept back 35° , the aspect ratio is 4.79, and the taper ratio is 0.513. Other pertinent dimensions are presented in table I. The root airfoil section is a modified NACA 0012-64 normal to the wing quarter-chord line; a modified NACA 0011-64 section is used at the tip. Two degrees of wash-out are incorporated in the streamwise direction. Ordinates of the root and tip airfoils are given in table II.

Pressure measurements were made at 113 points distributed along 5 spanwise stations on the left wing panel. The locations of the stations are shown in figure 3. The positions of the orifices at the five stations are given in table III.

The wing slat was locked in the closed position for all of the tests.

Instrumentation and Accuracy

The pressure instrumentation, including the orifices, pressure cells, and recording system, was installed by North American Aviation, Inc., for a separate investigation on contract with the U. S. Air Force. This instrumentation was supplemented during the present investigation by the installation of an NACA recording accelerometer and an NACA airspeed altimeter. The airspeed altimeter was connected to a 10-foot nose boom. The calibration of a similar boom is presented in reference 4. Correlation between the various instruments was obtained by the use of a chronometric timer.

Each orifice (0.050-inch diameter) was connected directly to an absolute pressure transducer of the range 2 to 15 pounds per square inch absolute. The use of these pressure transducers permitted the installing of the transducer relatively close to the orifice, thus minimizing the inaccuracy due to lag in the pressure lines. The electric output from the pressure transducers was recorded on multichannel oscillographs. To enable the data from all the transducers to be recorded on the available channels, it was necessary to duplex the records on the oscillographs. The system enabled a maximum of 144 records to be recorded every 0.16 second.

The pressure distributions are subject to considerable limitation since, with 24 orifices as the maximum in any spanwise station, much weight must be given to each orifice. Thus when an orifice was not operating properly, the faired chordwise distribution could be somewhat in error.

Measurements of wing bending in flight were made to assess its importance in this investigation. The deflections were found to be small. The effects of bending and torsion on the load distributions were calculated and were found to be negligible.

The accuracy has been estimated as follows:

Mach number	± 0.01
Pressure altitude	± 150 feet
Pressure coefficient	$\pm \frac{20 \text{ lb/ft}^2}{q}$
Aileron deflection	$\pm 0.25^\circ$

Tests

These data were obtained at the lower Mach numbers in progressively tightening turns at as constant airspeed as possible. At the higher Mach numbers it was necessary to make either diving turns or pull-ups to obtain data through as wide a lift-coefficient range as possible and the consequent variation in the Mach number was greater than at low speeds. Data were particularly difficult to get in the $M = 0.92$ to $M = 0.98$ range because of poorer stability and control characteristics, especially at high lift coefficients.

The nominal altitude for these tests was 35,000 feet, while in actual operation the altitude varied from 32,400 to 37,200 feet.

The range of Mach numbers and normal force coefficients attained is shown in figure 4. The Reynolds number based on the mean aerodynamic chord plotted versus Mach number is shown in figure 5 for standard conditions for the altitude range of the tests.

RESULTS AND DISCUSSION

Section Characteristics

Oblique drawings of the pressure distributions on the wing are shown for different values of C_{N_a} for nominal Mach numbers¹ of 0.70, 0.87, 0.90, and 1.02 in figure 6. The data at these four Mach numbers may be considered to be representative for the flight range and will be analyzed subsequently. In addition, some data at $M_n = 0.97$ and at $M_n = 1.11$ are included.

¹The nominal Mach numbers in this and other figures where the C_{N_a} varies are those representative of the run. The variation of M ranged from ± 0.01 for $M_n = 0.70$ to ± 0.04 for $M_n = 1.02$.

Rather large peak pressures are observed near the leading edge at the lowest Mach number. The sharpness of the nose peak in the pressure distributions over the upper surface decreases through the transonic range so that virtually no nose peak exists at supersonic speeds. In general, the magnitude of the negative pressures over the afterportion of the wing lower surface increases gradually from the inboard to outboard stations.

The integrated pressure distributions for the five spanwise stations have been plotted in terms of loading coefficient, c_n/c_{ay} , against uncorrected angle of attack in figure 7. The section normal-force curves at each Mach number indicate initial stalling of the outboard stations with subsequent progression inboard. The change in section normal force at the stall is gradual and the normal force often increases even after an initial break at stations 4 and 5. There is no perceptible increase in normal-force-curve slope for the inboard sections after the tip stalls.

The angle of attack at which the tip stalls decreases with increasing Mach number. Similarly, the angle of attack for which buffeting occurs decreases with increasing Mach number. The buffet boundary has been drawn on figure 7. The buffet boundary as defined herein is the flight condition where buffeting of $\pm 0.03g$ is recorded at the airplane center of gravity. At a Mach number of 0.70 the local lift loss is evident before buffeting is detected, but occurs almost simultaneously with buffeting at $M_n = 0.87$ and 0.90. The tip stall at supersonic speeds did not produce noticeable buffeting. For Mach numbers of 0.90 and below the upper surface pressures over the afterportion of the wing diminish toward the tip at the lower values of C_{N_a} but tend to level out without pressure recovery when the flow separates at the higher values of C_{N_a} . The separation was confirmed and its progression studied by means of tufts glued to the wing. Photographs of tufts showing stall progression at $M = 0.9$ are presented in figure 8. The photographs were taken with a movie camera pointed aft approximately parallel to the wing from the cockpit canopy. Initial separation takes place on the aileron and progresses forward, with the forward boundary of the separated area approximately normal to the free stream, until the flow over the entire wing is separated.

The upper surface pressures at supersonic speeds are quite uniform and the lower surface pressures become increasingly negative toward the tip, causing the total lift to decrease toward the tip. The pressure recovery at the outer station is generally poor at the higher Mach numbers.

Load Distribution

Span load distribution.- In this portion of the report the distribution of the additional loading only will be considered. To obtain the additional loading, curves of station normal-force coefficient versus airplane normal-force coefficient were plotted. Considering the value of station normal-force coefficient at zero airplane normal-force coefficient as a basic section normal-force coefficient, these values were subtracted from the values at other C_{N_a} 's. If these differences are plotted against spanwise station the resultant loading is termed the additional loading. This procedure eliminates the errors associated with the shift of instrument zeros during flight and removes the basic loading due to wing washout.

Curves of spanwise distribution of additional loading are plotted in figure 9 for the four Mach numbers discussed previously. The Weissinger method (reference 5) has been used to compute the theoretical span load distribution for comparison with experiment at Mach numbers below 1.0. At supersonic speeds the method of reference 6 has been used. The comparisons have been made on the basis of equal loading on the outer 90 percent of the span to obviate extrapolation to the fuselage center line. This portion of the wing has been termed the panel. No correction to the theoretical results has been made for the effect of the fuselage.

The comparison of the experimental and theoretical loadings at $M_n = 0.70$ is shown in figures 9(a) to 9(d). Since the ailerons were free to deflect somewhat under air load, a span-loading curve showing the effect of aileron floating, calculated according to the method of reference 7, is included. It is seen that for normal-force coefficients of 0.2 and 0.4 the tips carry slightly more load than predicted by theory. At $C_{N_a} = 0.6$ the loading is seen to be moving inboard. As the C_{N_a} increases to 0.8 the separation over the tip causes loss of lift, thereby leading to relatively high inboard loading.

The effect of aileron floating is small at the lower lift coefficients and, although larger at the higher lift coefficients, it does not account for the difference between theory and experiment. Therefore the correction in the theoretical loading for ailerons deflected has been omitted in the comparisons at other Mach numbers although the aileron deflections have been noted.

The trends observed for $M_n = 0.7$ are seen also at $M_n = 0.87$ and 0.90. No explanation is offered for the consistently low loadings at station 2.

On the basis of the comparisons of theory and experiment at subsonic speeds, it may be concluded that for structural design purposes the Weissinger theory for ailerons undeflected provides a reasonable estimate

of the spanwise distribution of loading up to the lift coefficient at which local stalling occurs. Following the stall, the loading shifts inboard so that the theory would be conservative for loads estimation.

The agreement between theory and experiment at the low supersonic Mach numbers of these tests would not be expected to be very close because the variation in the local Mach number over the wing would alter considerably the assumed position of the Mach lines for the theory. Also as in the comparison at high subsonic speeds, the effects of boundary-layer shock-wave interaction can be very large. It is not surprising then that, for the supersonic Mach number range of these tests, the agreement between theory and experiment is not good. The loading over the outer half of the wing is lower than that predicted by theory at $C_{N_a} = 0.2, 0.4, \text{ and } 0.5$. To an even greater degree than at subsonic speeds, the comparison shows the theory to give conservative results for loads estimation on this particular wing.

In order to show the variation in the theoretical span load distribution through the transonic speed range, span load distributions have been drawn for three Mach numbers in figure 10(a). The method of reference 5 was used at 0.95 Mach number. The method of reference 6 was used for Mach numbers of 1.02 and 1.20. Because the span load distributions for Mach numbers up to 0.95 are quite similar to that at $M = 0.95$, they have been omitted for clarity. The center of loading is seen to move outboard through the transonic range. From the theoretical results an increase in the bending stresses would be predicted for a given wing load as the Mach number increases through this range. To show the variation with Mach number in the loading at a given angle of attack as calculated by the two theories, the loading at three spanwise stations has been plotted against Mach number in figure 10(b). The variation in the loading is regular. The loading on the two inboard stations increases to a maximum at about $M = 1.01$. For the 0.8 semispan station, however, the loading continues to increase up to about $M = 1.13$.

Chordwise loading.- The theory of reference 6 provides not only the spanwise loading but the complete surface loading. Therefore a comparison of experiment and theory can be made for the chordwise loading in addition to the spanwise loading at supersonic speeds. The theoretical results have been plotted in oblique form in figure 11 for $M = 1.02, 1.05, 1.10, \text{ and } 1.20$. The transition from an almost constant loading at the wing root to a predominantly leading-edge loading at the tip is gradual. The discontinuities in slope of the loading curves occur along the Mach lines originating at the leading edge of the tip or the trailing edge of the root, or their reflections. The decremental loadings due to the tip and the trailing edge are additive and produce negative lifting loads over the afterportions of the tip. The predominant decremental load is from the tip and its magnitude can be seen in absence of the trailing-edge decremental loading in figure 11(d) for $M = 1.20$.

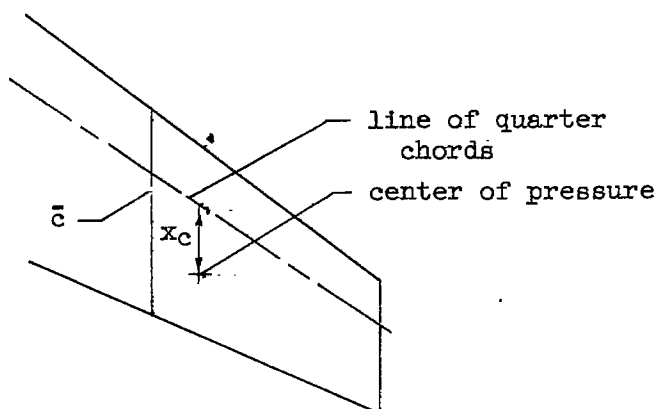
Experimental distributions have been included for $C_{N_a} = 0.2$ at $M = 1.02, 1.05, \text{ and } 1.10$. The general trends indicated by the theory are seen in the experimental data. The chordwise pressure distribution changes from the Ackeret type at the root to the subsonic peaked type at the tip. Striking similarity is seen in the tip effect although, possibly because of the downward floating of the aileron and flow separation, the measured pressures exceed those predicted from theory. This negative loading with the absence of the high predicted leading-edge pressures accounts for the difference in the theoretical and experimental spanwise load distributions.

Panel loads.- The pressures over the outboard 90-percent semispan have been integrated to determine the variation of the magnitude of the load and the lateral and chordwise position of the center of pressure on that portion of the wing outboard of the fuselage. The integrated pressures over the outer 90-percent semispan, when referred to the area of half the wing, yield a panel normal-force coefficient. The airplane normal-force coefficient was obtained from records of a normal accelerometer. Comparisons of these two coefficients have been made (fig. 12) at several values of C_{N_a} from Mach numbers of 0.7 to 1.11. Measurements of tail loads made during the tests reported in reference 8 showed them to be consistently small with respect to the wing loads through most of the lift-coefficient range. The changes in loading shown are then due primarily to the relative loadings of the wing and the fuselage. The portion of the load carried by the wing decreases as the Mach number increases until a low point is reached in the vicinity of 0.9 Mach number, whereupon an increase occurs with increasing Mach number.

The variation of the position of the lateral center of pressure with Mach number for different values of normal-force coefficient is shown in figure 13. The center of pressure remains essentially fixed for a given value of C_{N_a} up to a Mach number of about 0.87. At this point the tip portions show a loss in lift which shifts the center of pressure inboard. As the Mach number increases above 1.0 the loading begins to shift outboard again as exemplified at $C_{N_a} = 0.2$.

Theoretical results have been included for comparison in figure 13. The lateral center at pressure at supersonic speeds is inboard of that at subsonic speeds in direct contrast to the results shown by theory. This suggests that for structural design purposes the use of the subsonic spanwise distribution of loading obtained by the Weissinger method would provide a conservative estimate of loads at supersonic speeds.

The chordwise position of the center of load measured from the line of quarter chords in mean aerodynamic chords is termed the chordwise center of pressure (see sketch).



The variation in the position of the chordwise center of pressure with Mach number is shown in figure 14. At the lower normal-force coefficients the center of pressure progresses from the quarter chord at 0.7 Mach number to about 27 percent at 0.87 Mach number. At the higher normal-force coefficients the center of pressure at 0.7 Mach number is farther aft and progresses still farther aft with increasing Mach number. The data for $C_{N_a} = 0.2$ and $C_{N_a} = 0.4$ show a forward shift in the $M = 0.87$ to 0.92 region with a subsequent rearward movement. The forward shift is not seen at the higher values of C_{N_a} . The quarter-chord-line position of the chordwise center of pressure assumed in the Weissinger theory is in reasonable agreement with experiment at the lower lift coefficients and Mach numbers.

The panel load and the spanwise and chordwise positions of the center of pressure presented are sufficient to define the panel pitching moment. Analysis of the pitching-moment data is facilitated by breaking down the total wing pitching moment into the pitching moment associated with the lateral and chordwise shifts in loading. Data are presented (fig. 15) for 0.87 Mach number through the C_{N_a} range. The pitching moment due to change in chordwise center of pressure varies smoothly, becoming increasingly negative with increasing values of C_{N_a} . The pitching moment due to change in the lateral center of pressure, however, becomes unstable at about $0.5 C_{N_a}$ thus causing the unstable wing pitching-moment variation. That this contribution is the major factor causing longitudinal instability of the airplane is shown in reference 8.

Trailing-Edge Loads

Excessive upfloating of the flaps and ailerons, as well as some structural damage, has indicated that excessive trailing-edge loads were being encountered.

The integral of the pressure distribution over the aft 30 percent of the wing gives a measure of the average differential pressure over this part of the wing. Figure 16 presents data for the four Mach numbers discussed previously. At $M_n = 0.7$ the loads are positive and increase over the different stations with increasing values of C_{N_a} . The center-section trailing-edge loads are higher than those outboard. The slope of the trailing-edge load versus C_{N_a} curves is not constant but tends to increase at all stations at the higher values of C_{N_a} . At 0.87 Mach number the outer two stations exhibit negative loads at most of the normal-force coefficients. The loading at all stations increases at the highest normal-force coefficients. The loading variations at $M_n = 0.90$ are similar to those at $M_n = 0.87$ except that the loads begin to increase at lower values of C_{N_a} . The loading over the root reaches a value of $0.76q$ which is very high and considerably in excess of the value of $0.40q$ recommended for design purposes in reference 2. At $M_n = 1.02$ the trailing-edge loading is low at the lower values of C_{N_a} . Only the inner two stations exhibit much increase in loading, such as was shown at the lower speeds. One item of departure is the negative loading increase with C_{N_a} for station 5. This behavior has been confirmed by a number of runs at these high Mach numbers.

The variation of aileron floating angle with C_{N_a} is of interest both as an indication of loads over the outer aft portion of the wing² and as to its effect on the load distribution of the wing as a whole. Figure 17 shows the difference in the floating angle at various values of C_{N_a} from that at $C_{N_a} = 0$ (or the lower limit C_{N_a} of the run) plotted with the $\Delta\delta_{a_f} = 0$ point coinciding with the nominal Mach number of the run. Figure 17 indicates two different conditions in which trailing-edge loads are significantly large. At higher subsonic speeds at high lift coefficients large uploads were encountered. At supersonic speeds at the higher lift coefficients large downloads were encountered. Figure 16(d) shows this download occurred in the region of station 5. In the Mach number range from 0.75 to 0.92 little or no upfloating occurred at the lower C_{N_a} 's up to a point where upfloating increased rapidly with increasing C_{N_a} . Tuft photographs showed that the aileron

²Calibration of the lateral control system has shown that 1° of float represents 5600 inch-pounds hinge moment.

upfloat followed separation over the aileron. For further comparison, the buffet boundary has been included. The buffet boundary lies above the normal-force coefficient for start of rapid upfloat. This comparison is similar to that made in the discussion of figure 7 for section loading, indicating that noticeable separation can exist without buffeting being measured at the center of gravity.

The downfloat at supersonic speeds and at Mach numbers slightly below 1.0 occurs very abruptly. It is characterized by a slight upfloat prior to downfloating and by a reduction in downfloating with increasing C_{Na} above the break. The cause of the rapid downfloat can again be seen from tufts. Figure 18 shows tuft pictures just prior to and just following the rapid downfloat. The tufts have turned from the streamwise direction and point toward the tip. This is indicative of separation over the upper surface of the aileron. The separation is not characterized by a rapid oscillating motion of the tufts and buffeting is not experienced.

CONCLUSIONS

Tests of a 35° swept-wing F-86A airplane in flight at Mach numbers up to 1.11 have indicated the following conclusions:

1. At subsonic speeds the spanwise distribution of loading was adequately predicted by the Weissinger method up to the buffet boundary. At supersonic speeds the center of loading was inboard from that predicted from either supersonic or subsonic theory. Therefore, for structural design purposes, the use of the subsonic spanwise distribution of loading obtained by the Weissinger method would provide a conservative estimate of loads at supersonic speeds.
2. For normal-force coefficients above the buffet boundary the measured load distribution departed from the theoretical, the amount depending upon the Mach number; however, the theoretical distribution was still conservative for loads estimation.
3. Separation of the flow at the outboard stations occurred before buffeting was detected at the center of gravity of the airplane.
4. Significantly large uploads (about $0.8q$ at $M = 0.90$) and downloads (above $M = 0.97$) over the trailing edge of the wing were encountered, particularly when the flow was separated.

Ames Aeronautical Laboratory
National Advisory Committee for Aeronautics
Moffett Field, Calif.

~~CONFIDENTIAL~~

REFERENCES

1. Clousing, Lawrence A., Turner, William N., and Rolls, L. Stewart: Measurements in Flight of the Pressure Distribution on the Right Wing of a Pursuit-Type Airplane at Several Values of Mach Number. NACA Rep. 859, 1946. (Formerly NACA ARR 4K09)
2. Brown, Harvey H., and Clousing, Lawrence A.: Wing Pressure-Distribution Measurements up to 0.866 Mach Number in Flight on a Jet-Propelled Airplane. NACA TN 1181, 1947.
3. Rolls, L. Stewart: Comparison Between Flight-Measured and Calculated Span Load Distribution at High Mach Numbers. NACA RM A7G17, 1947.
4. Thompson, Jim Rogers, Bray, Richard S., and Cooper, George E.: Flight Calibration of Four Airspeed Systems on a Swept-Wing Airplane at Mach Numbers Up to 1.04 by the NACA Radar-Phototheodolite Method. NACA RM A50H24, 1950.
5. DeYoung, John, and Harper, Charles W.: Theoretical Symmetric Span Loading at Subsonic Speeds for Wings Having Arbitrary Plan Form. NACA Rep. 921, 1948.
6. Cohen, Doris: Formulas for the Supersonic Loading, Lift, and Drag of Flat Swept-Back Wings with Leading Edges Behind the Mach Lines. NACA Rep. 1050, 1951. (Formerly NACA TN's 1555, 1991, and 2093)
7. DeYoung, John: Theoretical Symmetric Span Loading Due to Flap Deflection for Wings of Arbitrary Plan Form at Subsonic Speeds. NACA TN 2278, 1951.
8. Anderson, Seth B., and Bray, Richard S.: A Flight Evaluation of the Longitudinal Stability Characteristics Associated With the Pitch-Up of a Swept-Wing Airplane in Maneuvering Flight at Transonic Speeds. NACA RM A51I12, 1951.

TABLE I.- PERTINENT AIRPLANE DIMENSIONS

Wing data	
Total wing area (includes flaps, slats, and 49.92 sq ft covered by fuselage)	287.90 sq ft
Span	37.12 ft
Aspect ratio	4.785
Taper ratio	0.5131
Dihedral angle	3°00'
Mean aerodynamic chord	97.03 in.
Sweepback of the 25-percent element	35°13'31.4"
Incidence of the root chord	1°00'
Incidence of the tip chord	-1°00'
Aileron data (data for one aileron only)	
Area (aft of hinge line including tab)	18.60 sq ft
Balance area (including 5 percent of fabric seal = 0.32 sq ft)	4.67 sq ft
Span (equivalent)	110.03 in.
Aileron deflection	14° up, 14° down
Fuselage data	
Width at wing juncture	60.0 in.
Length	408.4 in.

NACA


TABLE II.- ORDINATES OF ROOT AND TIP AIRFOILS

x percent chord	Root 0012-64 mod	Tip 0011-64 mod
	z percent chord	z percent chord
0	0	0
1.25	1.77	1.59
2.50	2.40	2.16
5.00	3.20	2.86
7.50	3.73	3.34
10.00	4.14	3.70
15.00	4.74	4.32
20.00	5.15	4.60
30.00	5.65	5.02
40.00	5.78	5.09
50.00	5.54	4.83
60.00	4.96	4.23
70.00	4.04	3.32
80.00	2.80	2.22
90.00	1.41	1.11
95.00	0.71	0.55
100.00	0	0
L.E. radius, percent chord	1.53	1.24

NACA

TABLE III.- PRESSURE-SURVEY ORIFICE LOCATION
[Locations given in percent chord]

Station 1		Station 2		Station 3		Station 4		Station 5	
Orifice	Location	Orifice	Location	Orifice	Location	Orifice	Location	Orifice	Location
1 U	2.4	1 U	0.06	1 U	0.2	1 U	0.1	1 U	0.2
2 U	5.1	2 U	2.7	2 U	3.1	2 U	2.7	2 U	2.7
3 U	8.3	3 U	8.2	3 U	5.9	3 U	5.4	3 U	9.0
4 U	12.9	4 U	17.1	4 U	9.6	4 U	10.7	4 U	17.6
5 U	24.1	5 U	22.3	5 U	14.2	5 U	15.9	5 U	30.9
6 U	33.8	6 U	31.4	6 U	23.3	6 U	26.7	6 U	50.0
7 U	39.0	7 U	41.7	7 U	37.4	7 U	39.6	7 U	59.0
8 U	44.1	8 U	51.3	8 U	49.5	8 U	53.7	8 U	72.7
9 U	48.2	9 U	60.8	9 U	64.2	9 U	58.5	9 U	82.4
10 U	53.6	10 U	70.1	10 U	79.8	10 U	73.2	10 U	92.2
11 U	58.0	11 U	81.5	11 U	87.7	11 U	80.2	11 U	91.4
12 U	64.0	12 U	85.4	12 U	95.6	12 U	87.3	12 U	82.4
13 U	75.4	13 U	90.2	13 L	94.8	13 U	94.3	13 L	72.7
14 U	85.6	14 U	95.8	14 L	87.0	14 L	93.9	14 L	59.7
15 U	91.5	15 L	95.3	15 L	80.6	15 L	87.3	15 L	50.0
16 U	97.4	16 L	88.7	16 L	55.1	16 L	80.3	16 L	30.9
17 L	90.0	17 L	82.1	17 L	45.5	17 L	73.2	17 L	18.9
18 L	66.4	18 L	76.1	18 L	32.0	18 L	53.7	18 L	2.1
19 L	57.8	19 L	65.6	19 L	11.7	19 L	39.6	Chord length, 72.06 in.	
20 L	43.9	20 L	51.8	20 L	1.6	20 L	26.6		
21 L	28.5	21 L	38.4	Chord length, 96.09 in.		21 L	12.2		
22 L	18.2	22 L	22.1			22 L	1.8		
23 L	10.3	23 L	11.0	Chord length, 85.29 in.		Chord length, 85.29 in.			
24 L	5.1	24 L	1.4						
Chord length, 115.8 in.		Chord length, 105.54 in.							



NOTE: U, upper surface; L, lower surface.

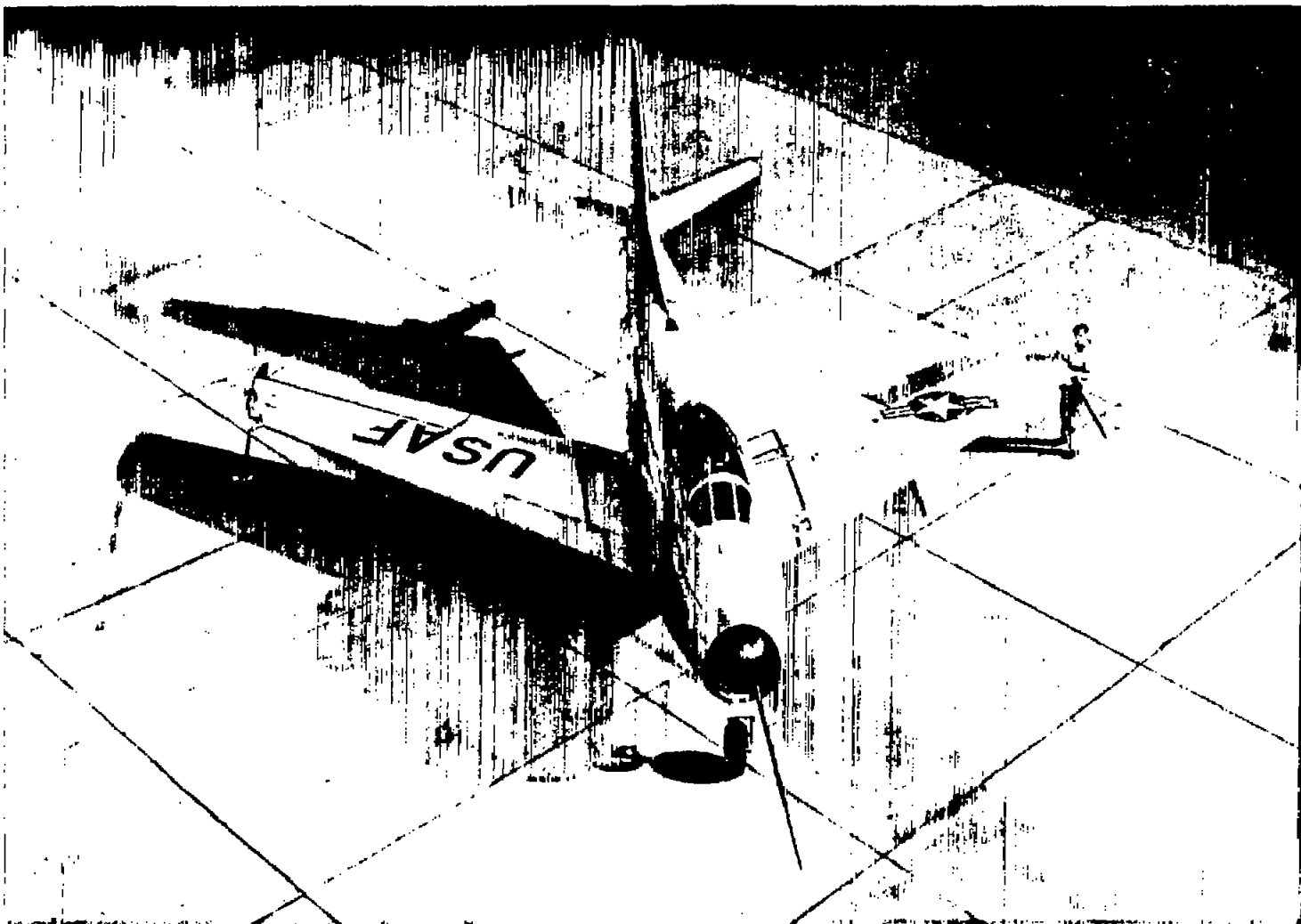


Figure 1.— The test airplane.

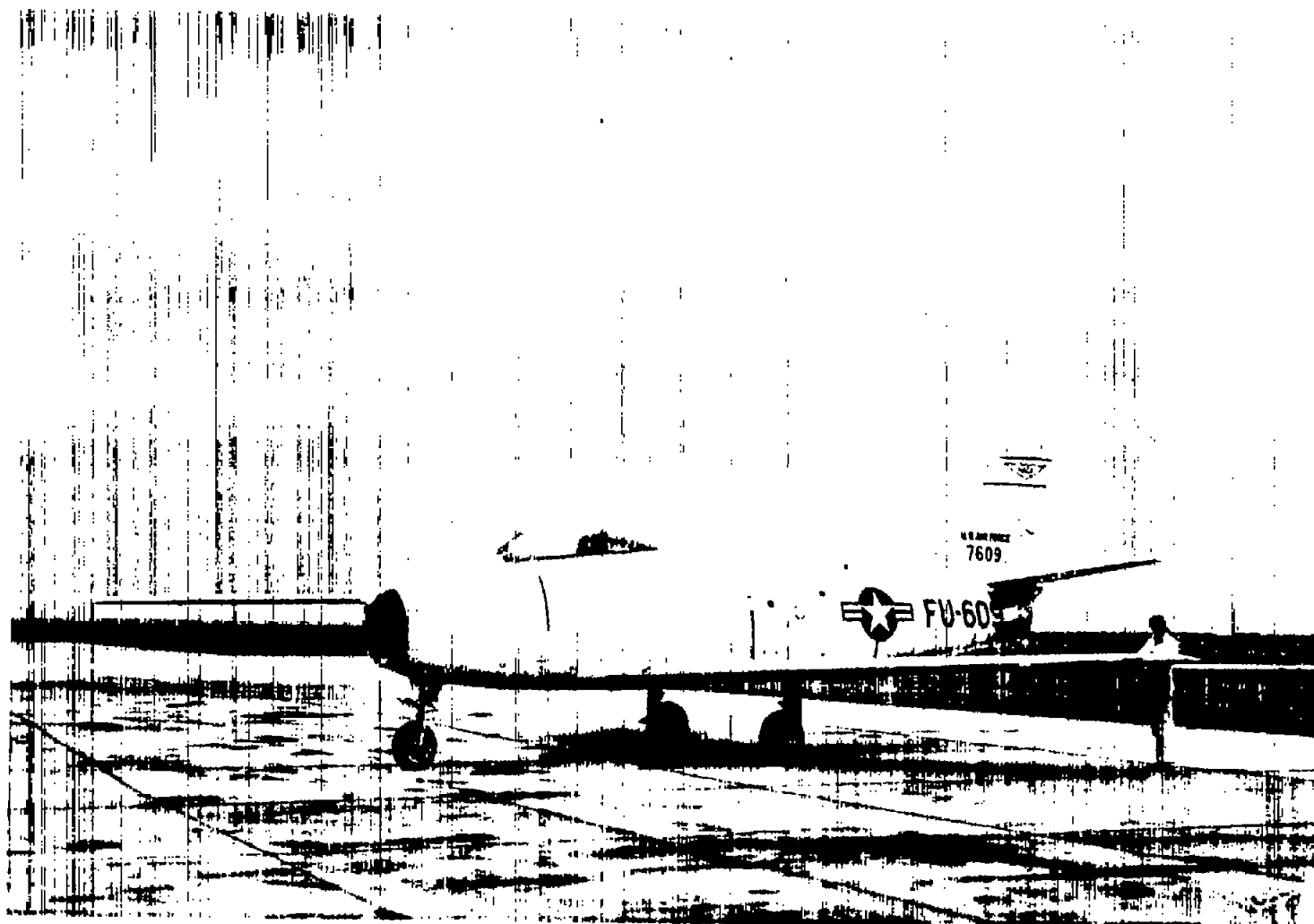


Figure 2.— Side view of test airplane.

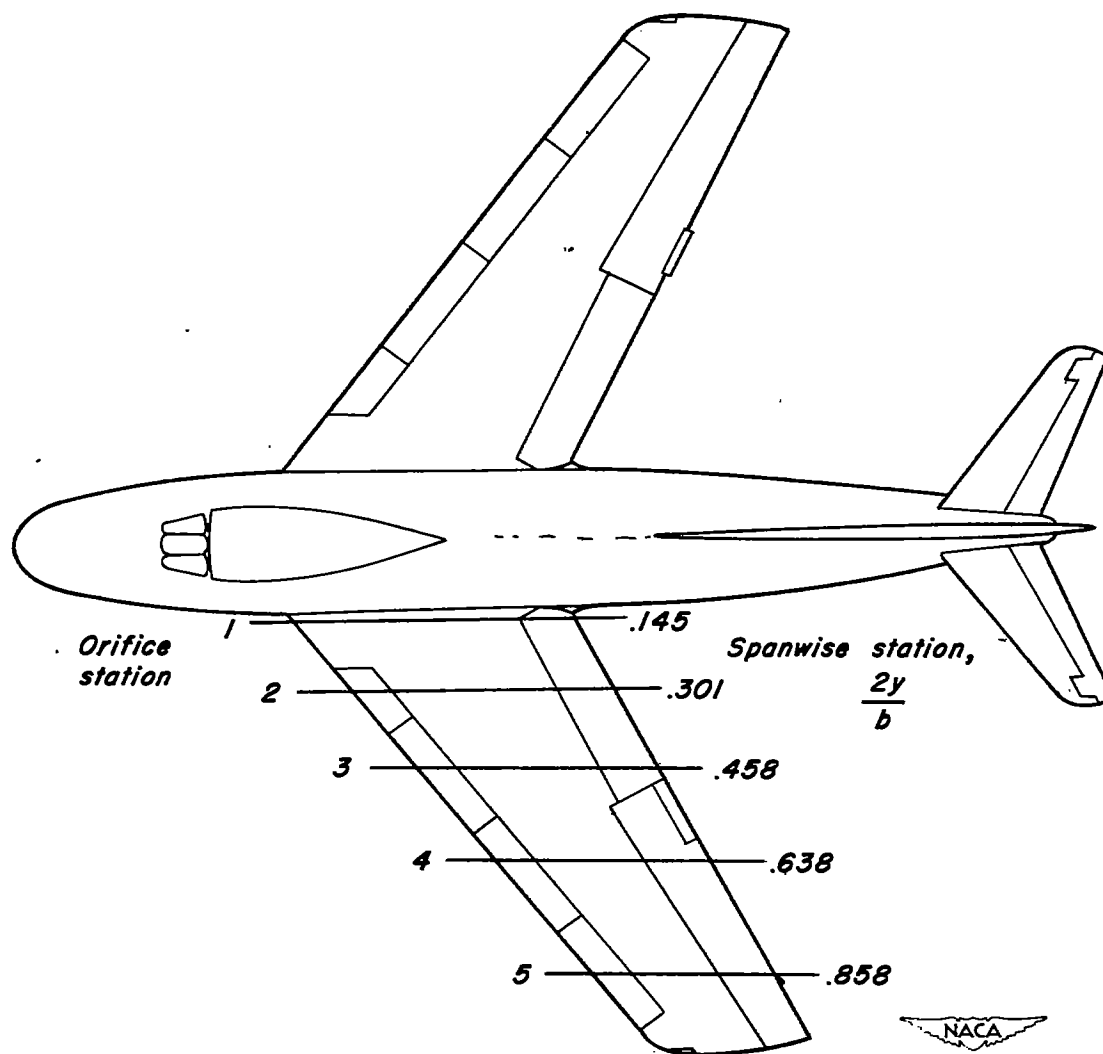


Figure 3.— Location of pressure-orifice stations.

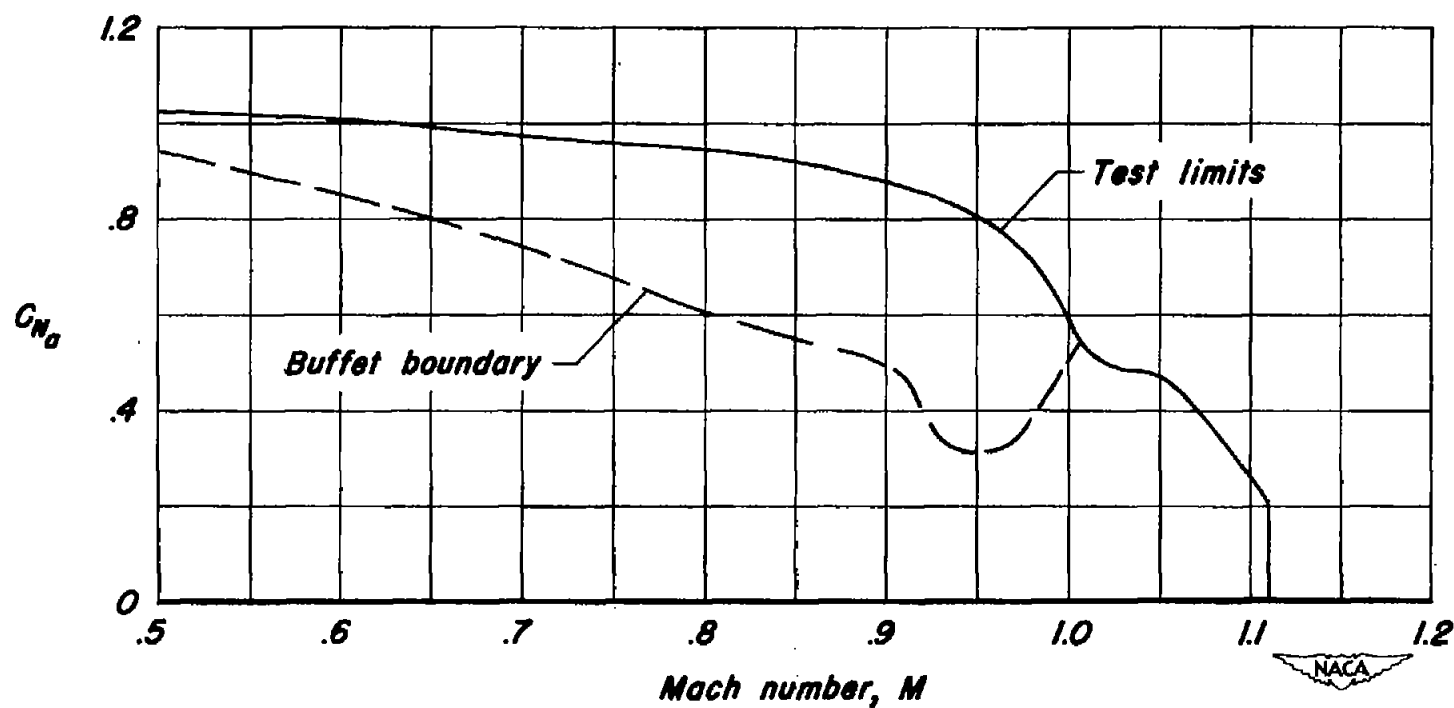


Figure 4.—Test limits and buffet boundary for test airplane.

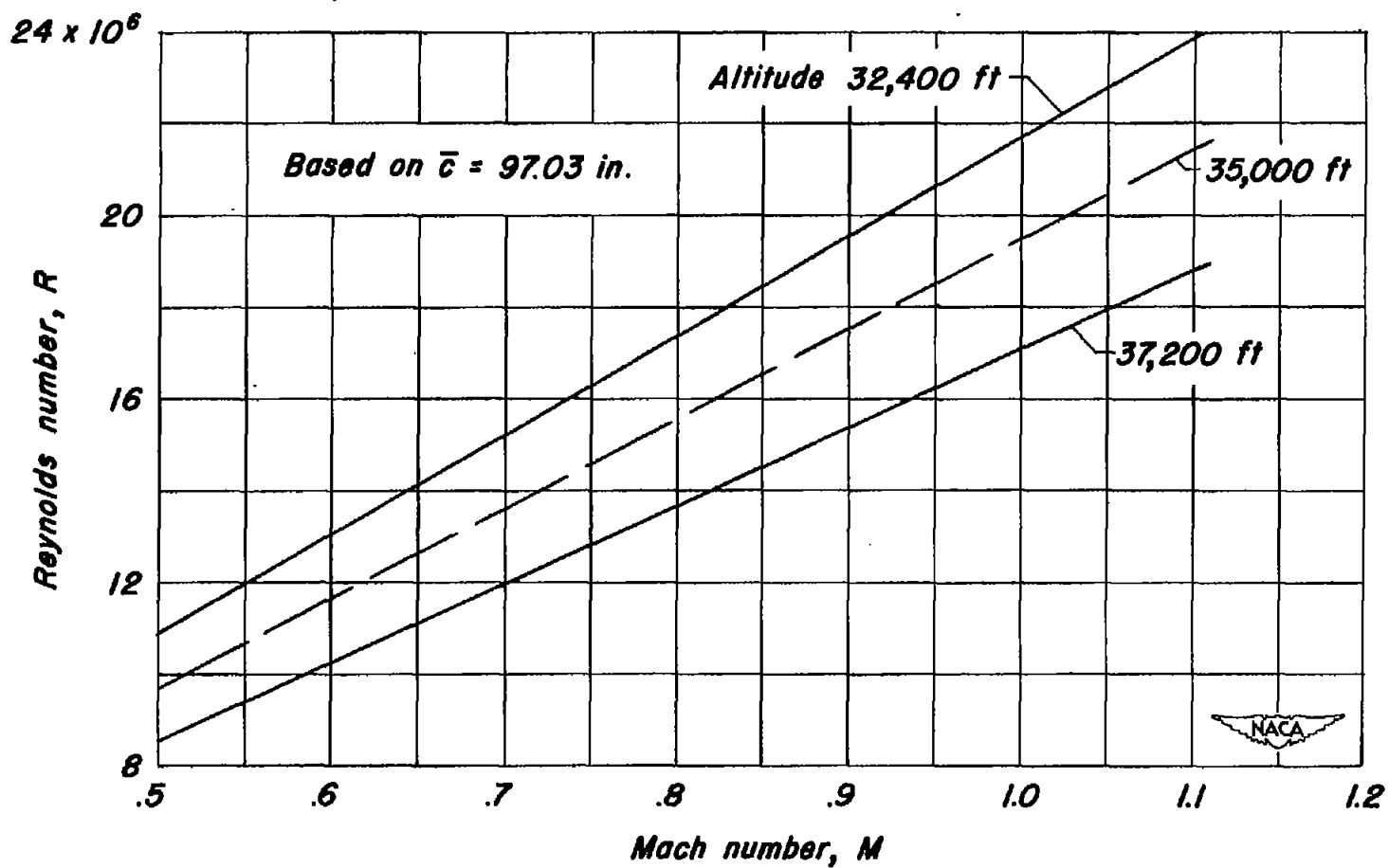
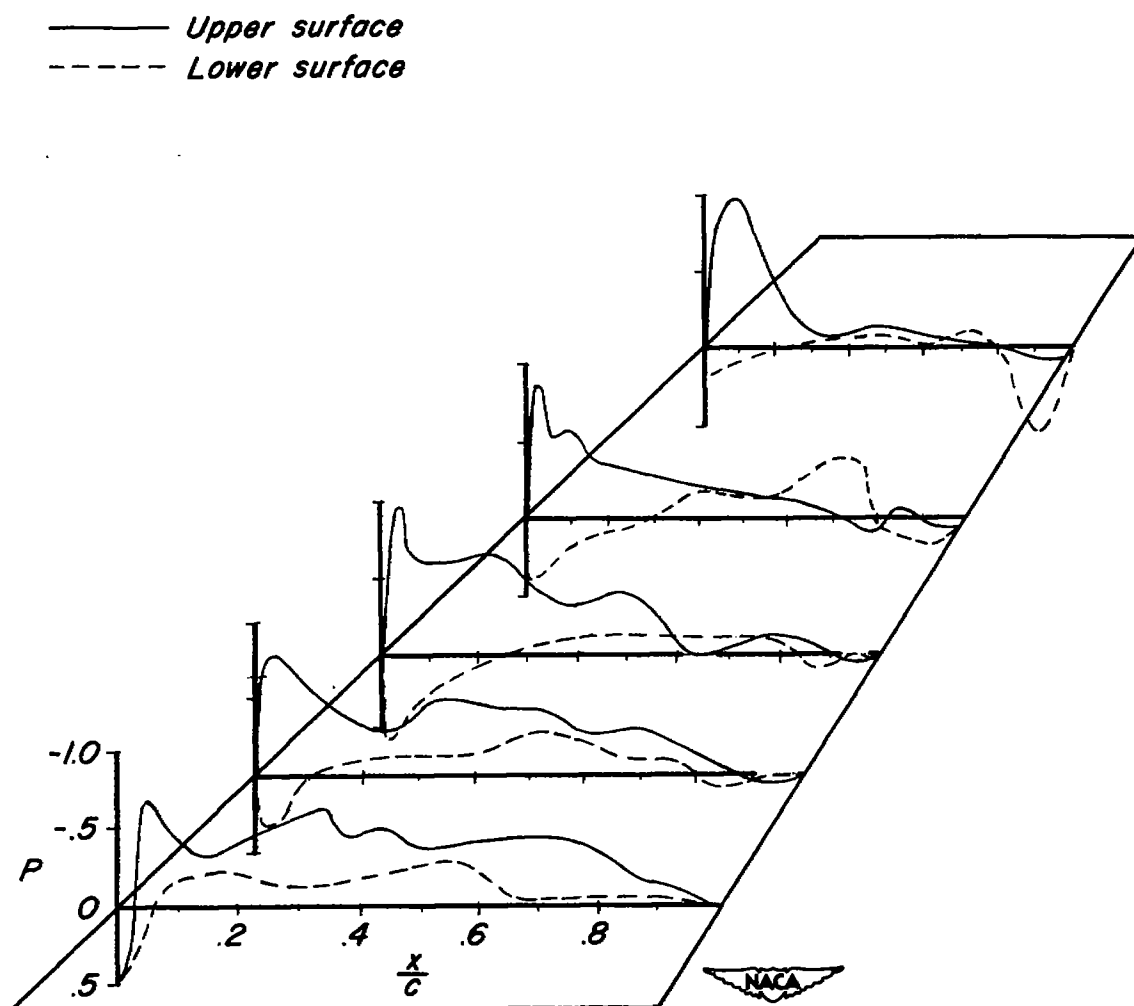
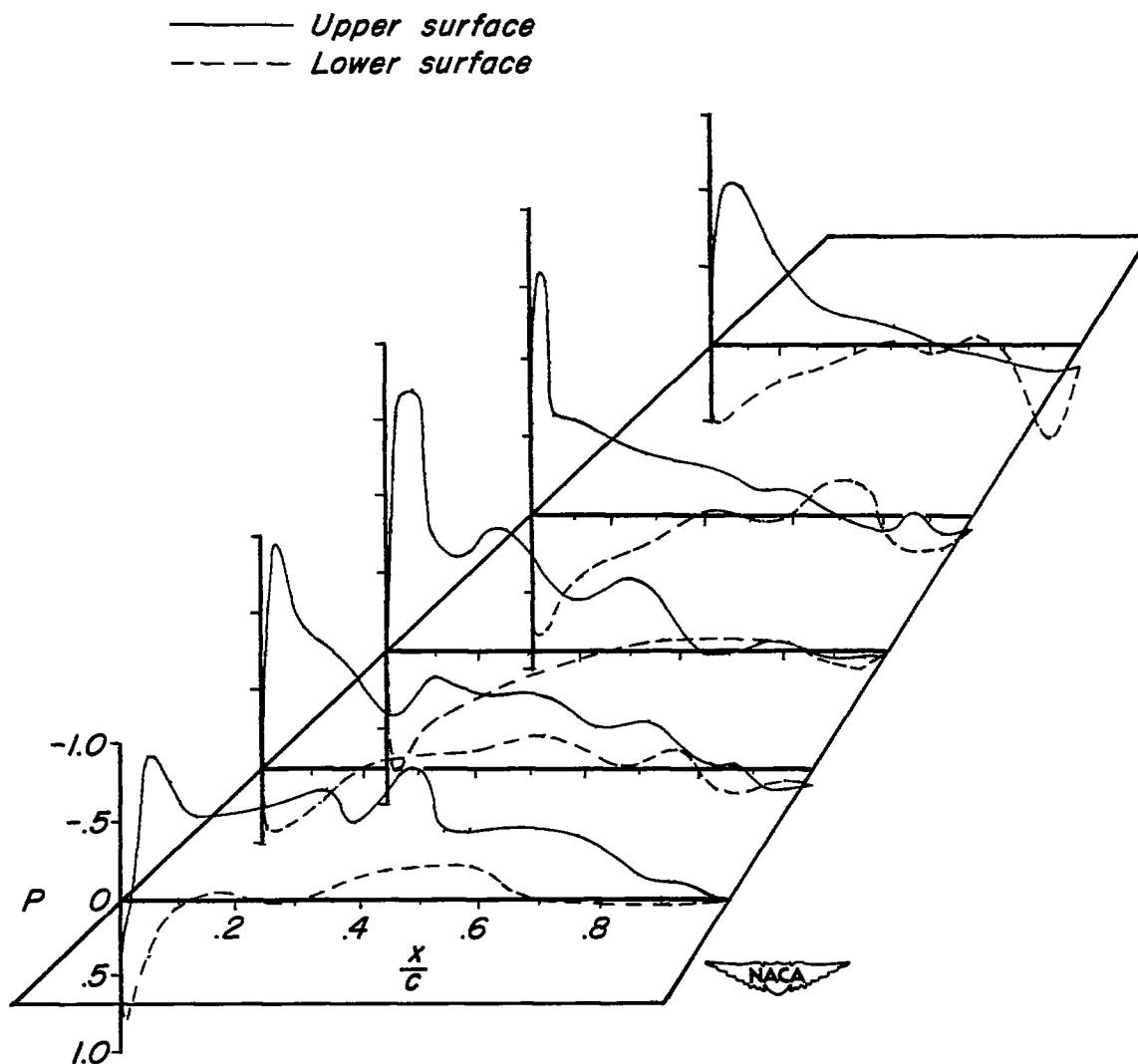


Figure 5.—Variation of Reynolds number with Mach number for tests.



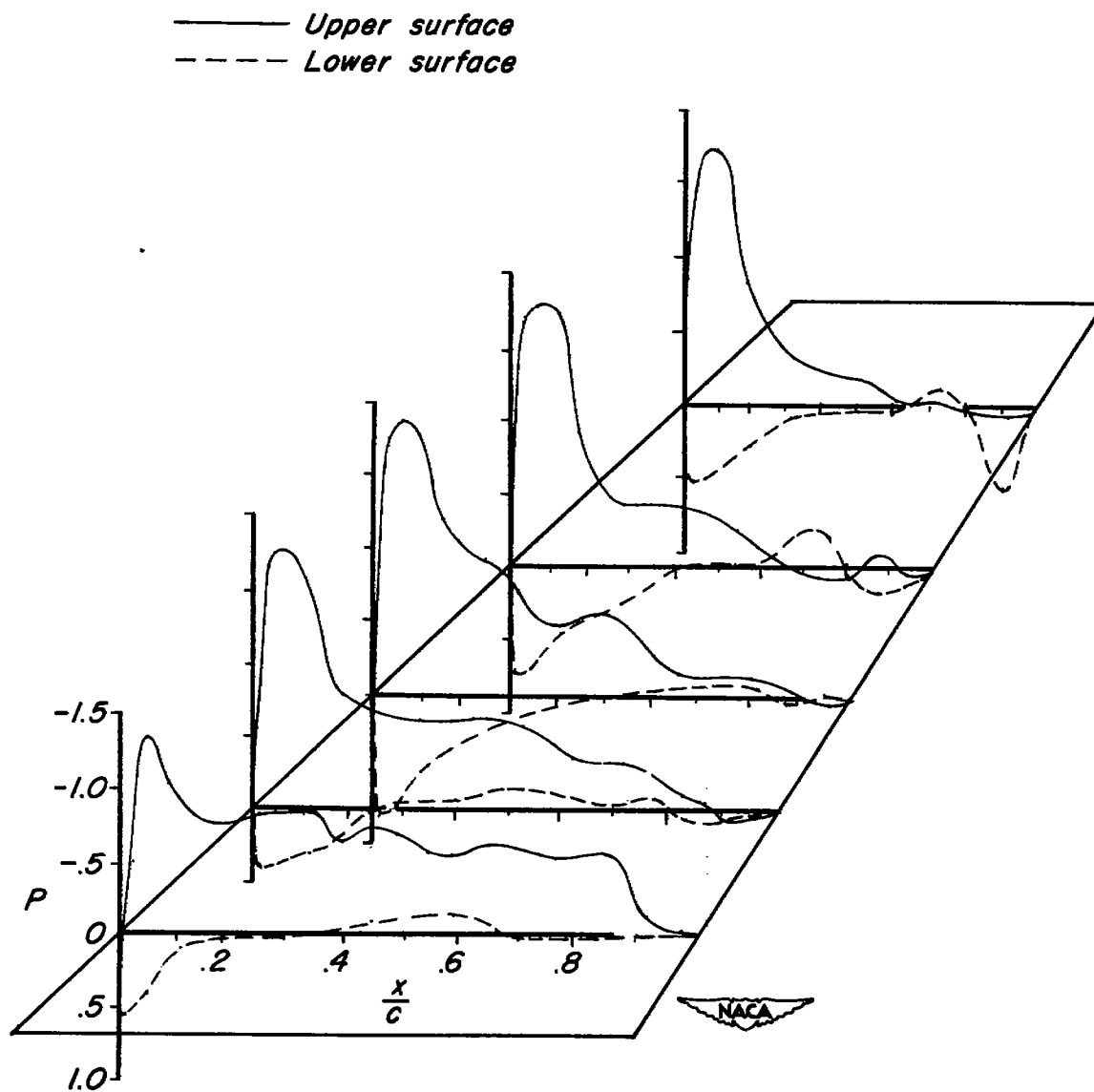
(a) $M_n = 0.70$; $C_{N_d} = 0.20$; $\alpha_u = 3.5^\circ$

Figure 6.— Wing pressure distribution.



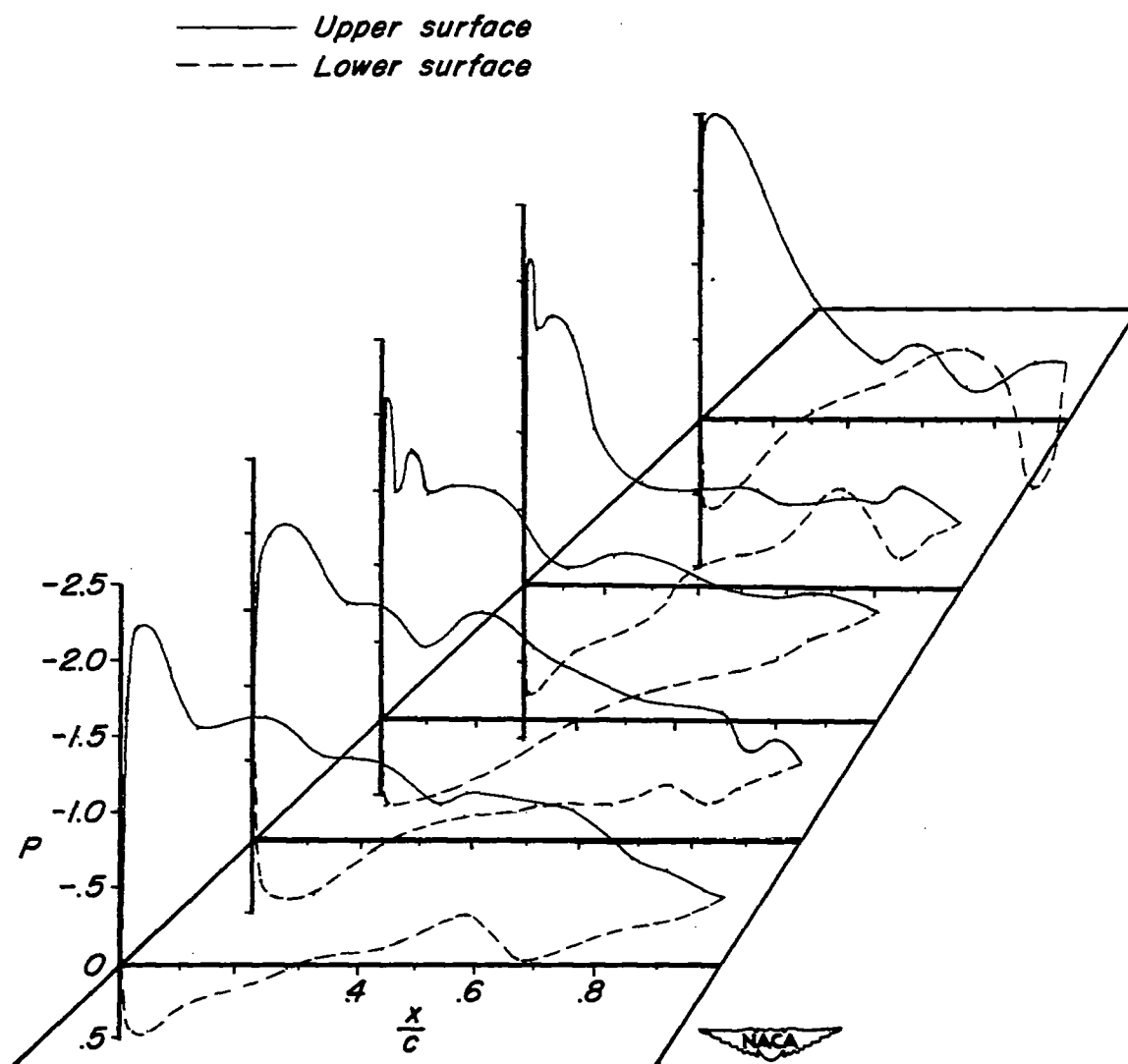
(b) $M_n = 0.70$; $C_{N_a} = 0.41$; $\alpha_u = 6.4^\circ$

Figure 6.— Continued.



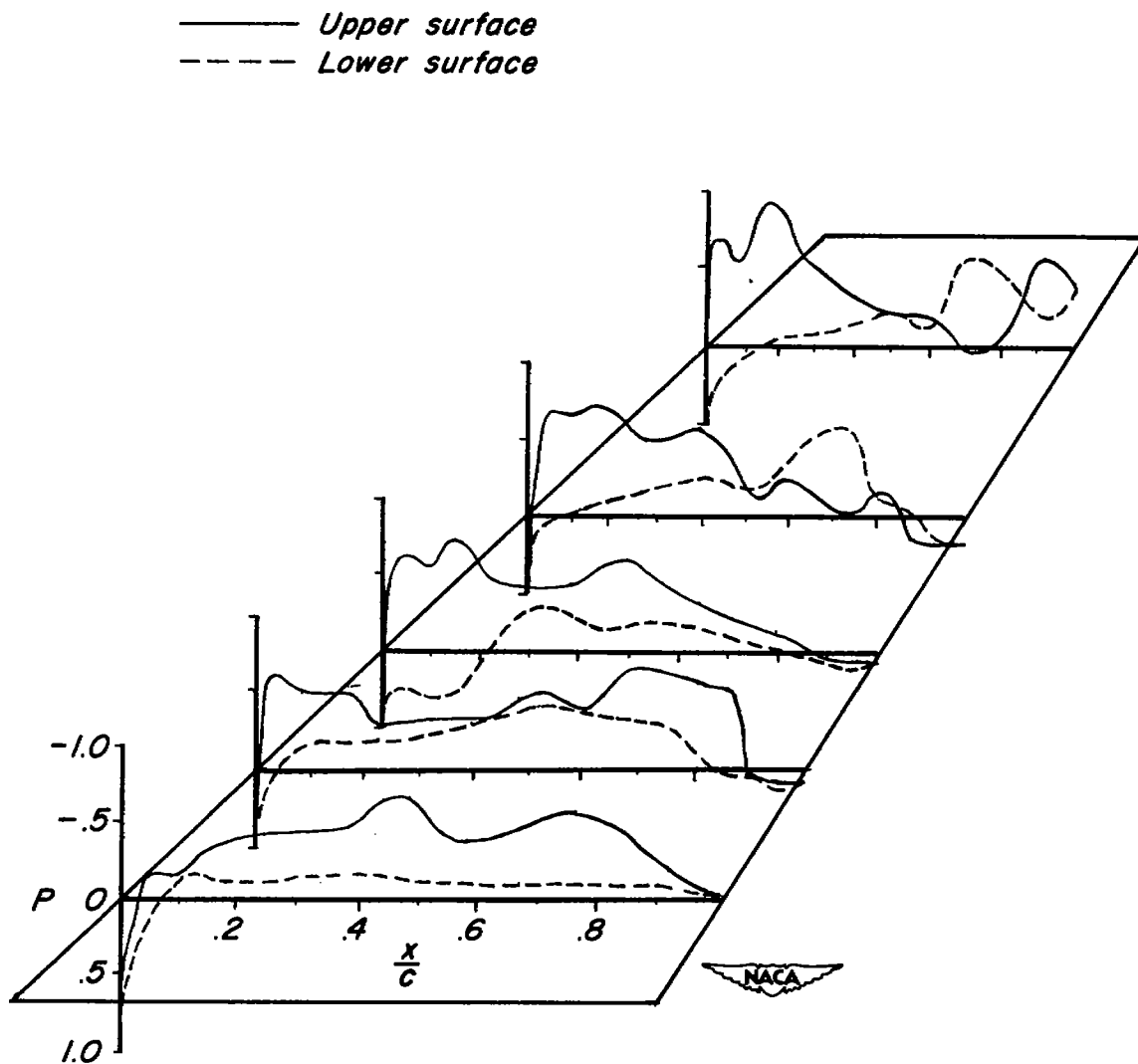
(c) $M_n = 0.70$; $C_{N_a} = 0.58$; $\alpha_u = 9.6^\circ$

Figure 6. - Continued.



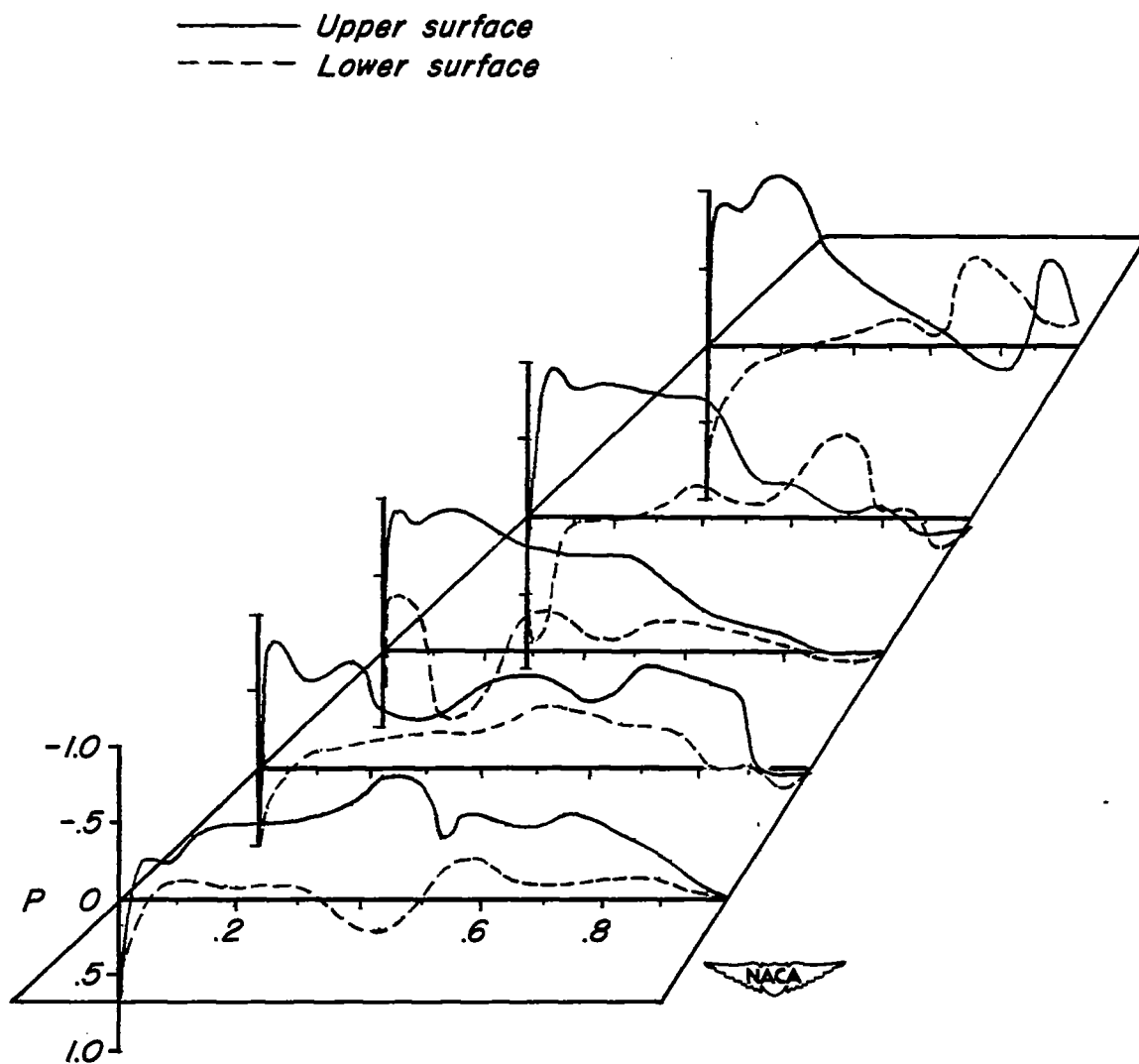
(d) $M_h = 0.70$; $C_{Na} = 0.90$; $\alpha_u = 19.4^\circ$

Figure 6.—Continued.



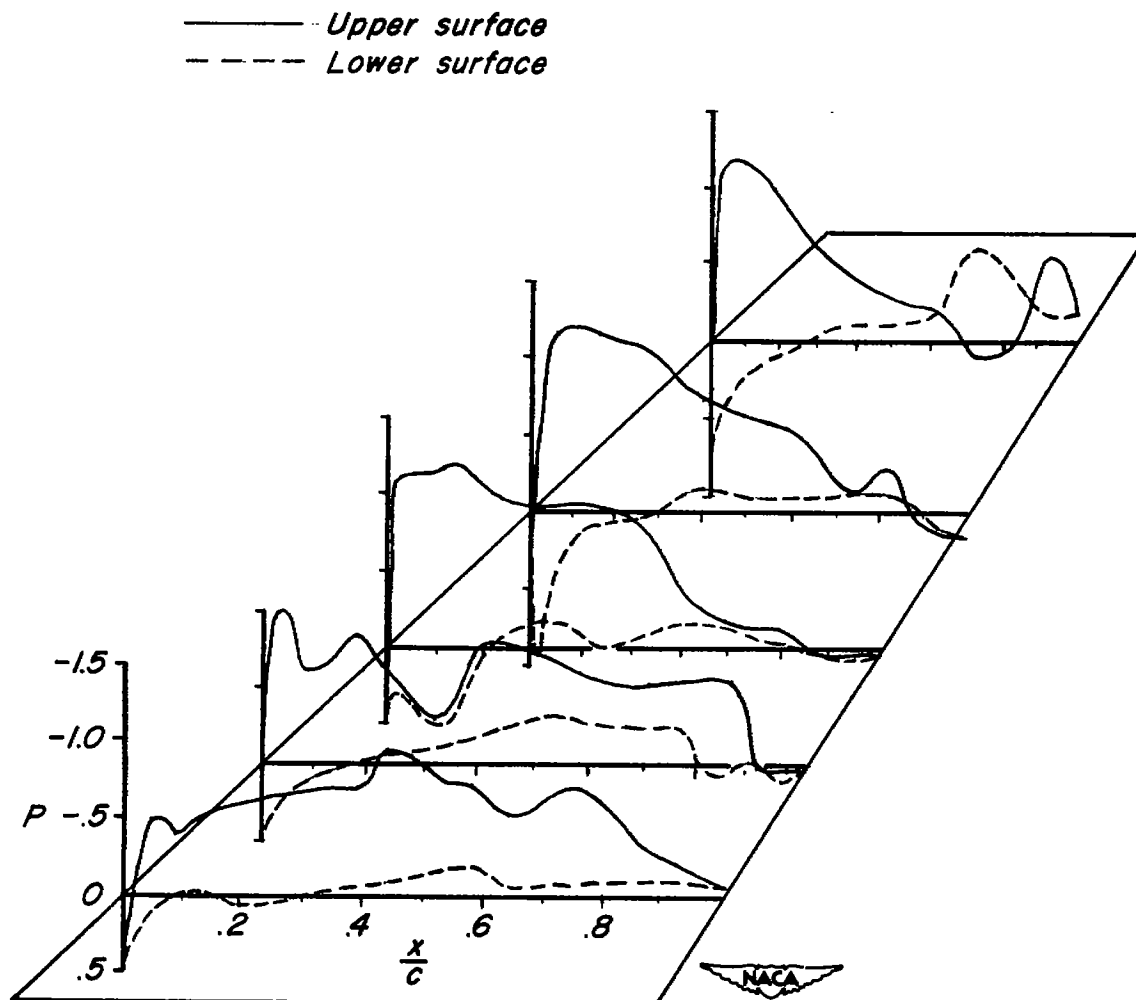
(e) $M_n = 0.87$; $C_{Na} = 0.17$; $\alpha_u = 2.5^\circ$

Figure 6.- Continued.



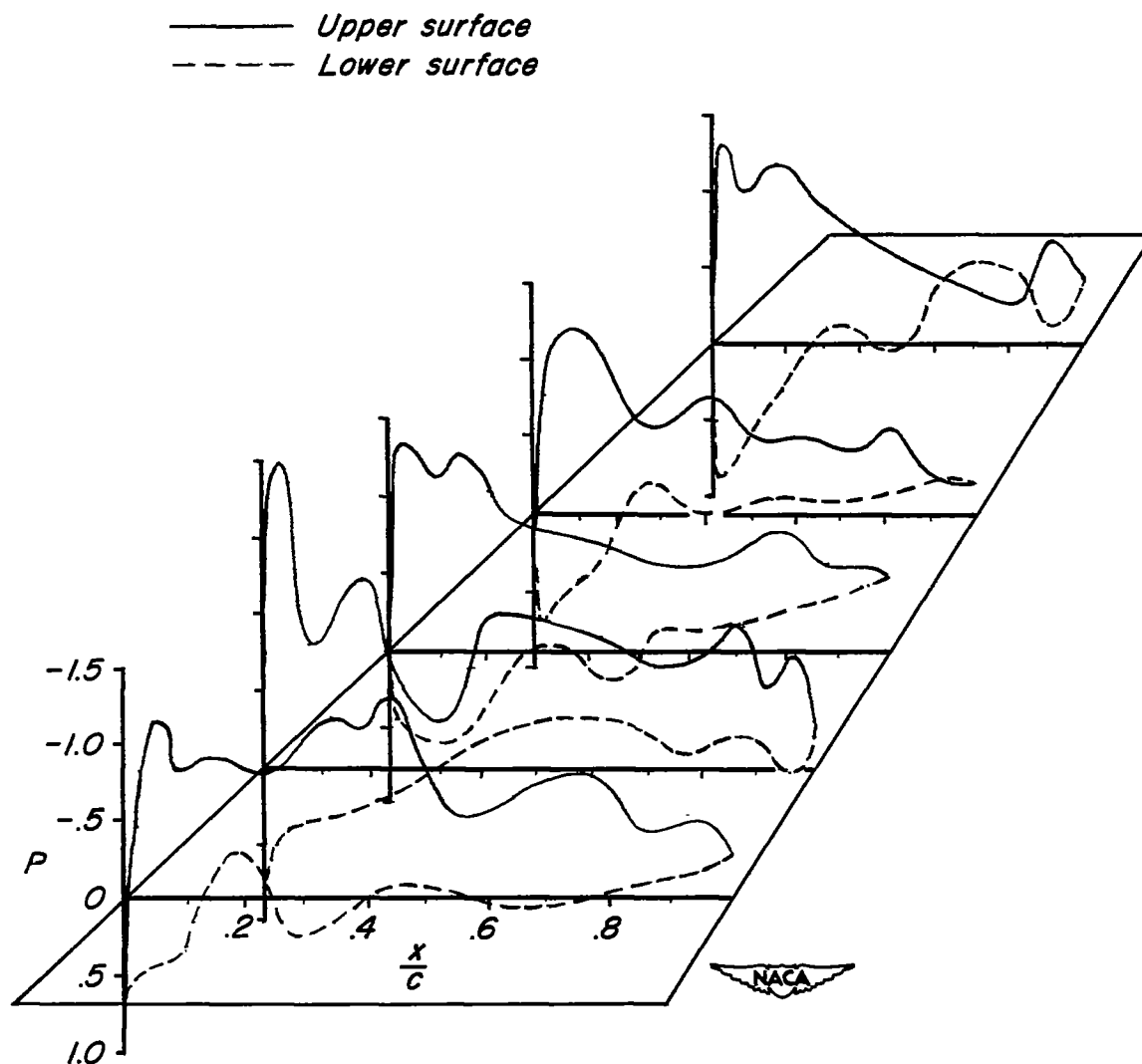
(f) $M_n = 0.87$; $C_{N_a} = 0.39$; $\alpha_u = 5.2^\circ$

Figure 6.— Continued.



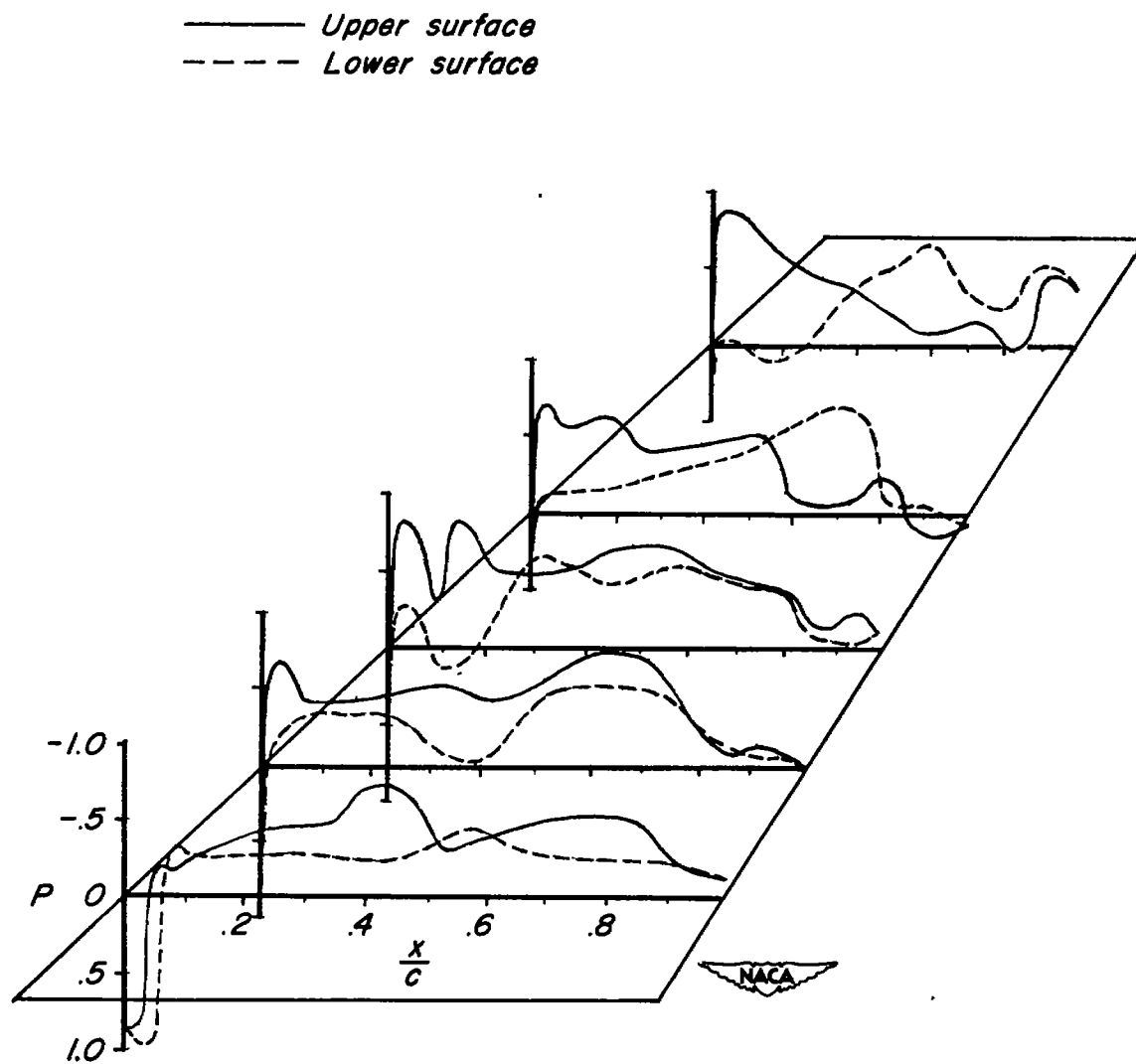
(g) $M_n = 0.87$; $C_{N_a} = 0.59$; $\alpha_u = 8.1^\circ$

Figure 6.-Continued.



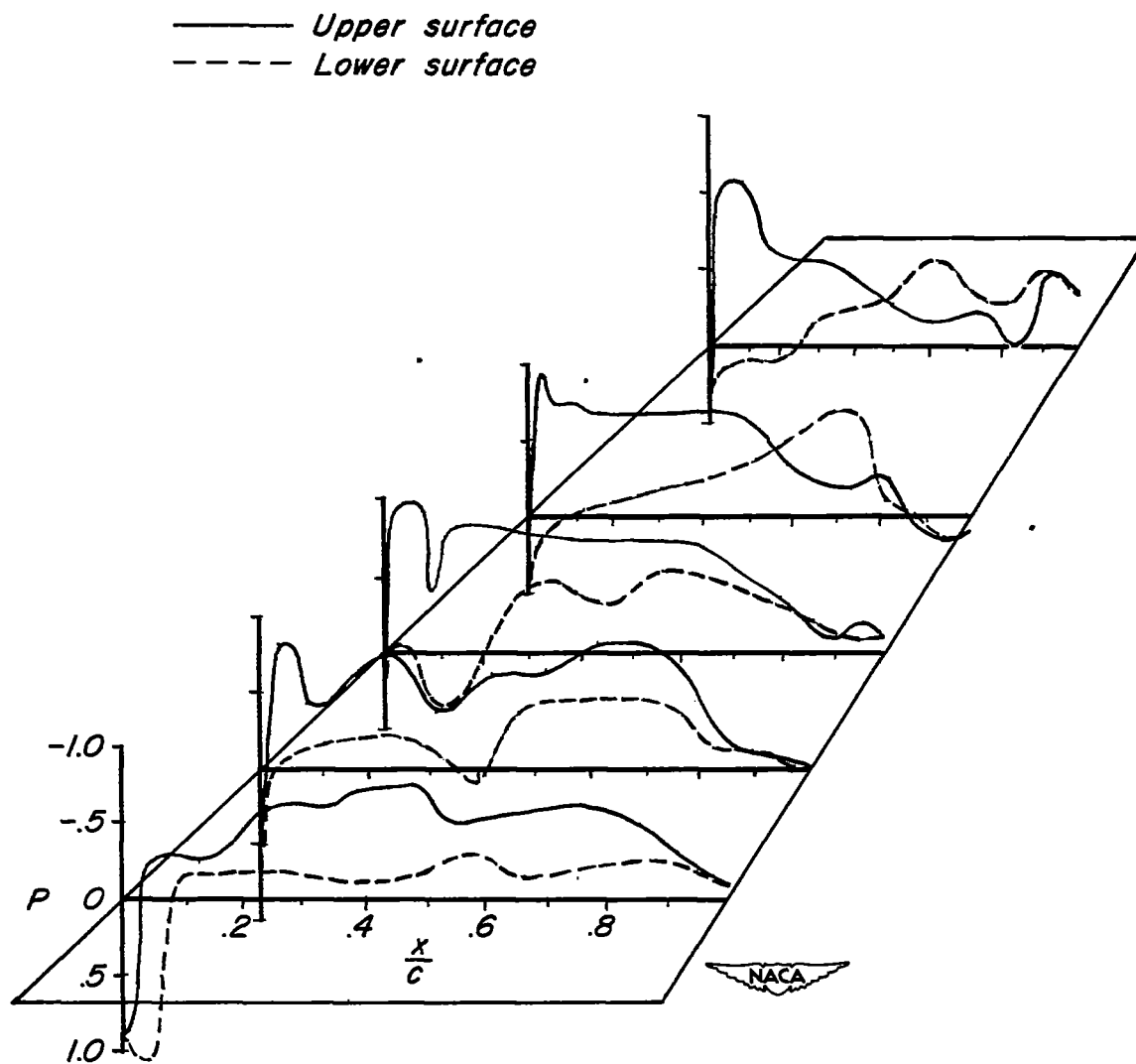
(h) $M_n = 0.87$; $C_{N_a} = 0.85$; $\alpha_u = 16.6^\circ$

Figure 6.-Continued.



(i) $M_n = 0.90$; $C_{N_a} = 0.20$; $\alpha_u = 5.5^\circ$

Figure 6.—Continued.



(j) $M_n = 0.90$; $C_{N_d} = 0.39$; $\alpha_u = 8.2^\circ$

Figure 6.- Continued

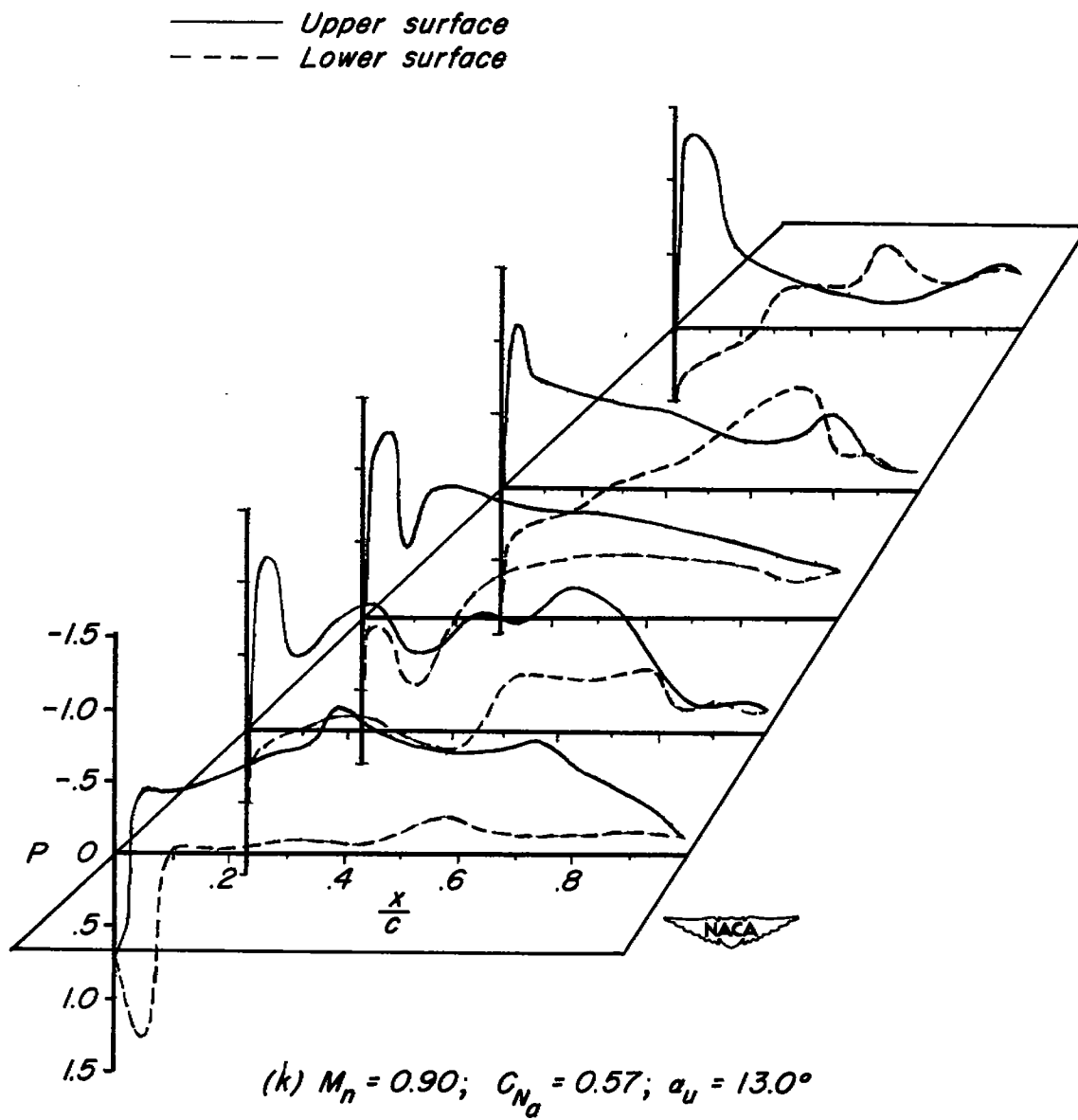
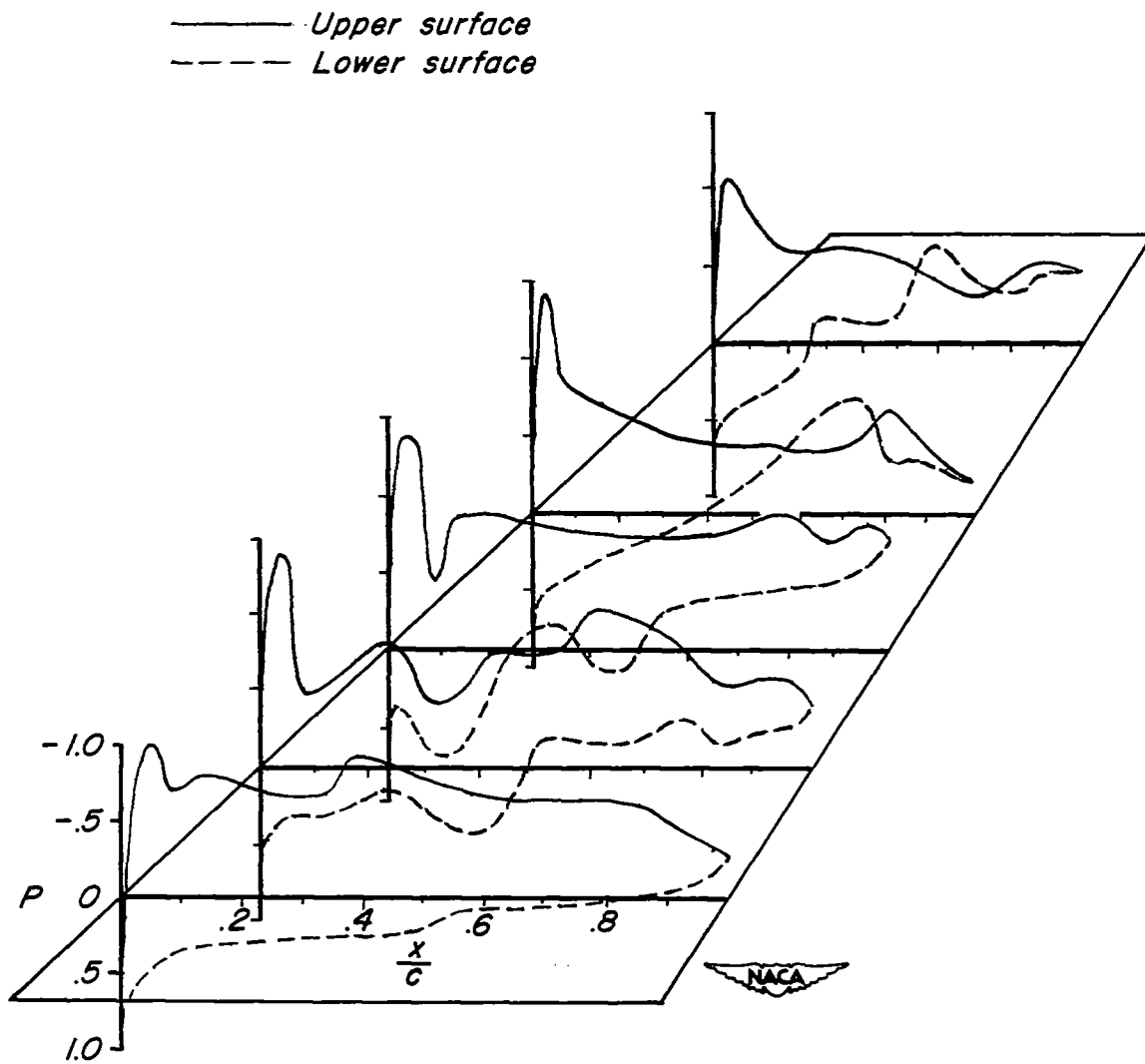
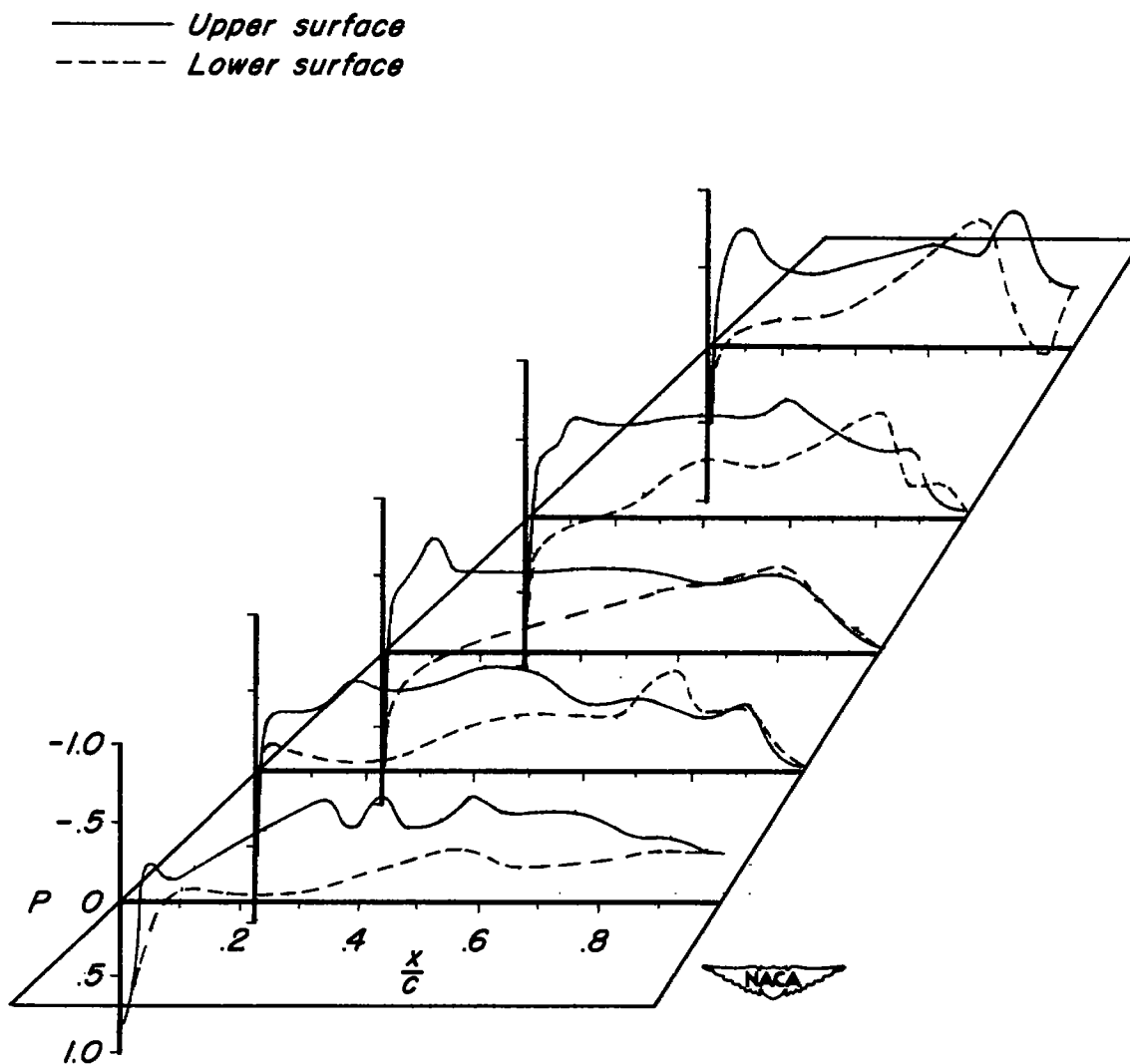


Figure 6.- Continued.



(1) $M_n = 0.90$; $C_{N_a} = 0.81$; $\alpha_u = 21.7^\circ$

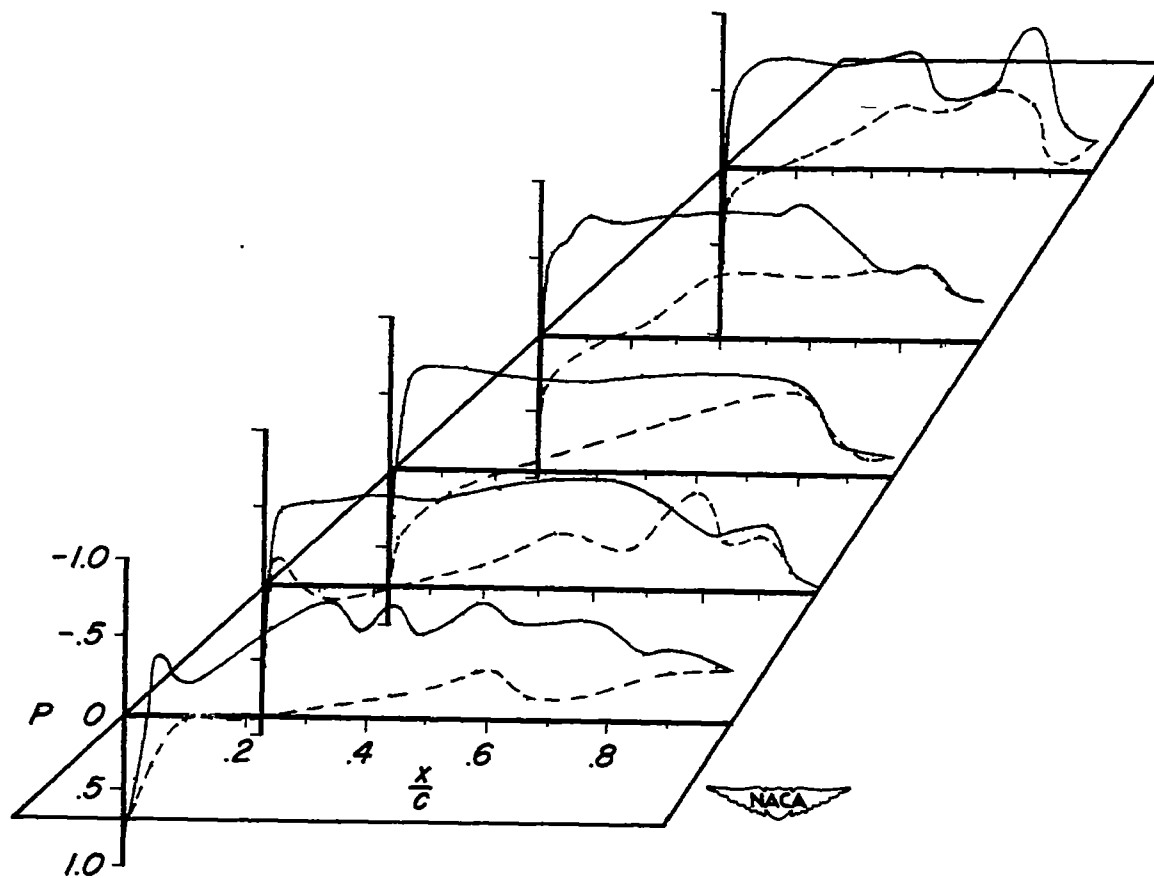
Figure 6.- Continued.



(m) $M_h = 0.97$; $C_{N_a} = 0.17$

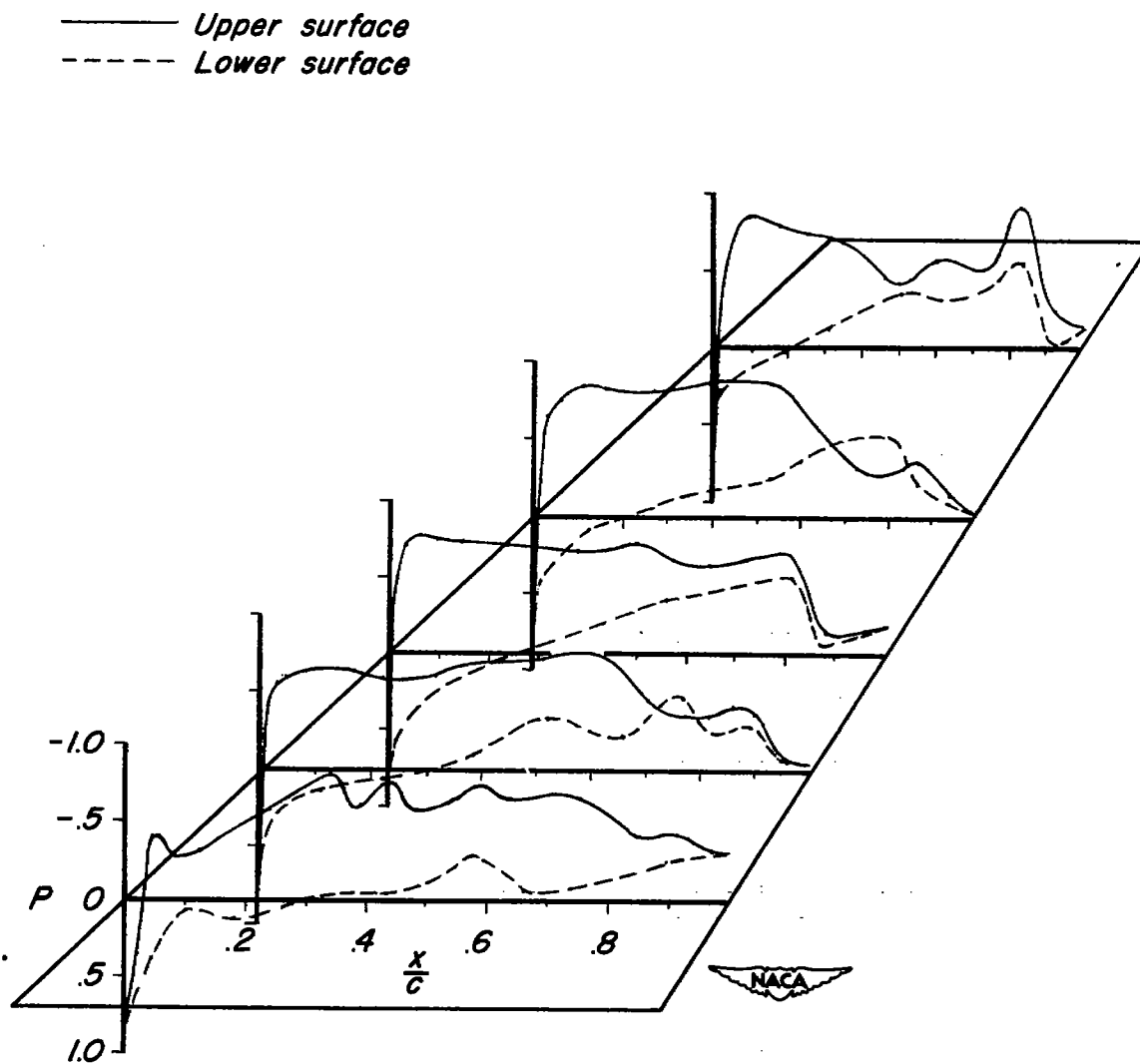
Figure 6. — Continued.

— Upper surface
--- Lower surface



(n) $M_n = 0.97$; $C_{N_0} = 0.34$

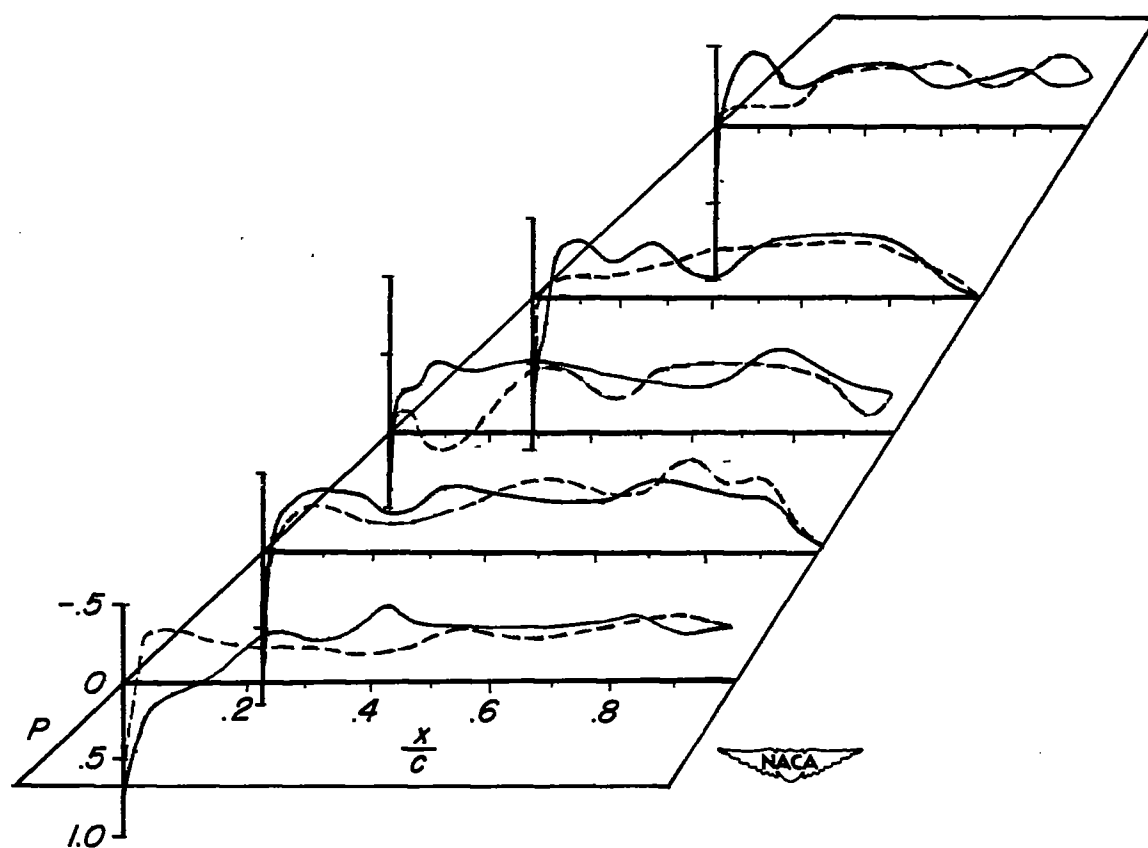
Figure 6.- Continued.



(o) $M_n = 0.97$; $C_{N_a} = 0.47$

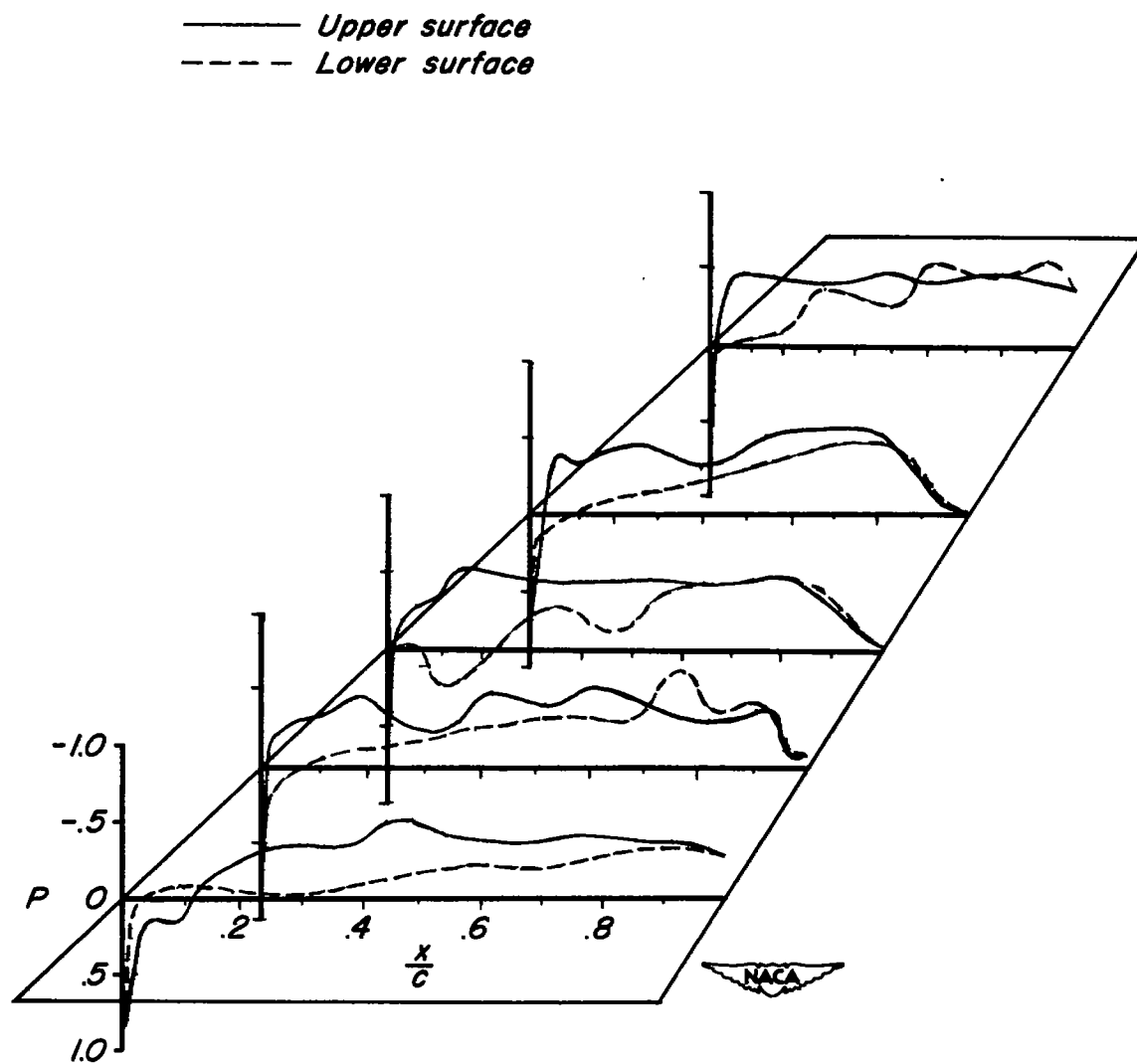
Figure 6.- Continued.

— Upper surface
- - - Lower surface



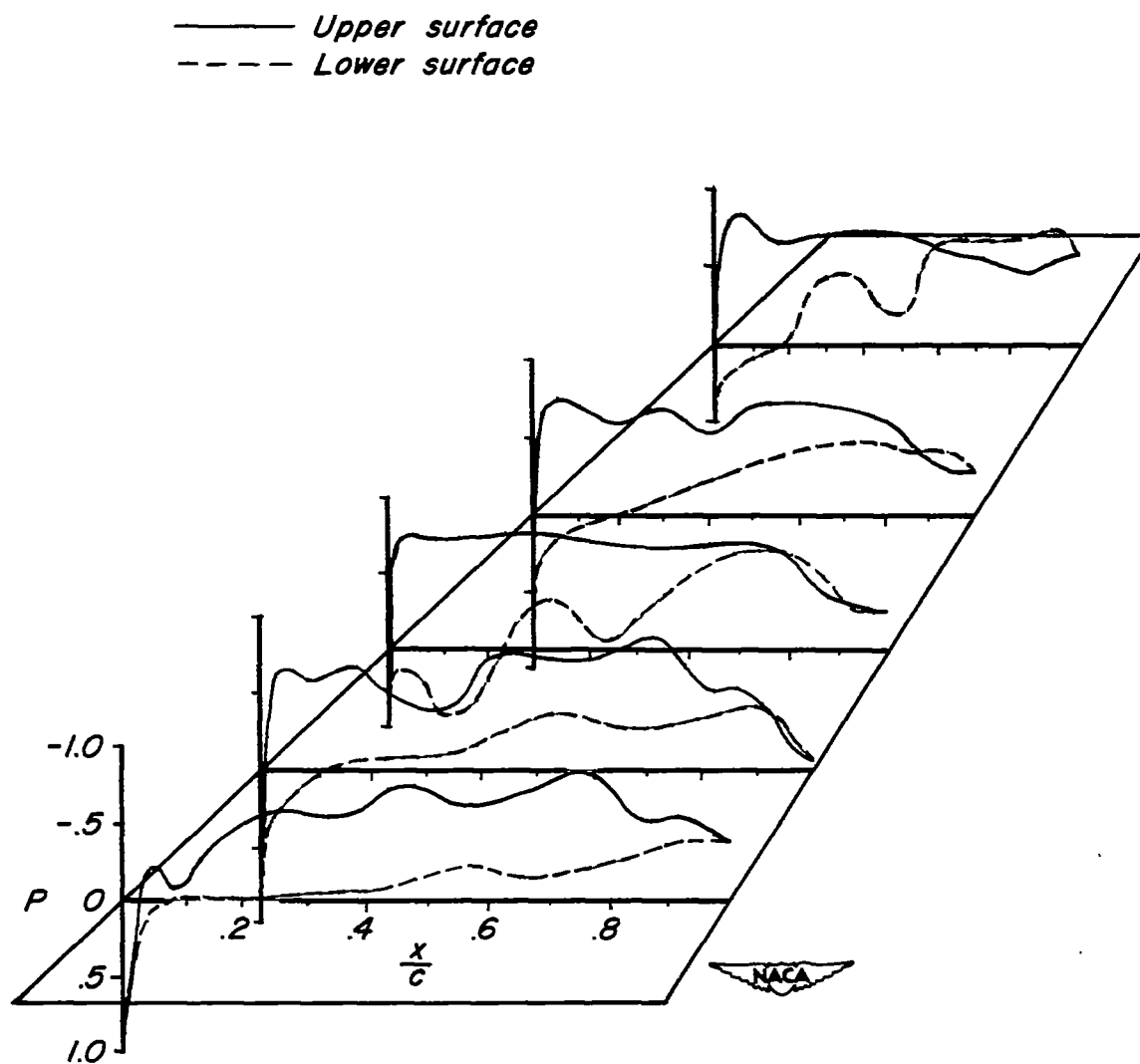
(p) $M_n = 1.02$; $C_{N_a} = 0.10$; $\alpha_u = 3.8^\circ$

Figure 6.- Continued.



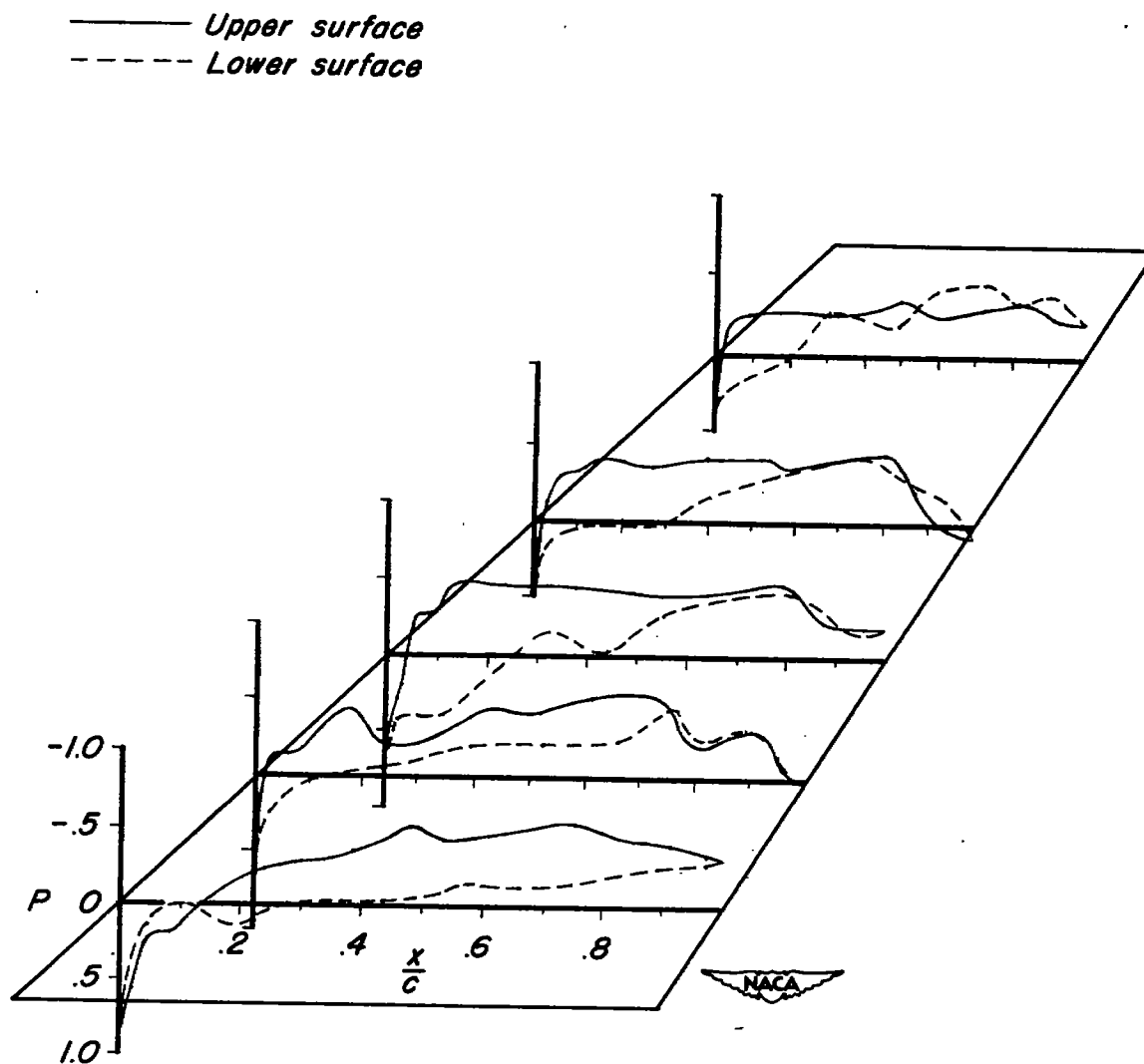
(q) $M_n = 1.02$; $C_{Na} = 0.30$; $\alpha_u = 6.6^\circ$

Figure 6.—Continued.



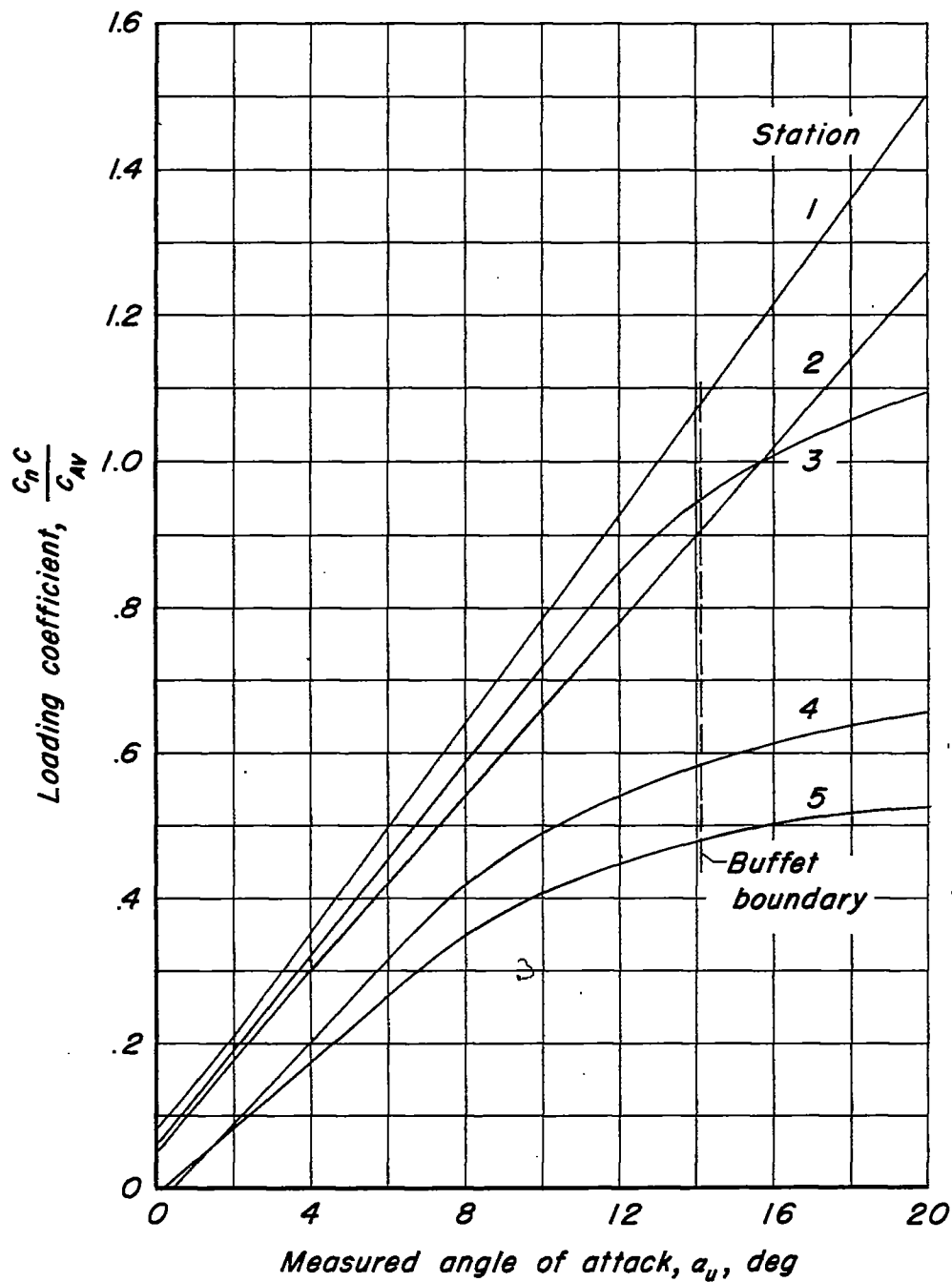
(r) $M_n = 1.02$; $C_{N_a} = 0.50$; $\alpha_u = 9.3^\circ$

Figure 6.- Continued.



(s) $M_n = 1.11$; $C_{Na} = 0.20$

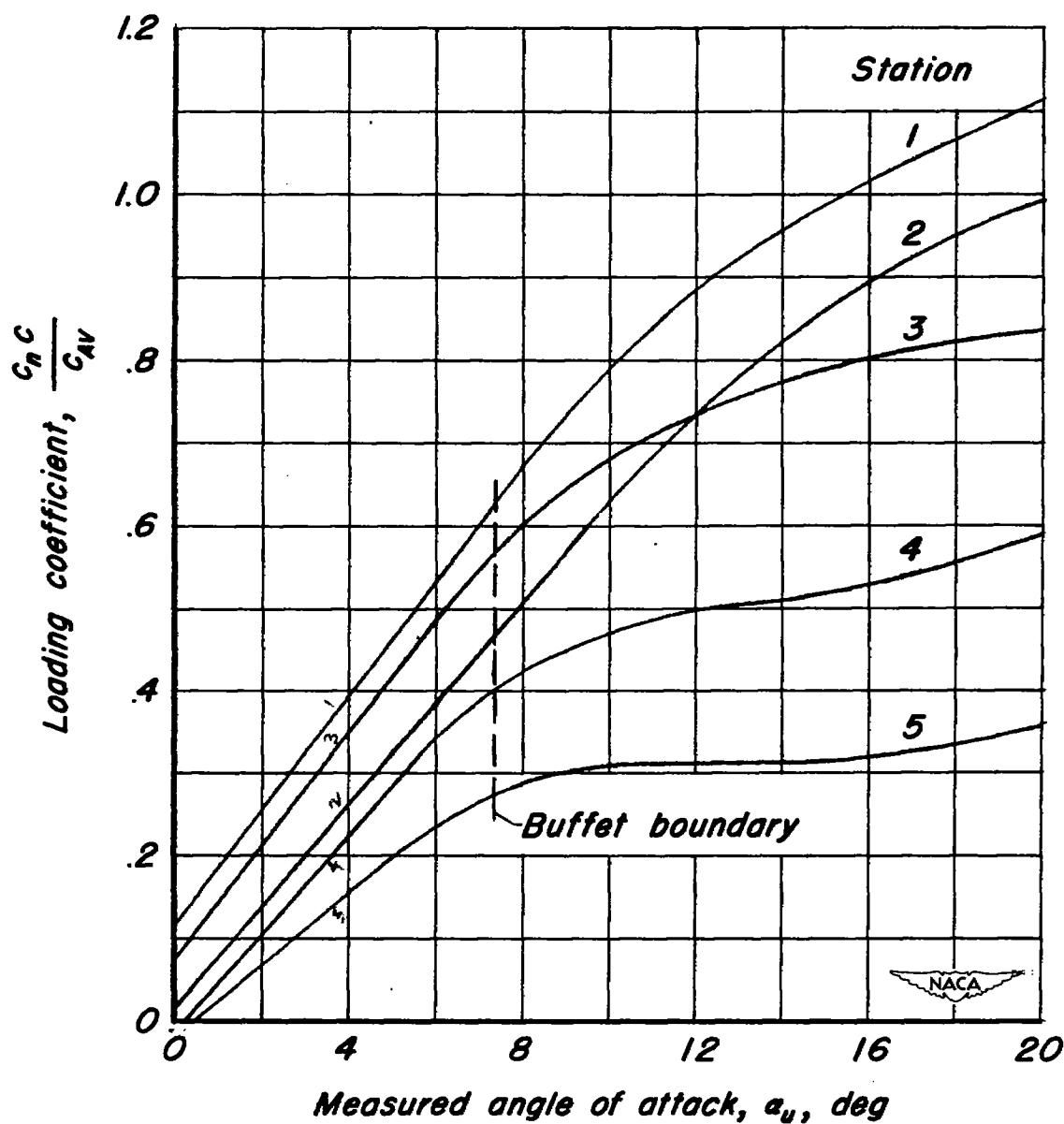
Figure 6.- Concluded.



(a) $M_n = 0.70$

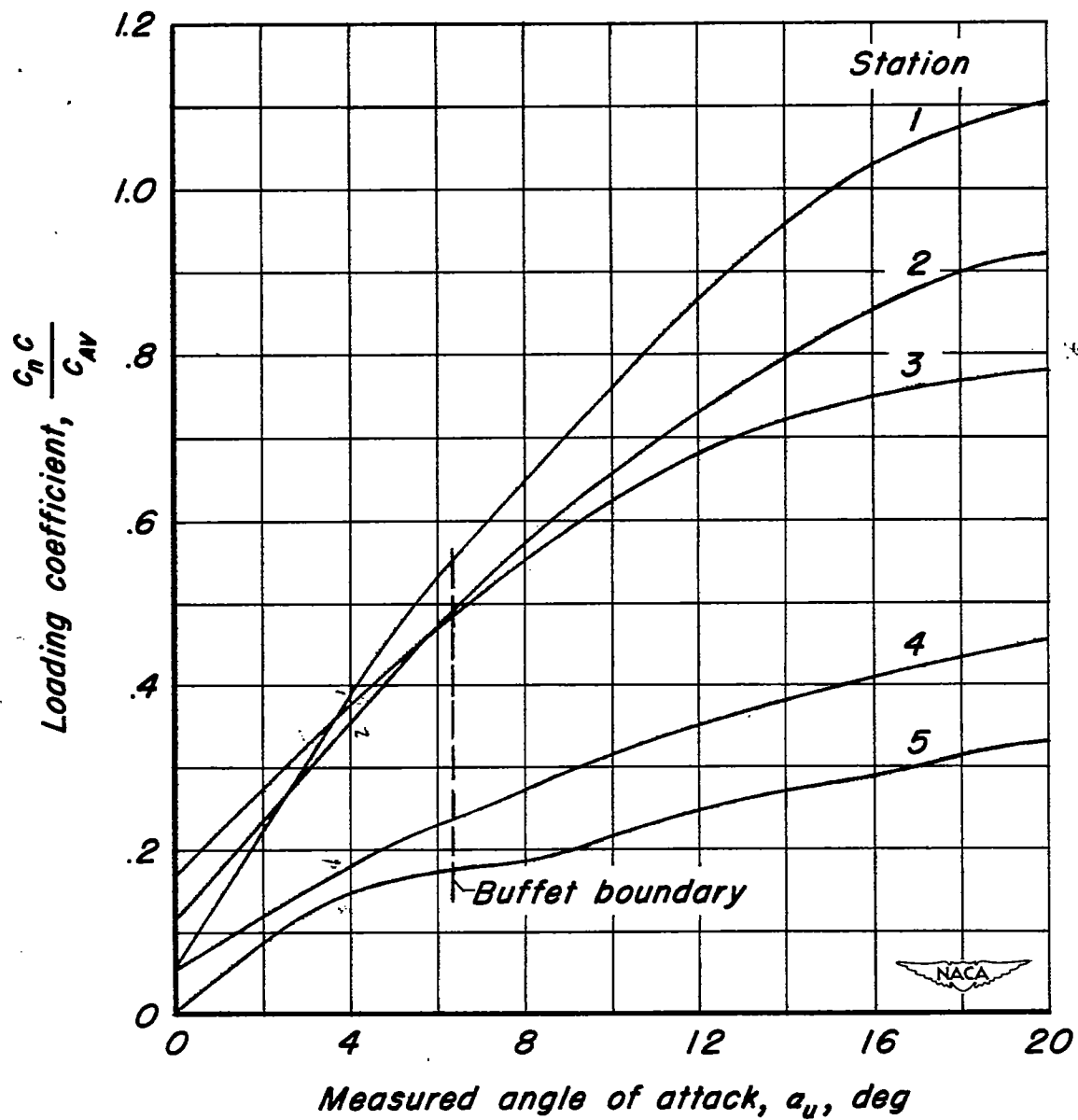


Figure 7.- Section lift characteristics .



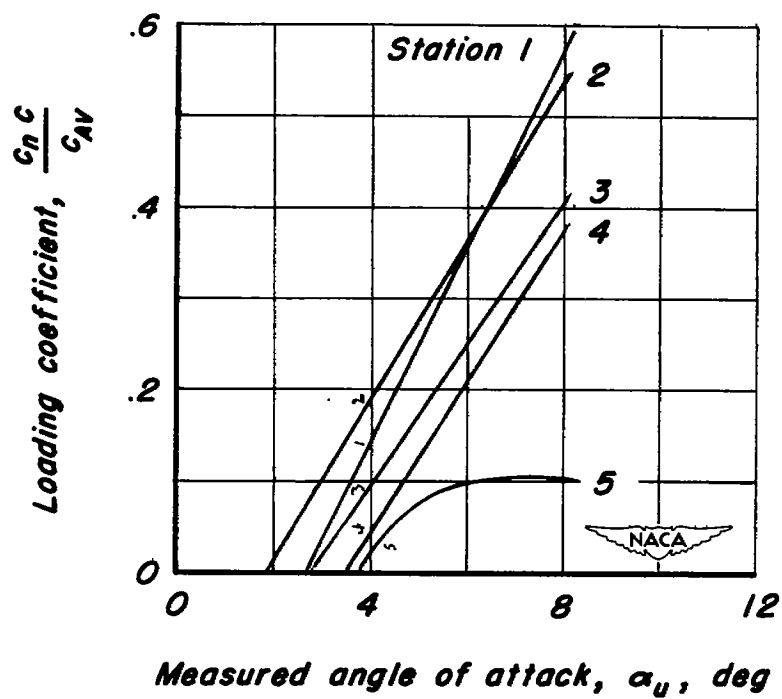
(b) $M_n = 0.87$

Figure 7.—Continued.



(c) $M_n = 0.90$

Figure 7.- Continued.



(d) $M_n = 1.02$

Figure 7. - Concluded.

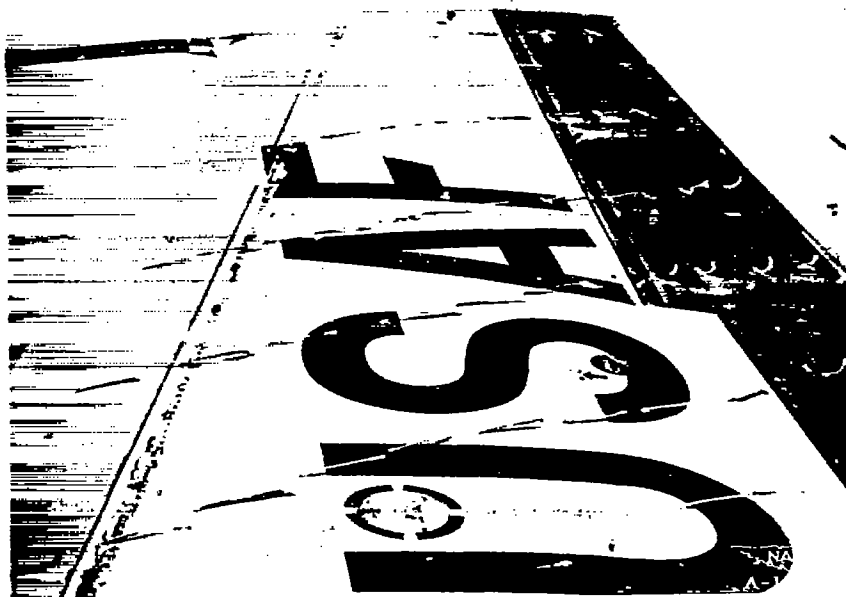
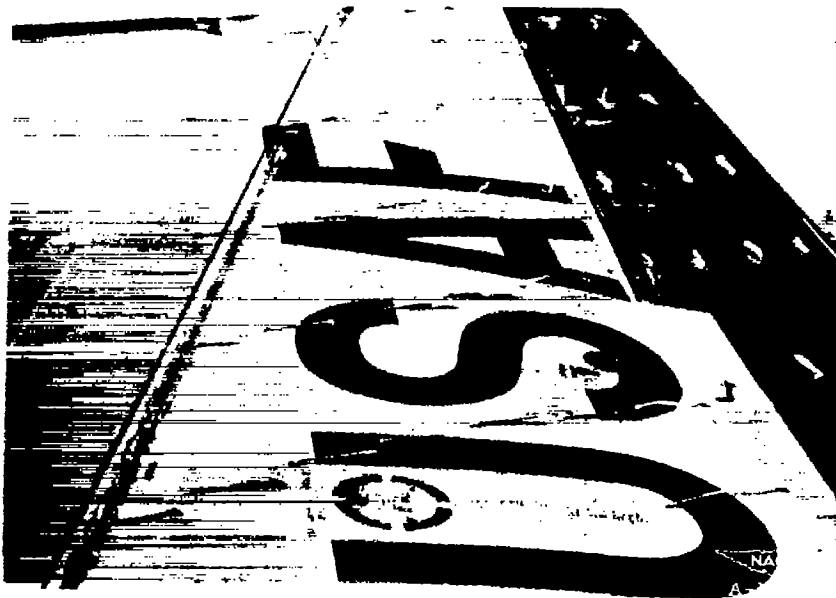
(a) $C_{N_a} = 0.18$ (b) $C_{N_a} = 0.27$

Figure 8.— Photographs of tuft behavior showing stalling of outer panel.
 $M = 0.9$.

CONFIDENTIAL



(c) $C_{Na} = 0.49$



(d) $C_{Na} = 0.74$

Figure 8.— Concluded.

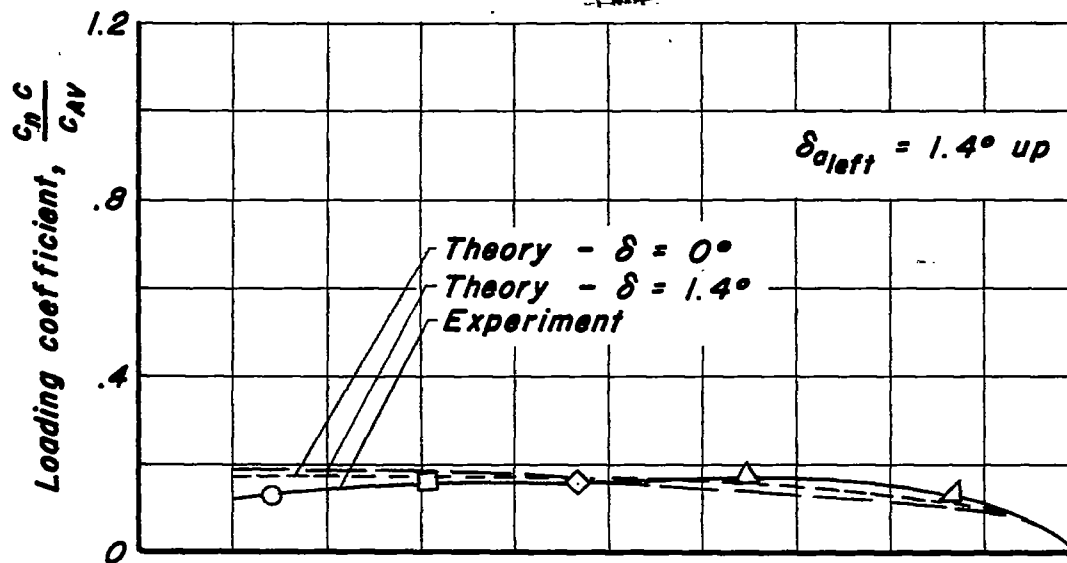
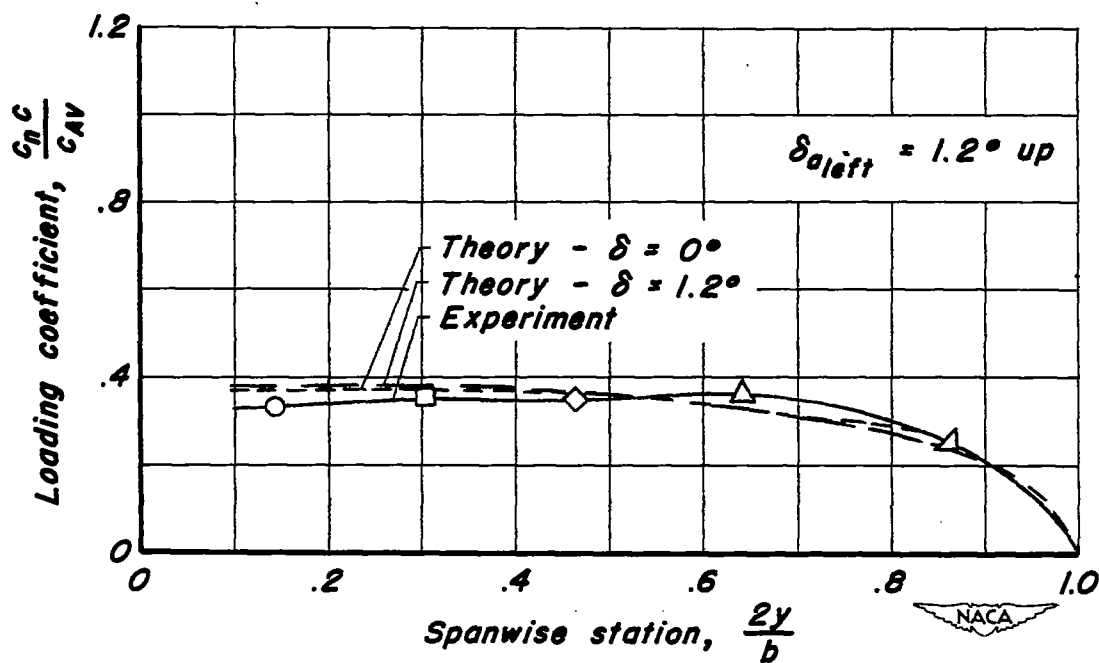
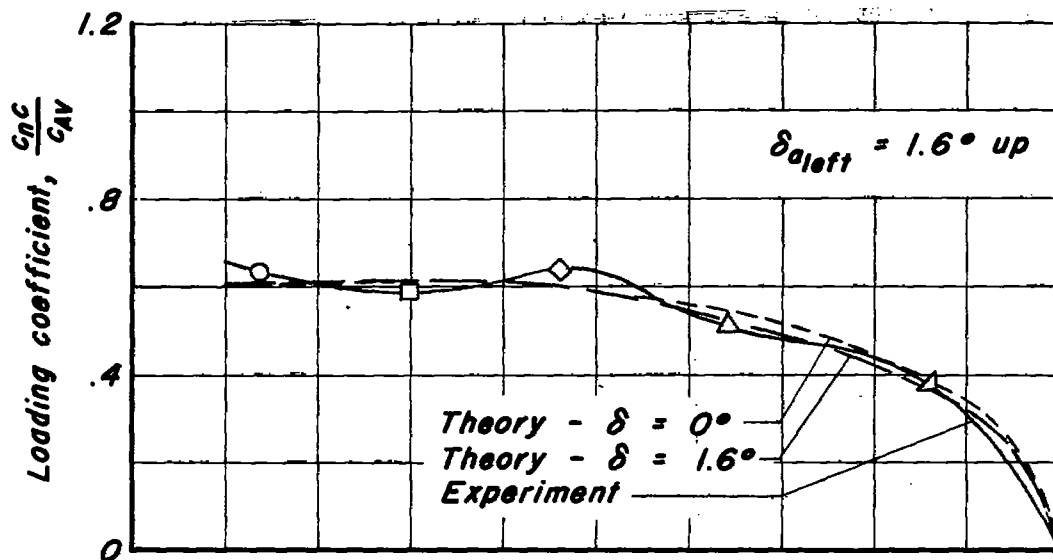
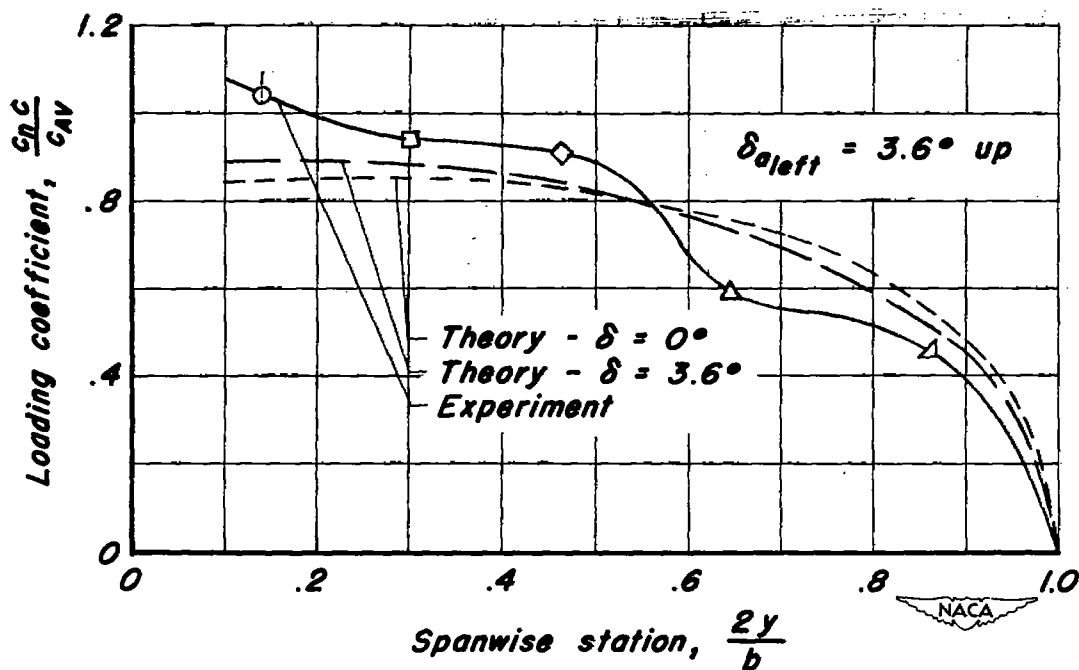
(a) $C_{N_0} = 0.2$; $M_n = 0.70$ (b) $C_{N_0} = 0.4$; $M_n = 0.70$

Figure 9.- Spanwise distribution of additional loading.

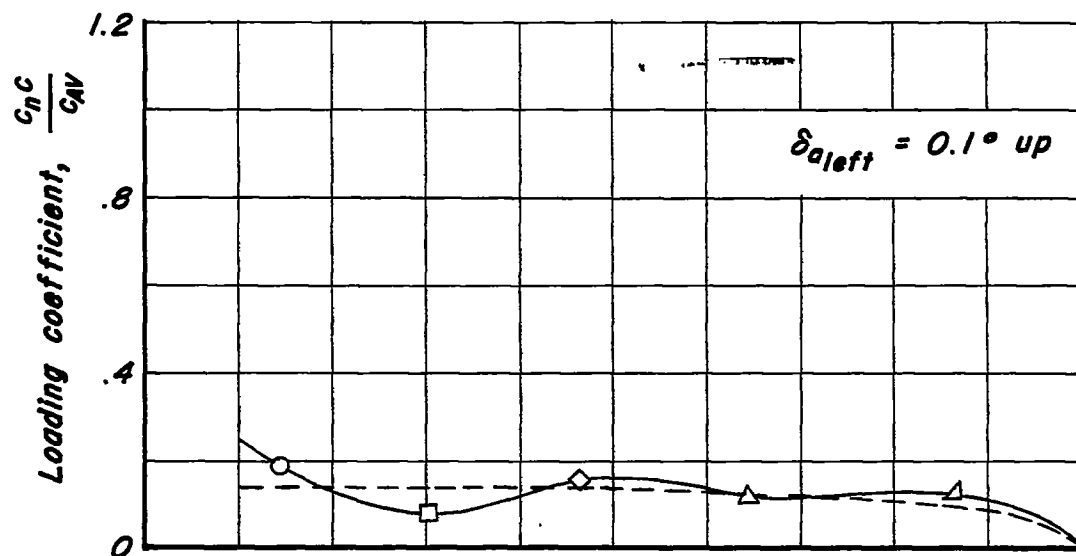


(c) $C_{N_0} = 0.6$; $M_n = 0.70$

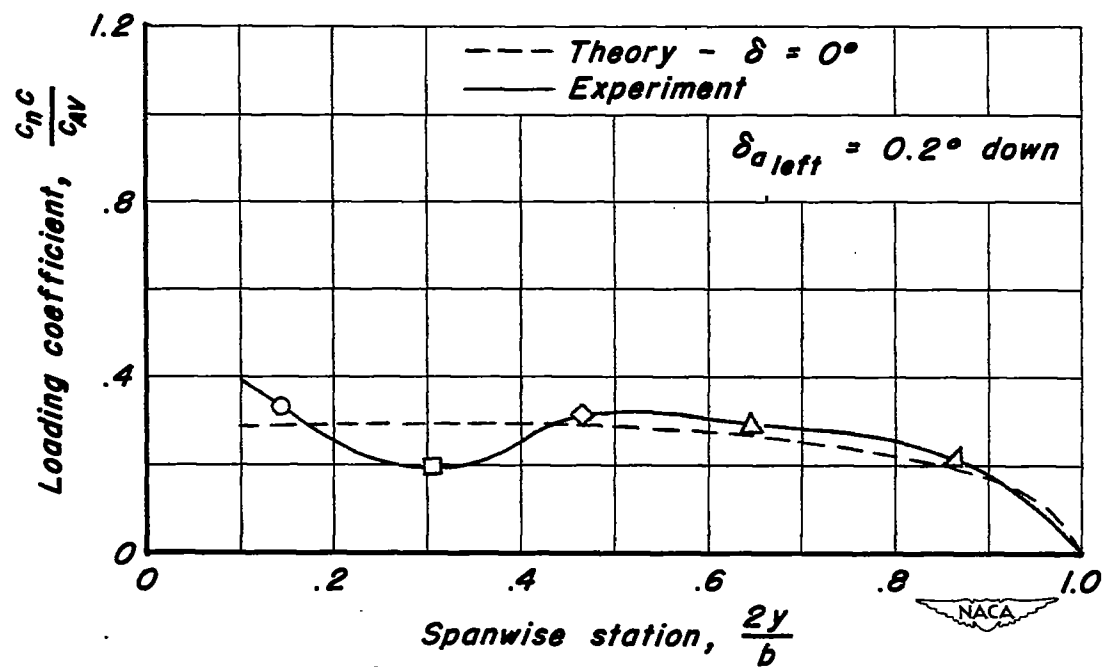


(d) $C_{N_0} = 0.8$; $M_n = 0.70$

Figure 9. - Continued.



(e) $C_{N_0} = 0.2$; $M_n = 0.87$



(f) $C_{N_0} = 0.4$; $M_n = 0.87$

Figure 9. - Continued.

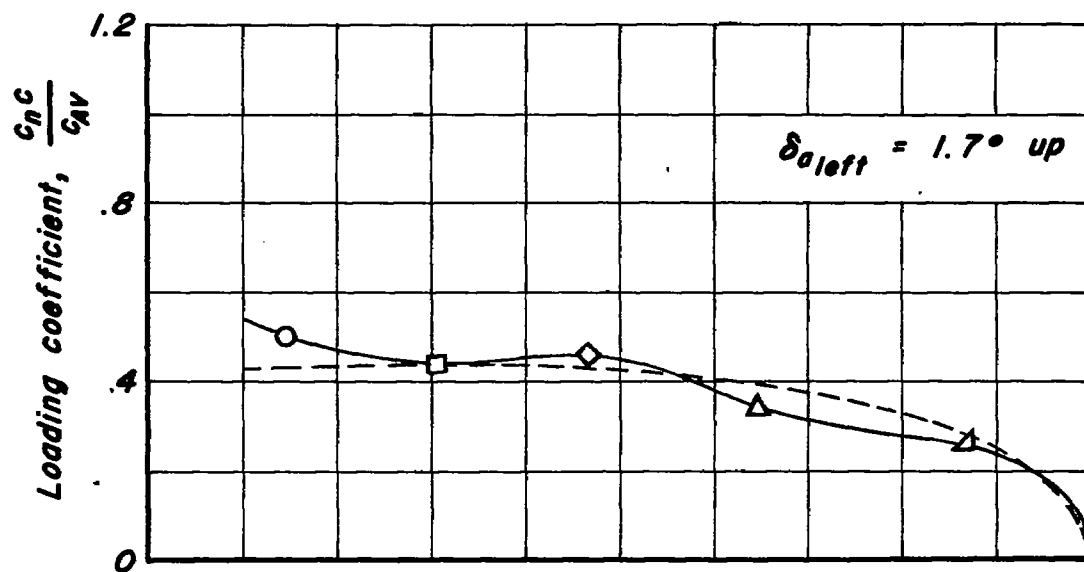
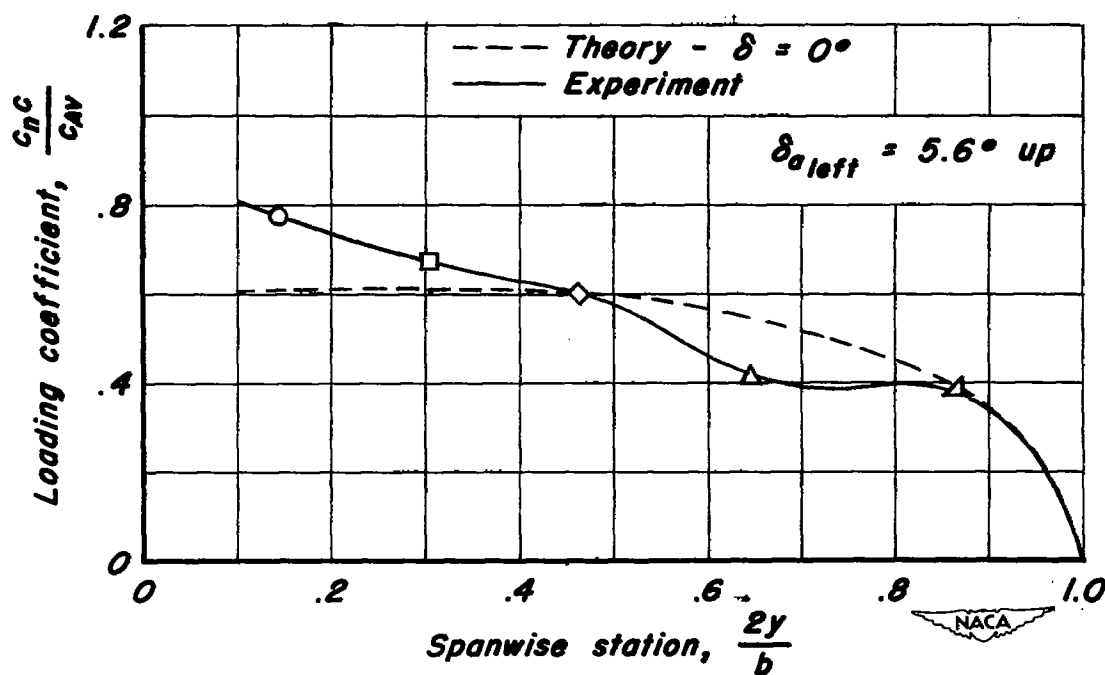
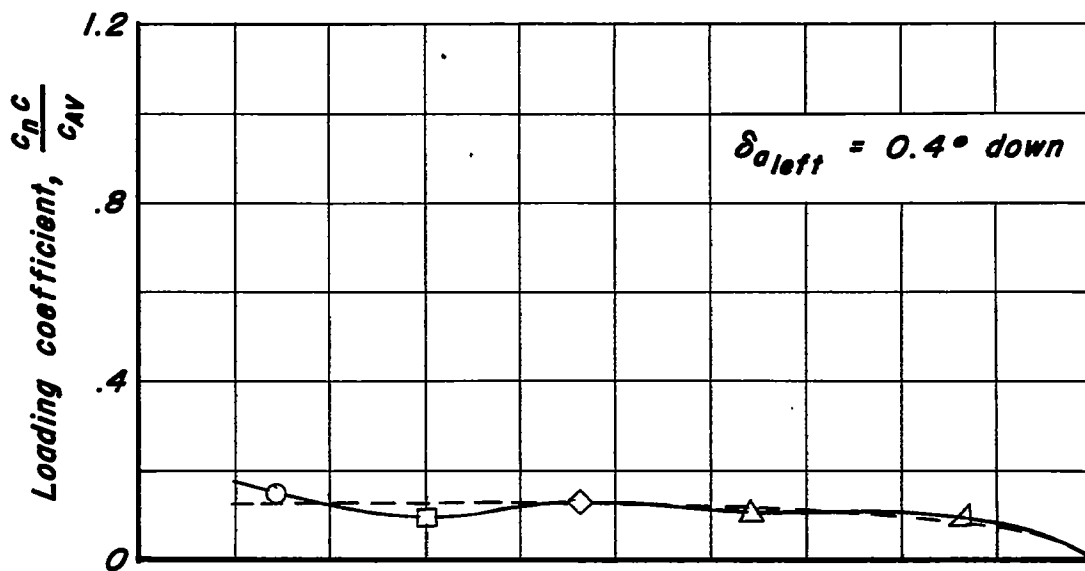
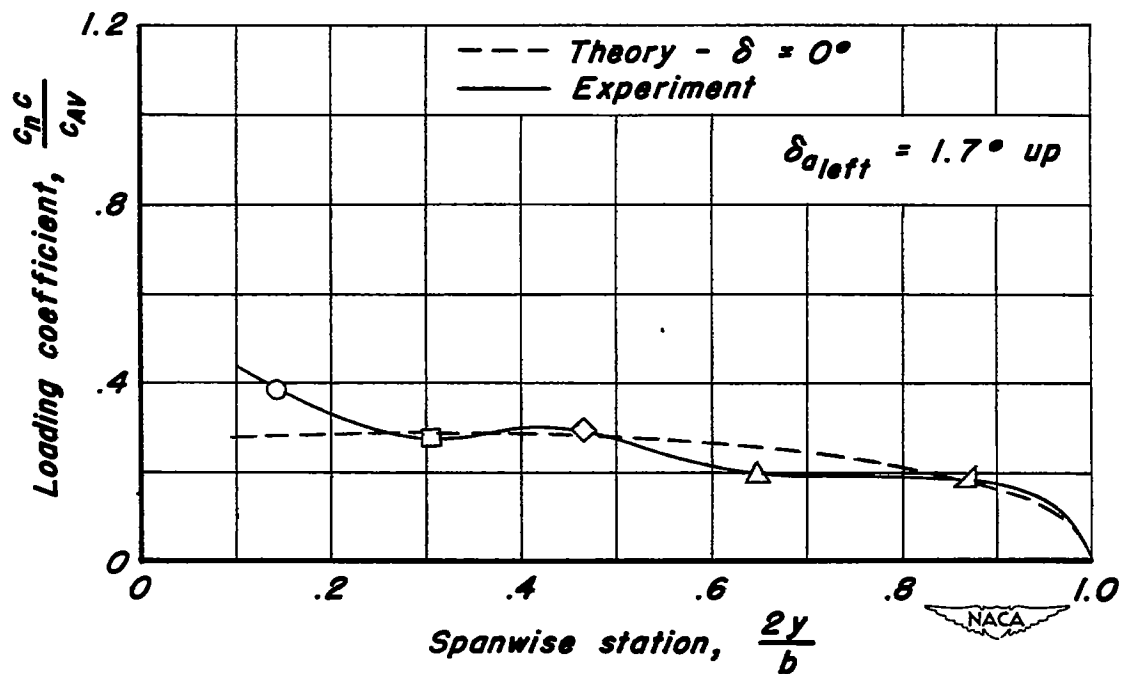
(g) $C_{N_0} = 0.6$; $M_n = 0.87$ (h) $C_{N_0} = 0.8$; $M_n = 0.87$

Figure 9. - Continued.

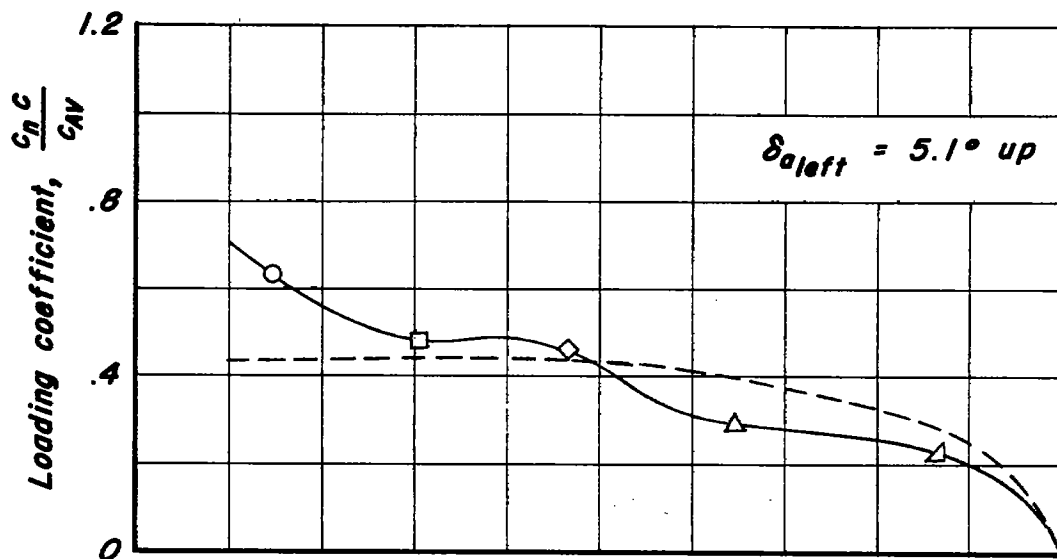


(i) $C_{N_0} = 0.2$; $M_n = 0.90$

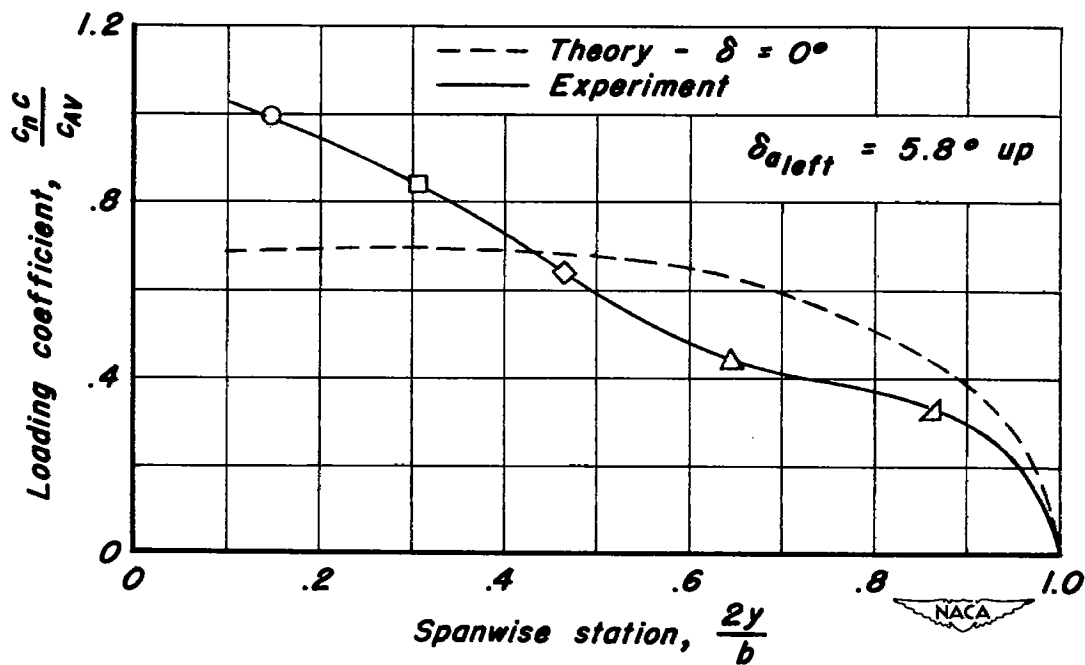


(j) $C_{N_0} = 0.4$; $M_n = 0.90$

Figure 9. - Continued.



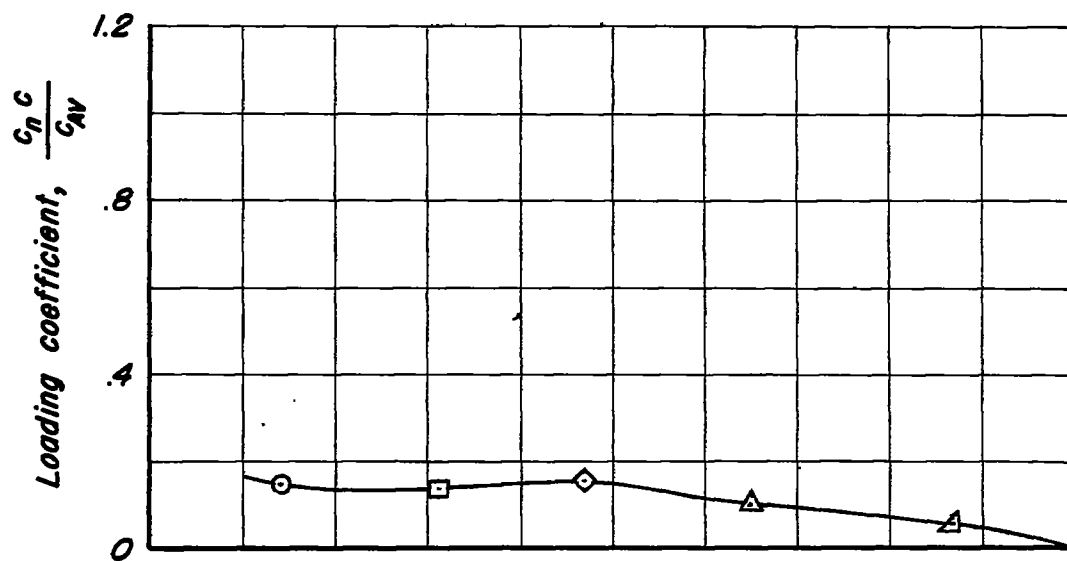
(k) $C_{N_0} = 0.6$; $M_n = 0.90$



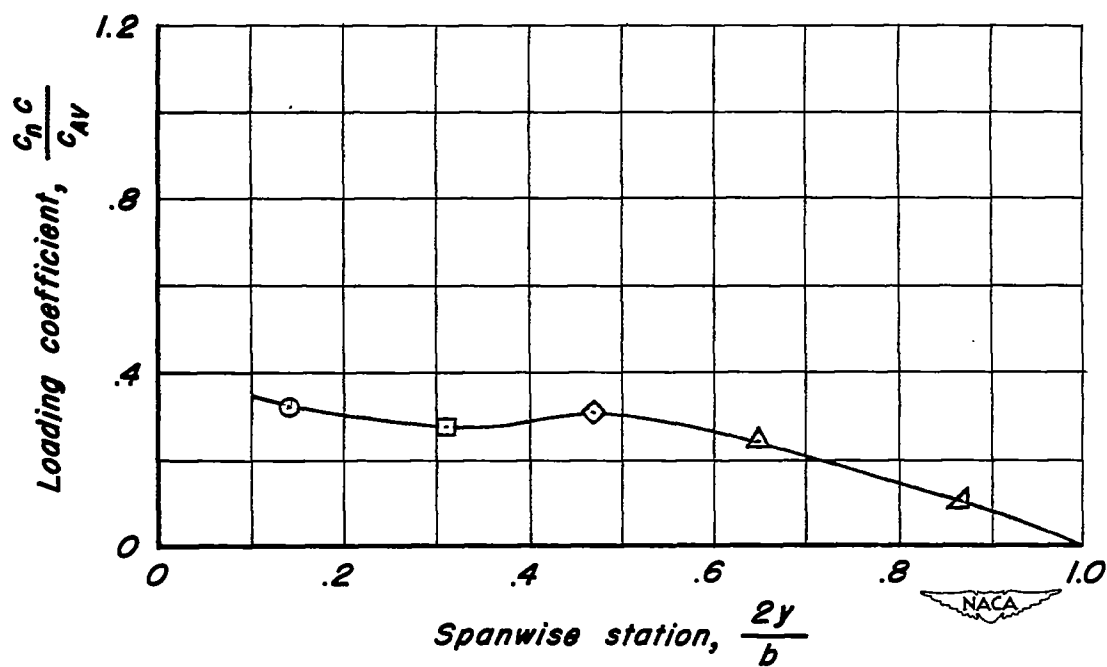
(l) $C_{N_0} = 0.8$; $M_n = 0.90$

Figure 9. - Continued.

CONFIDENTIAL

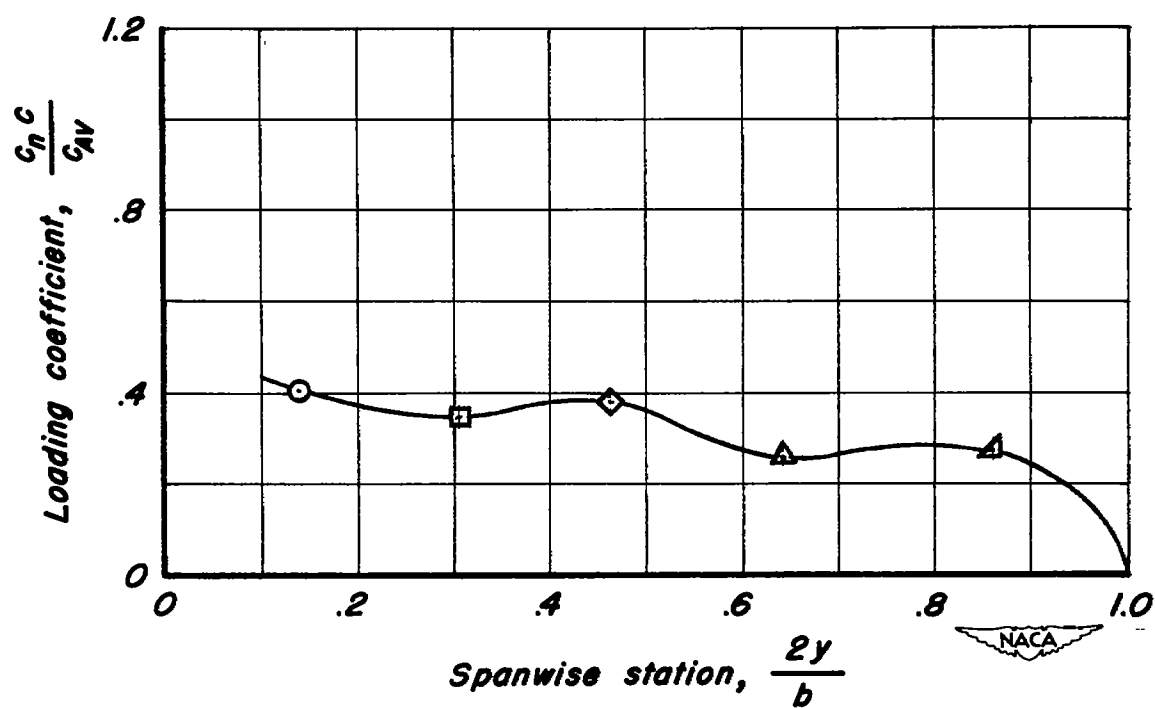


(m) $C_{N_0} = 0.17$; $M_n = 0.97$



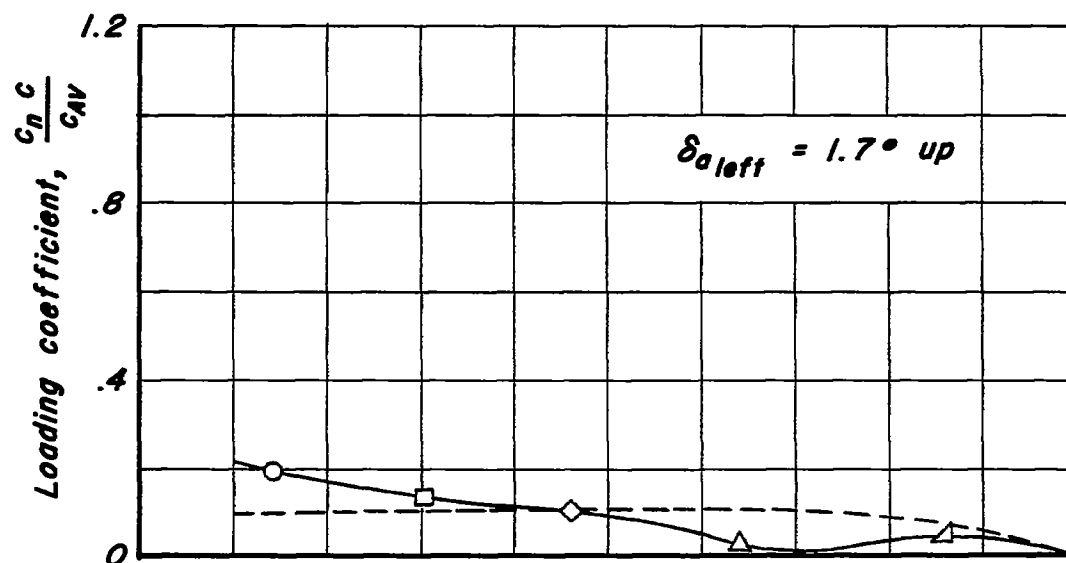
(n) $C_{N_0} = 0.34$; $M_n = 0.97$

Figure 9.- Continued.

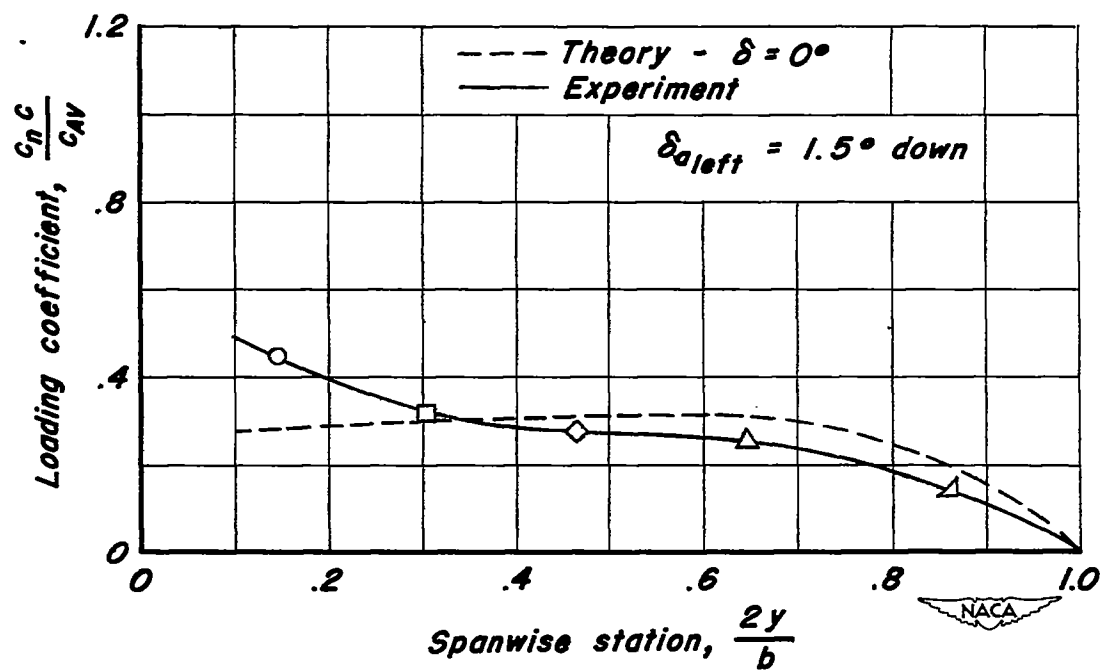


(a) $C_{N_0} = 0.47$; $M_n = 0.97$

Figure 9.- Continued.

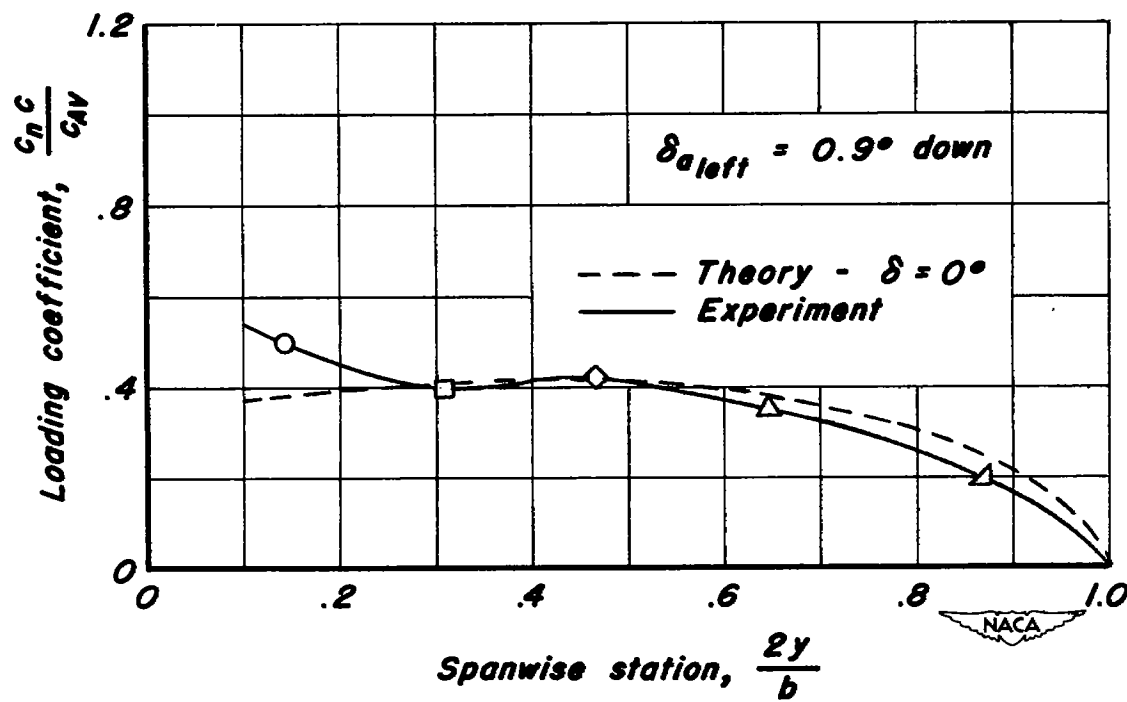


(p) $C_{N_0} = 0.2$; $M_n = 1.02$



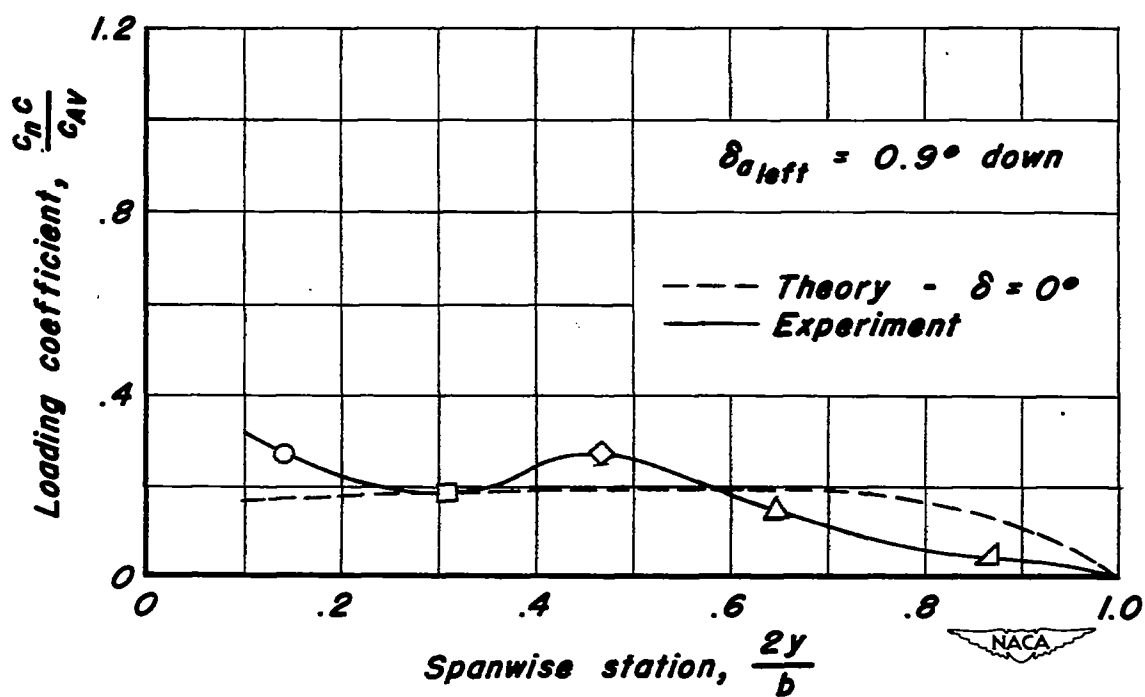
(q) $C_{N_0} = 0.4$; $M_n = 1.02$

Figure 9. - Continued.



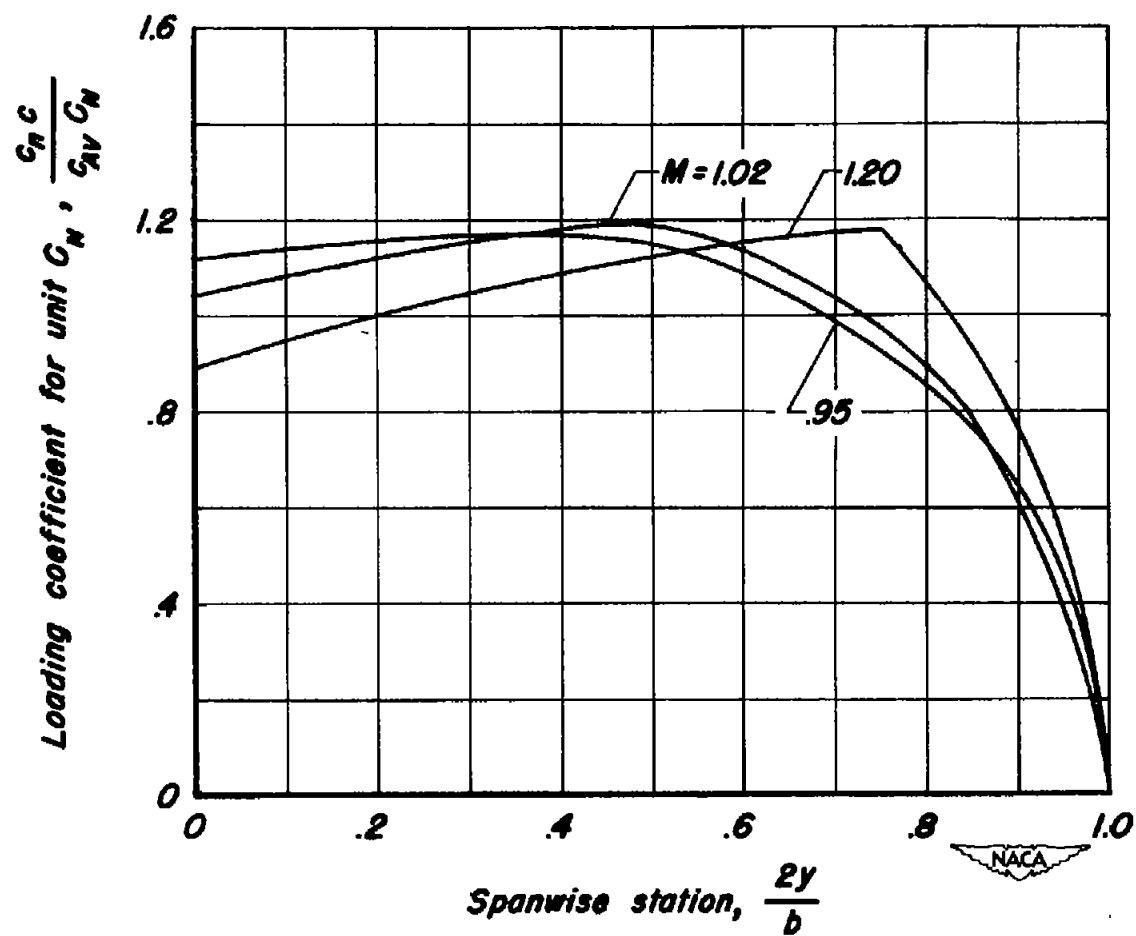
(r) $C_{N_0} = 0.5$; $M_n = 1.02$

Figure 9. - Continued.



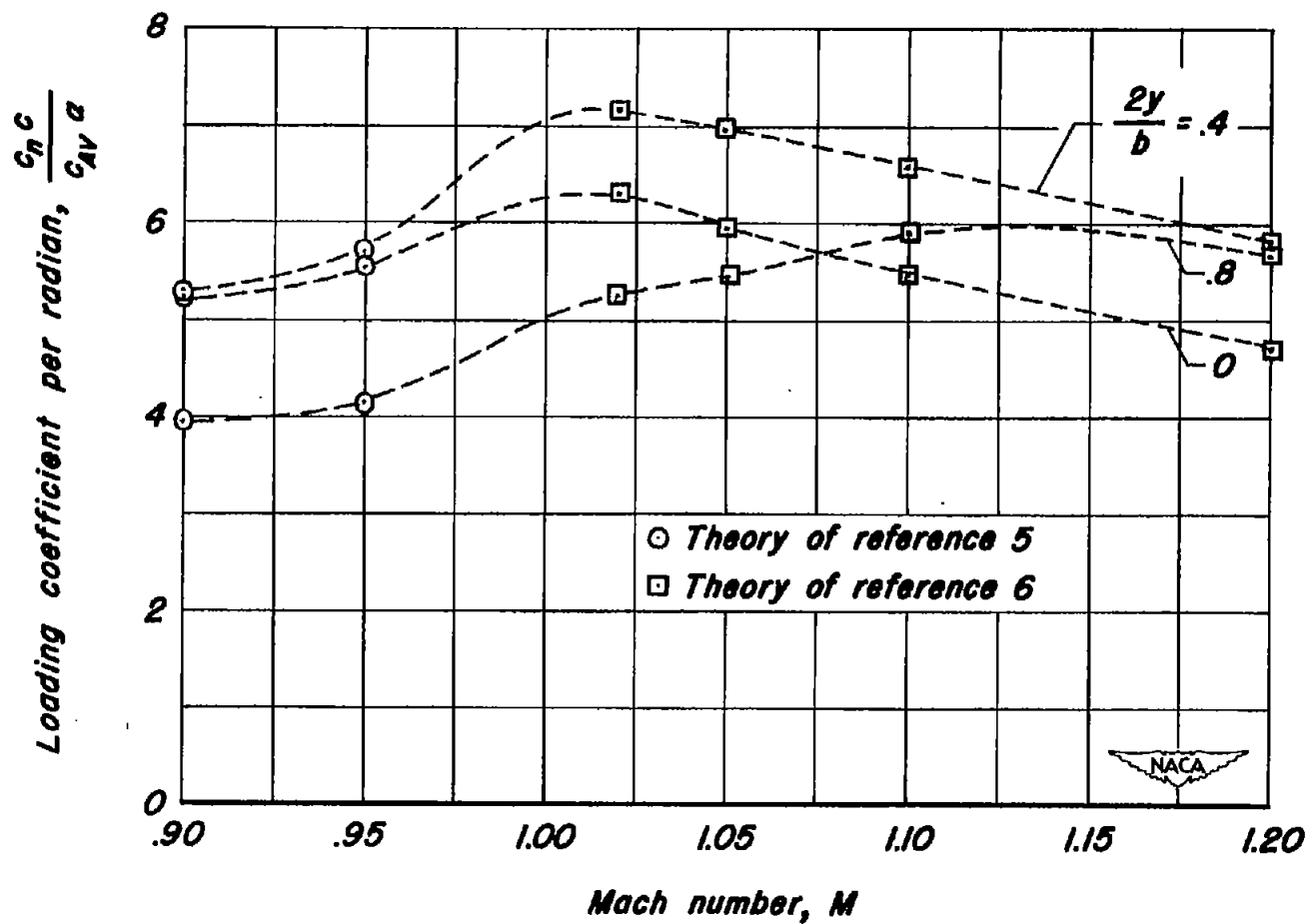
(s) $C_{N_a} = 0.2$; $M_n = 1.11$

Figure 9. - Concluded.



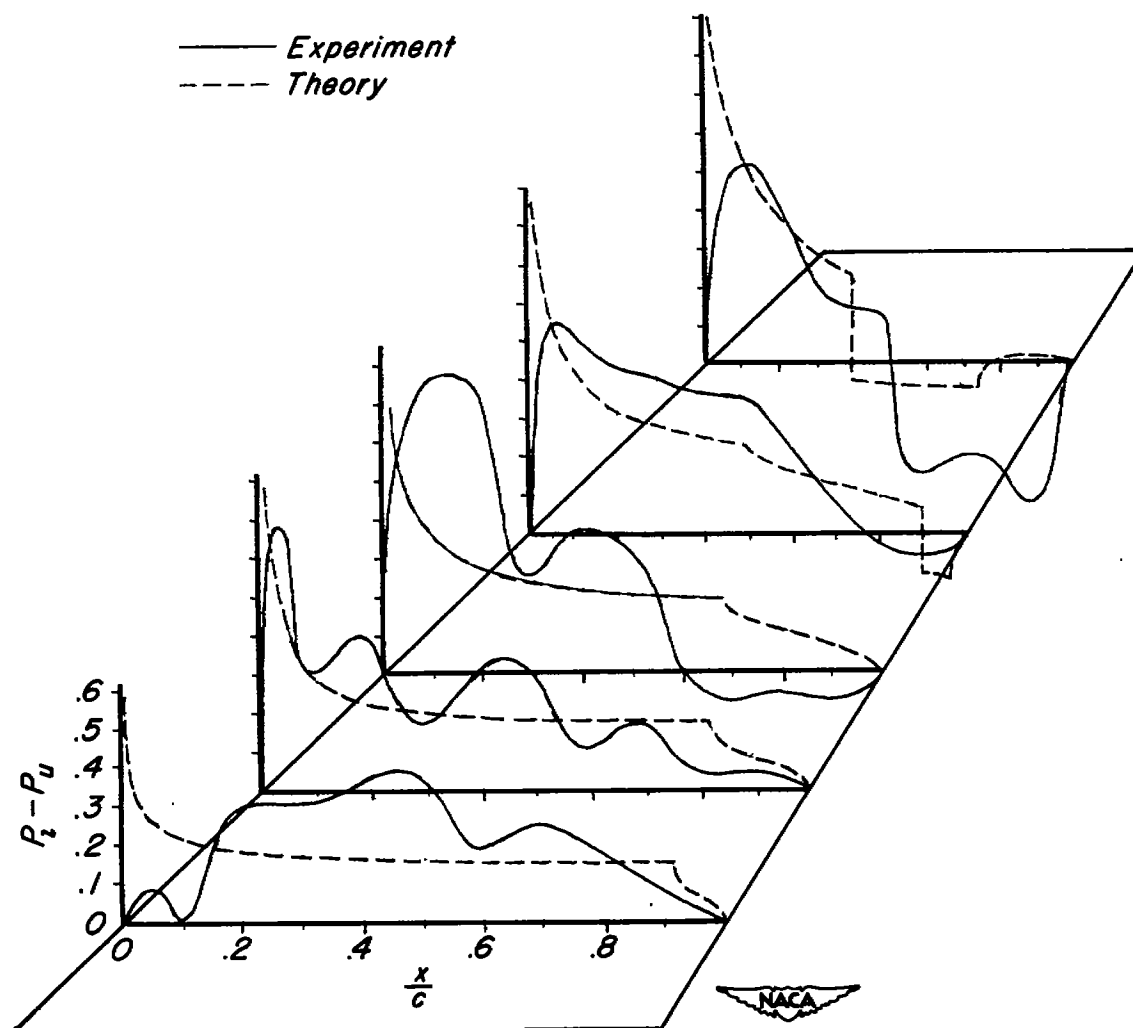
(a) Span load distribution per unit C_N .

Figure 10. - Variation of theoretical additional loading through the transonic range.



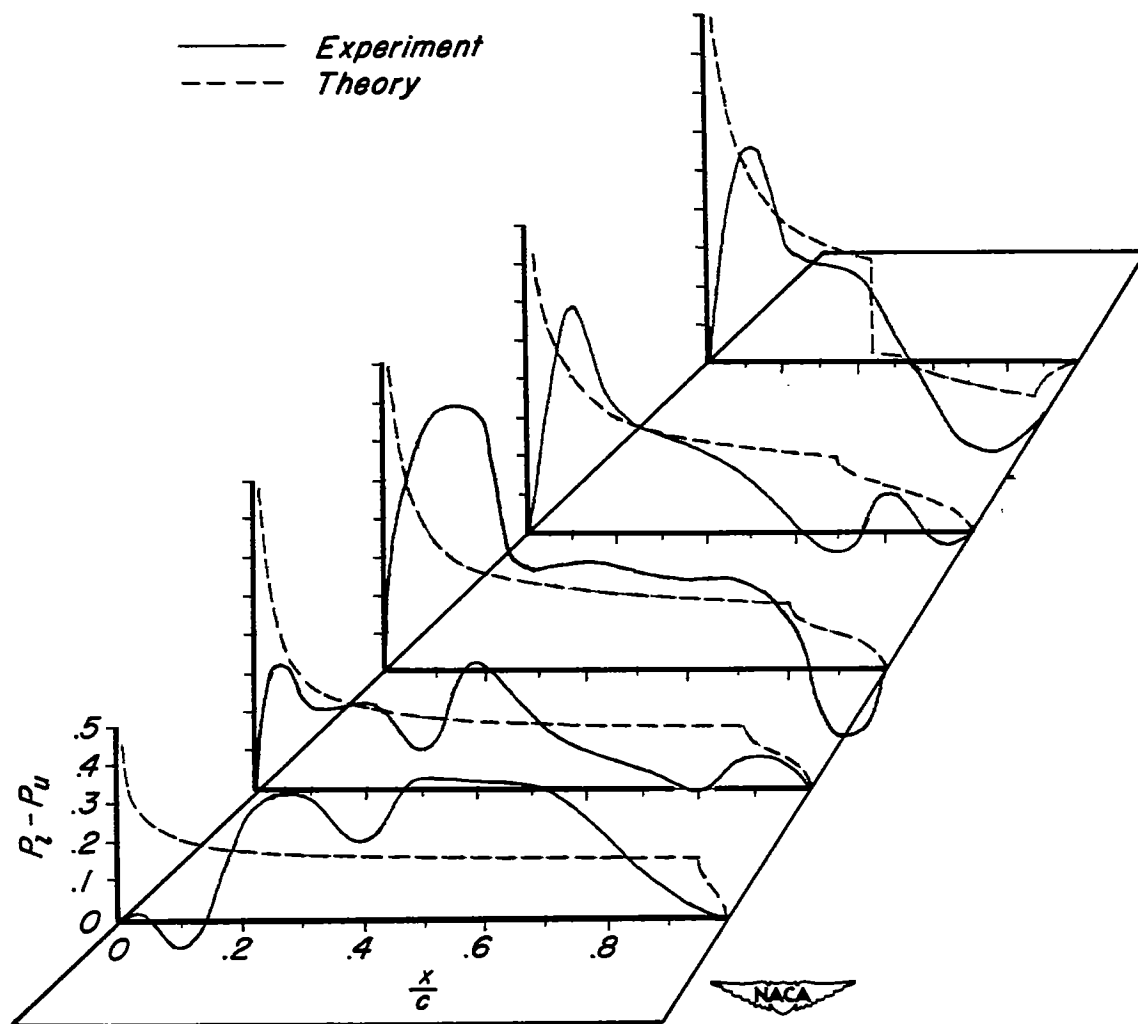
(b) Variation of loading with Mach number.

Figure 10.- Concluded.



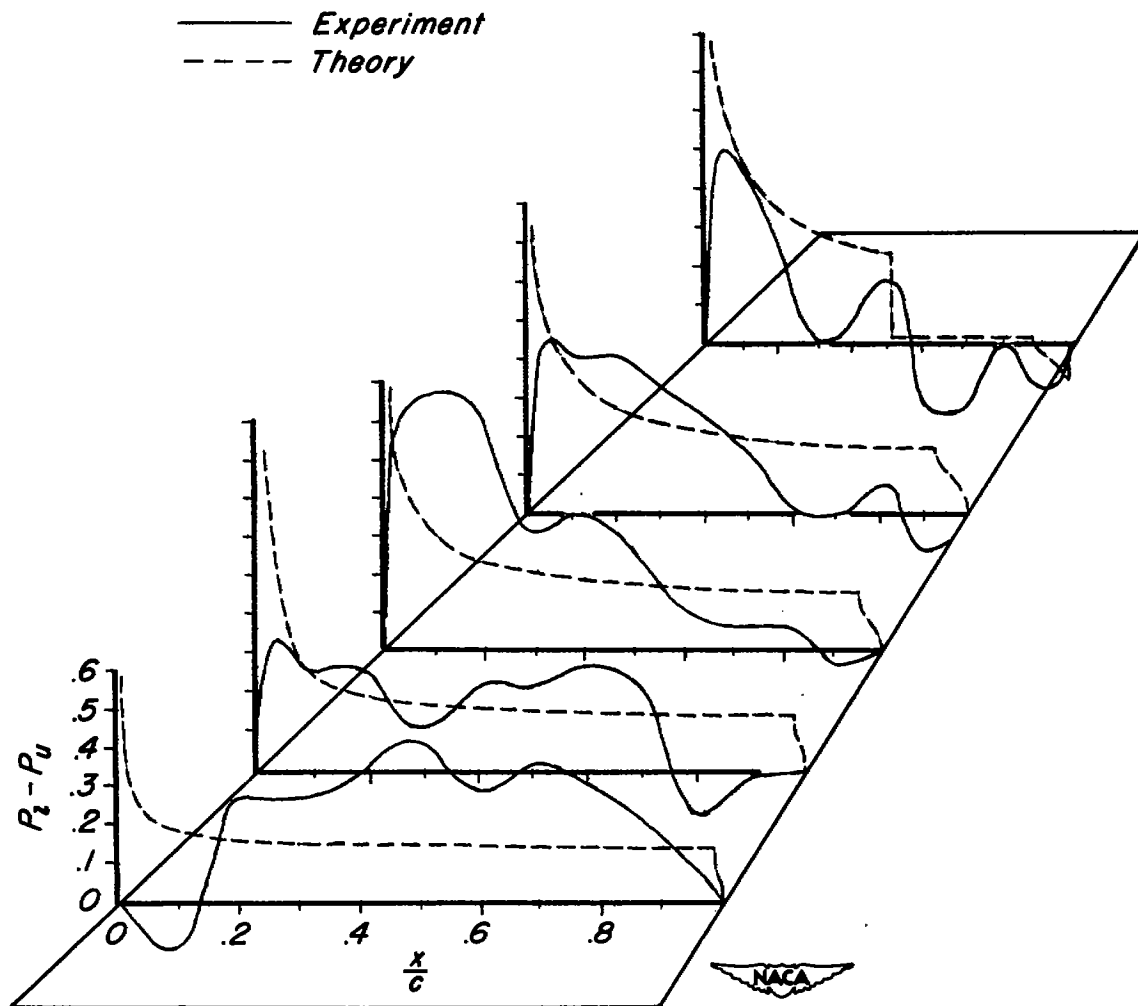
(a) $M = 1.02$; $C_{N_\alpha} = 0.2$

Figure 11.- Comparison of theoretical and experimental chordwise loading at supersonic speeds.



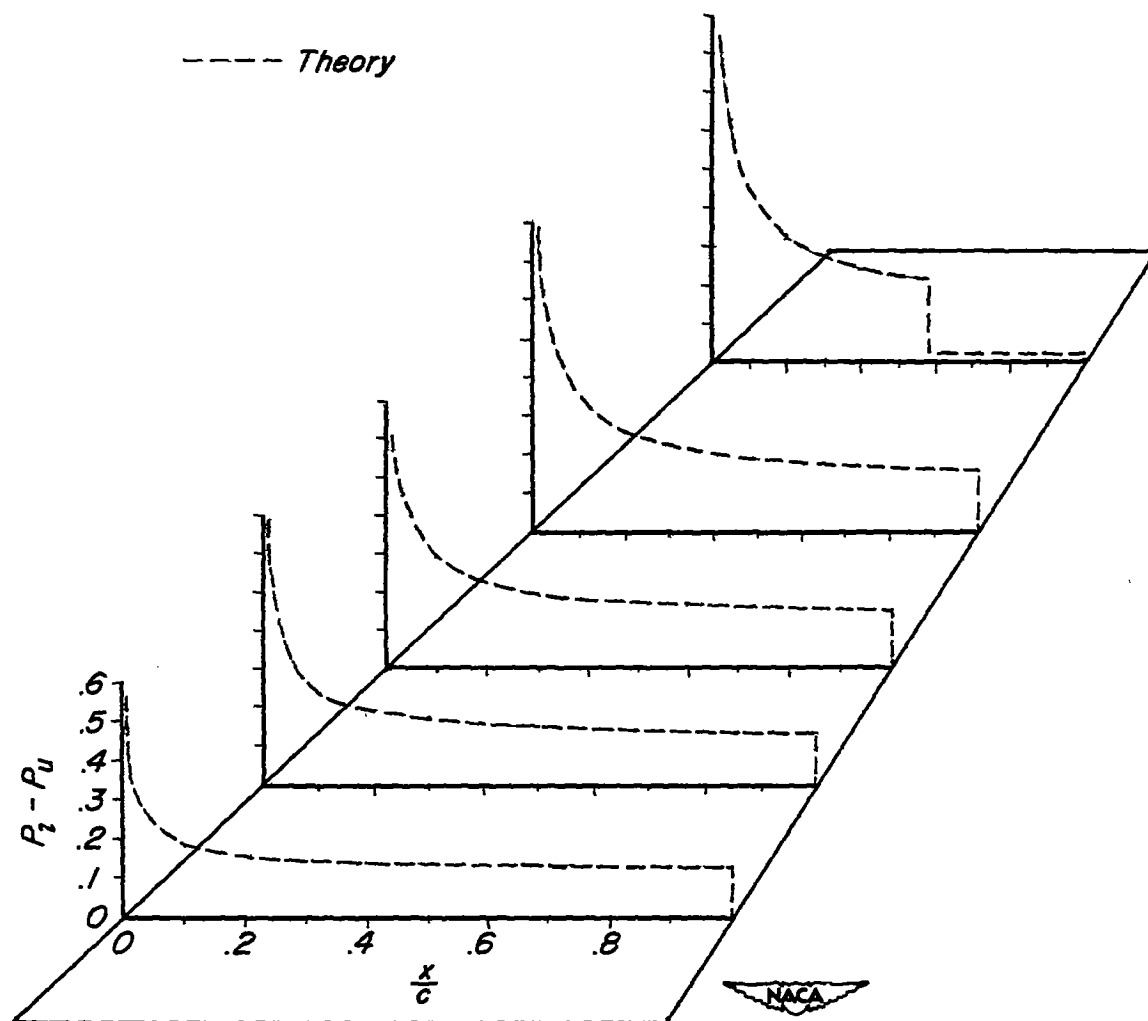
(b) $M = 1.05$; $C_{N_a} = 0.2$

Figure 11.—Continued.



(c) $M = 1.10$; $C_{N_a} = 0.2$

Figure 11.- Continued.



(d) $M = 1.20$; $C_{Na} = 0.2$

Figure 11.- Concluded.

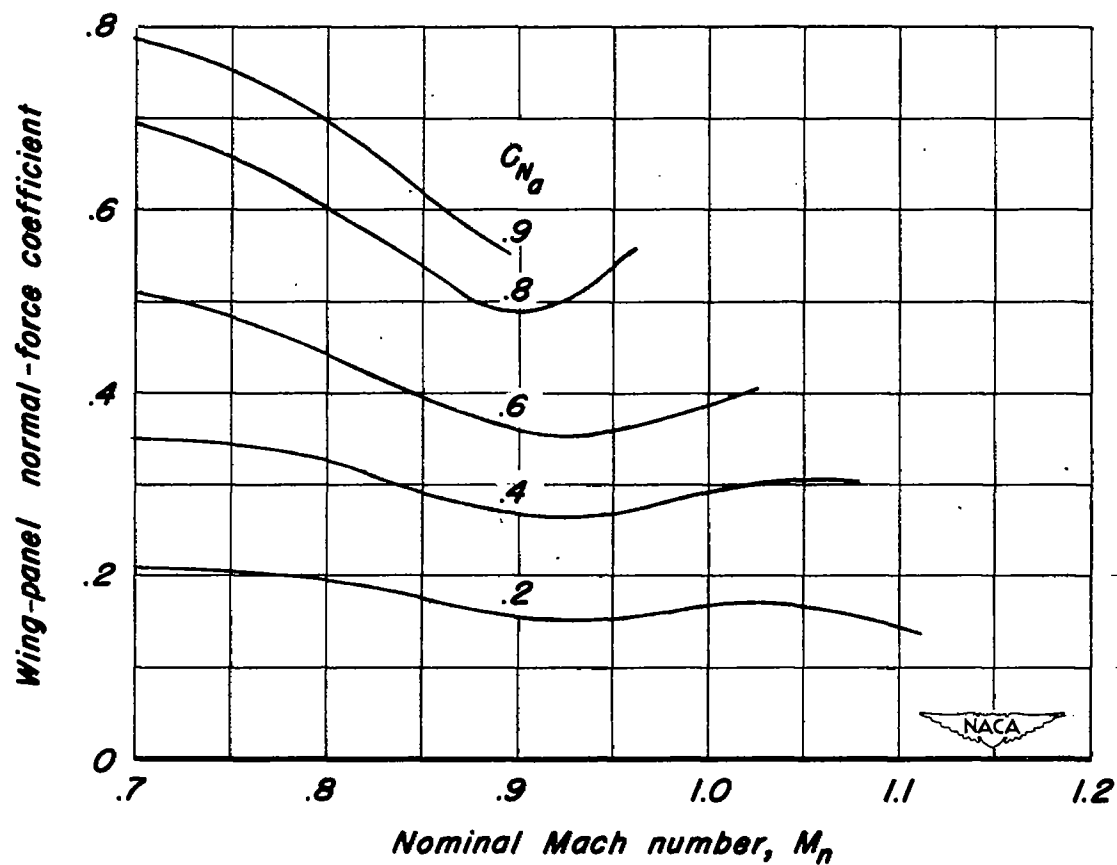


Figure 12.- Load carried by wing panel.

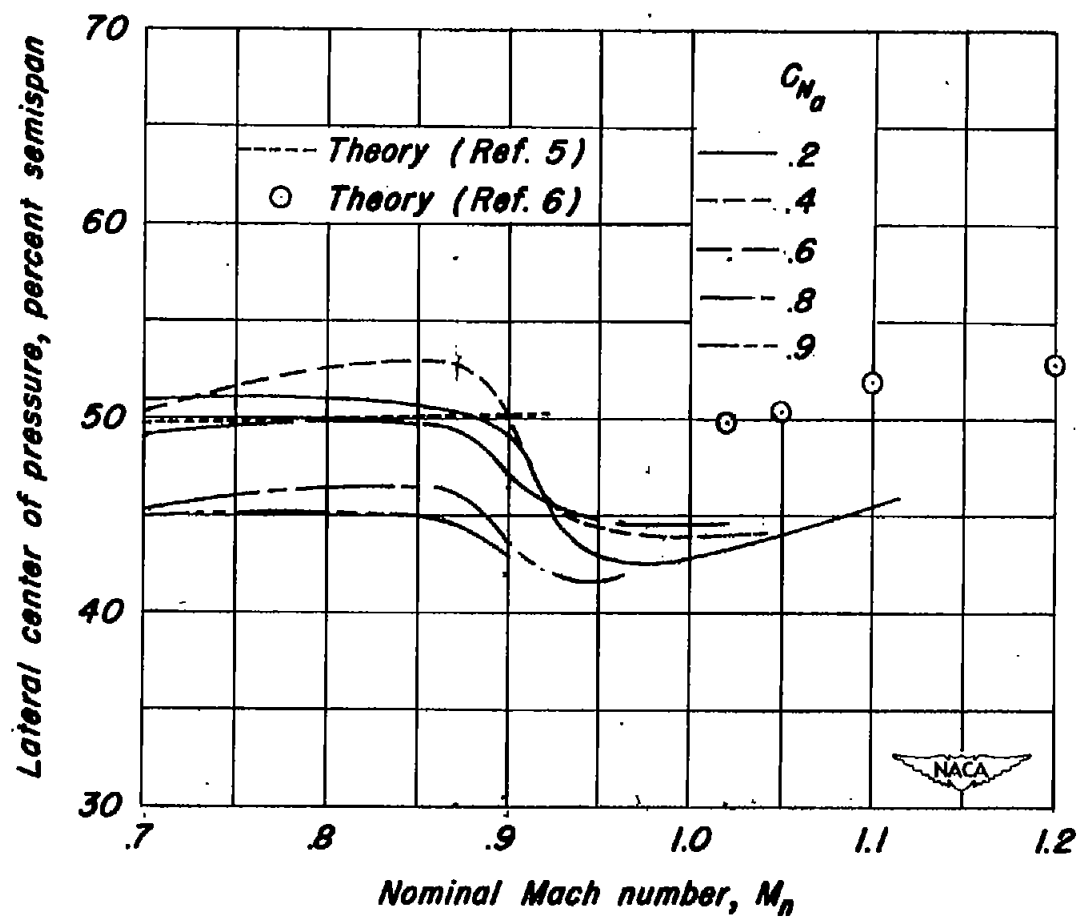


Figure 13.— Lateral center of pressure of load on panel.

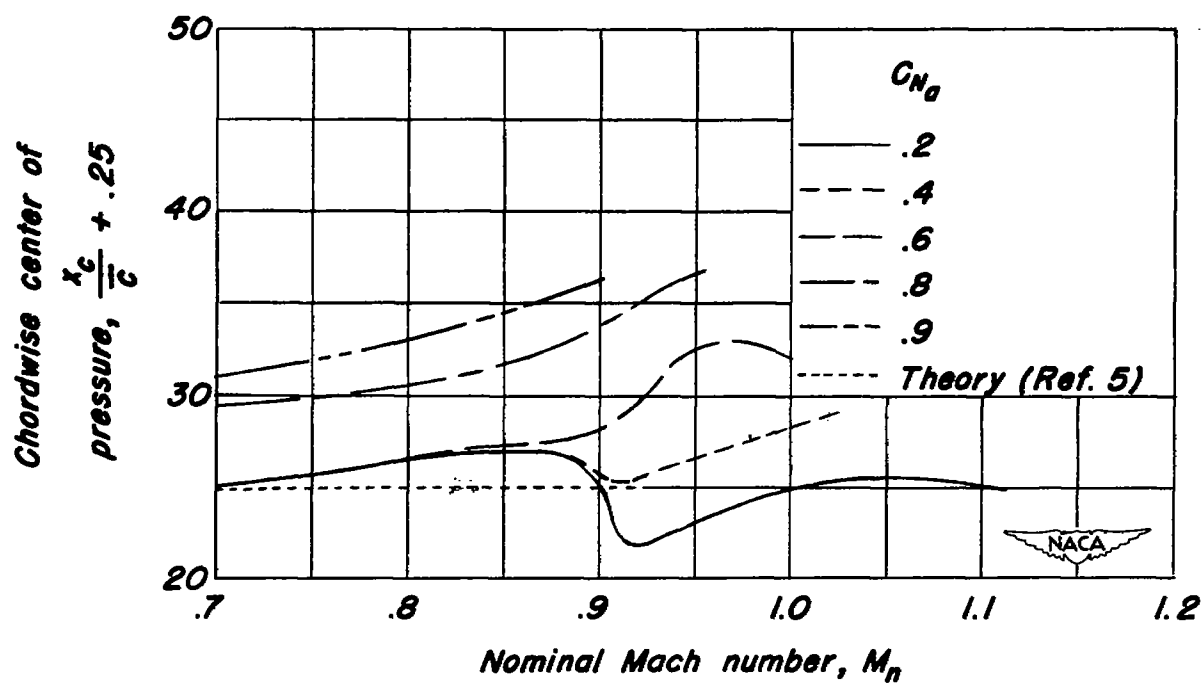


Figure 14.- Chordwise center of pressure of load on panel.

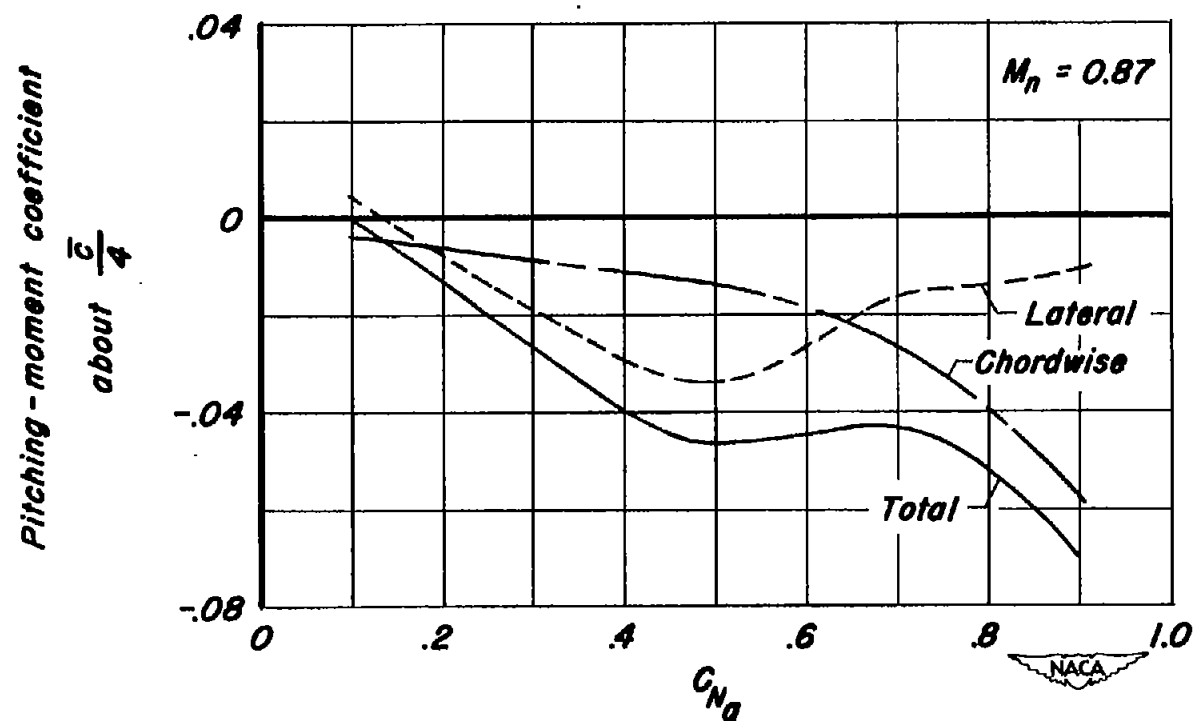
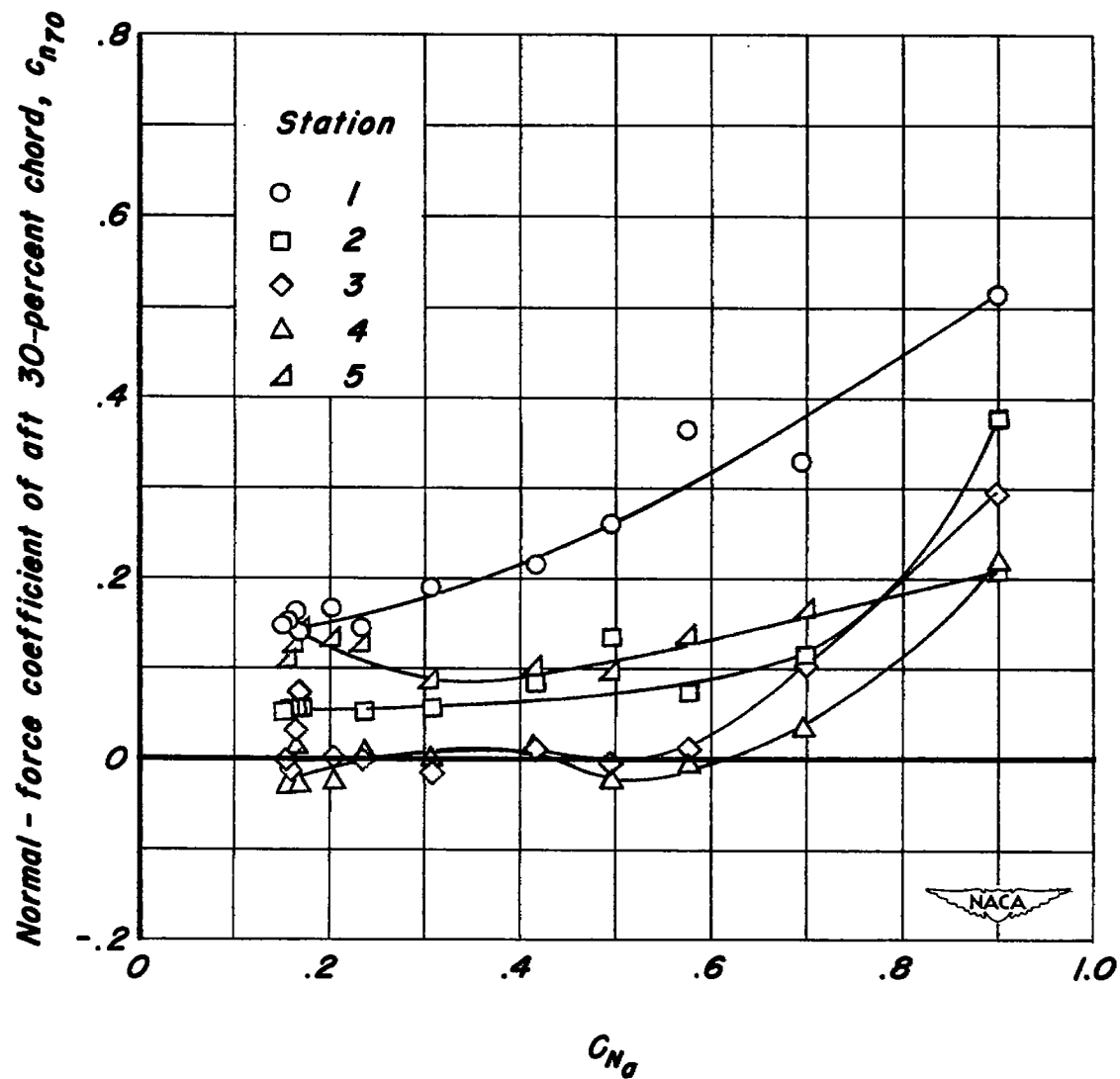
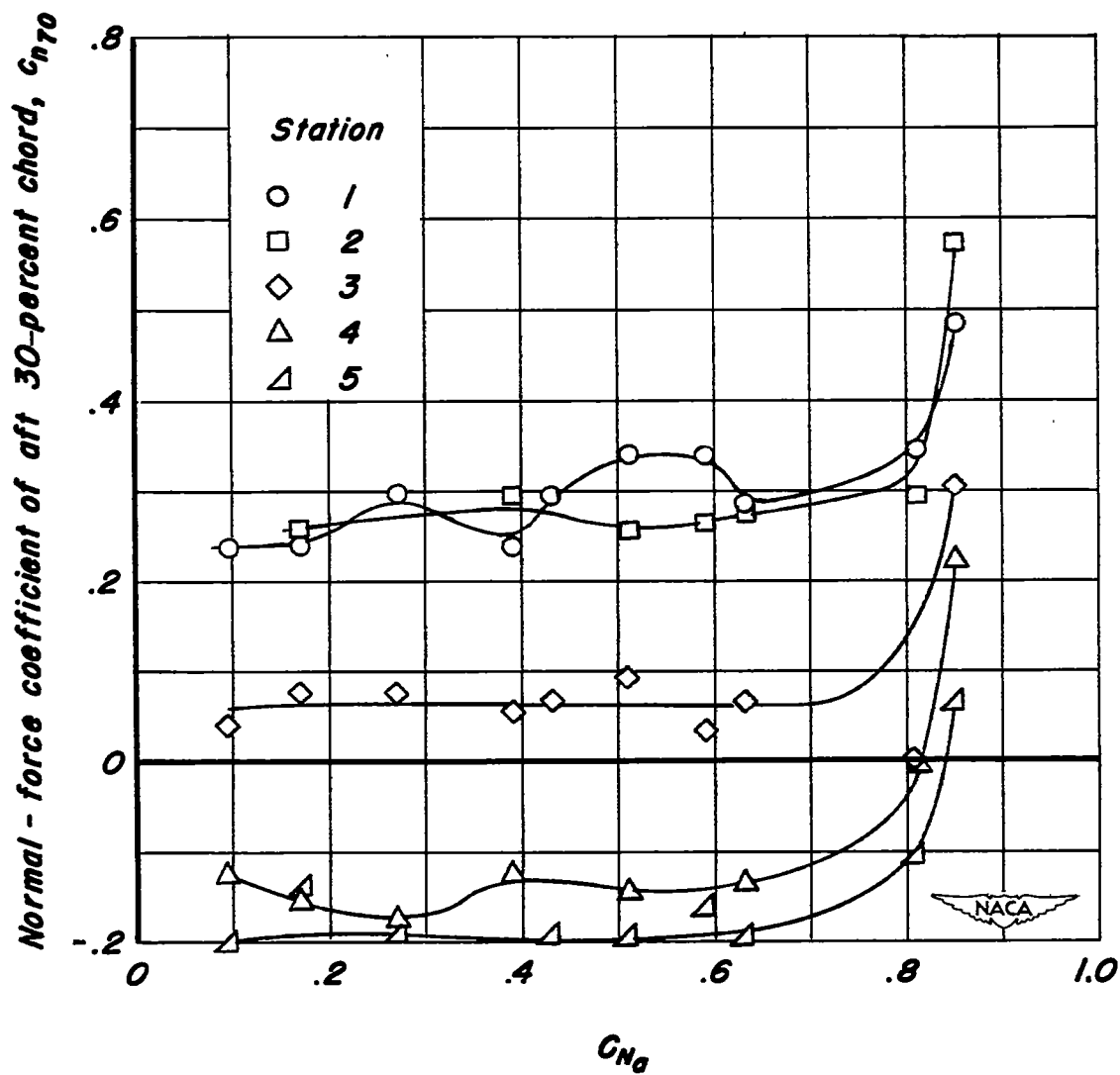


Figure 15.—Contributions of the lateral and chordwise variations of load on the panel to total panel pitching moment.



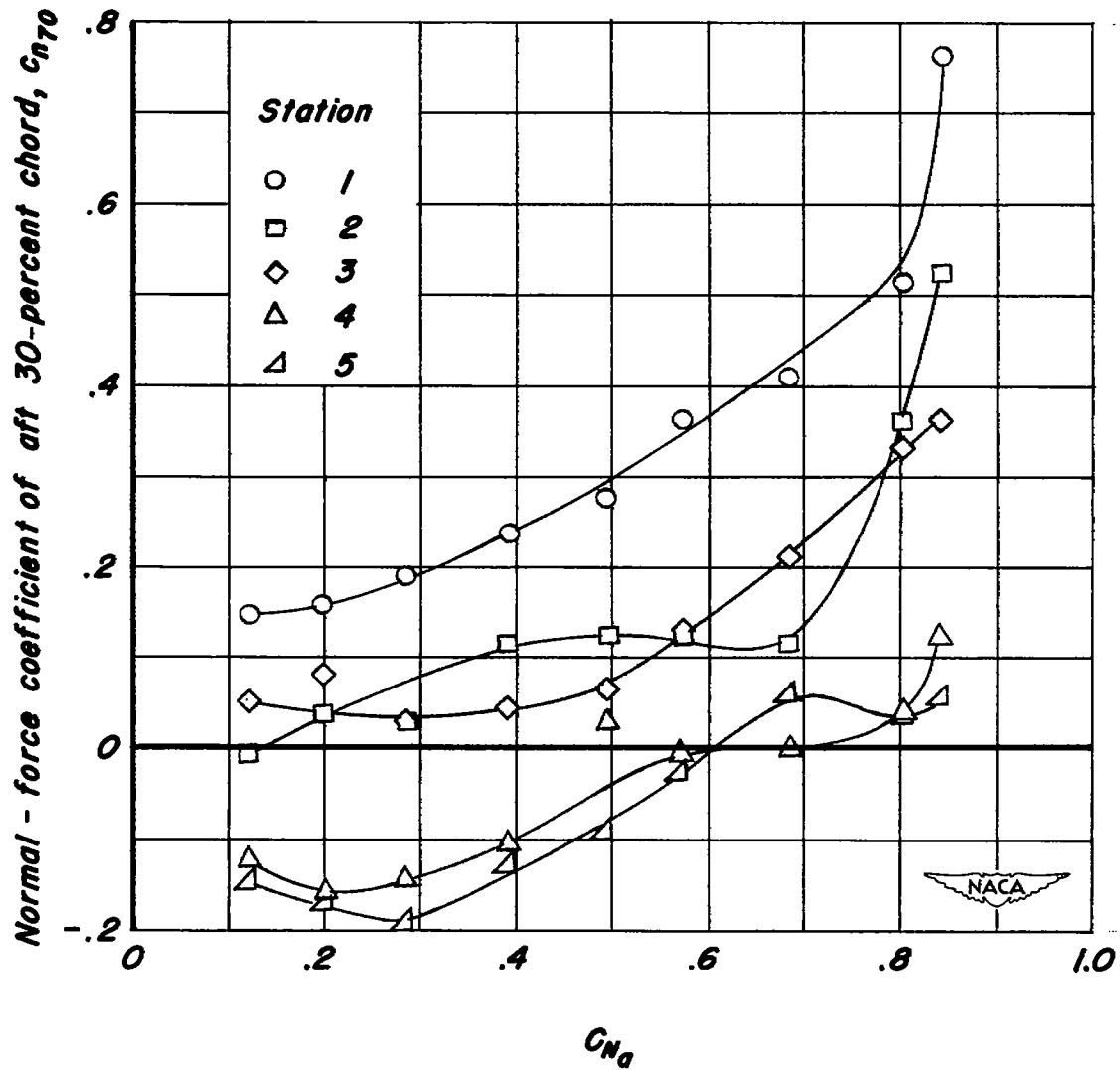
(a) $M_n = 0.70$

Figure 16. - Trailing - edge loads.



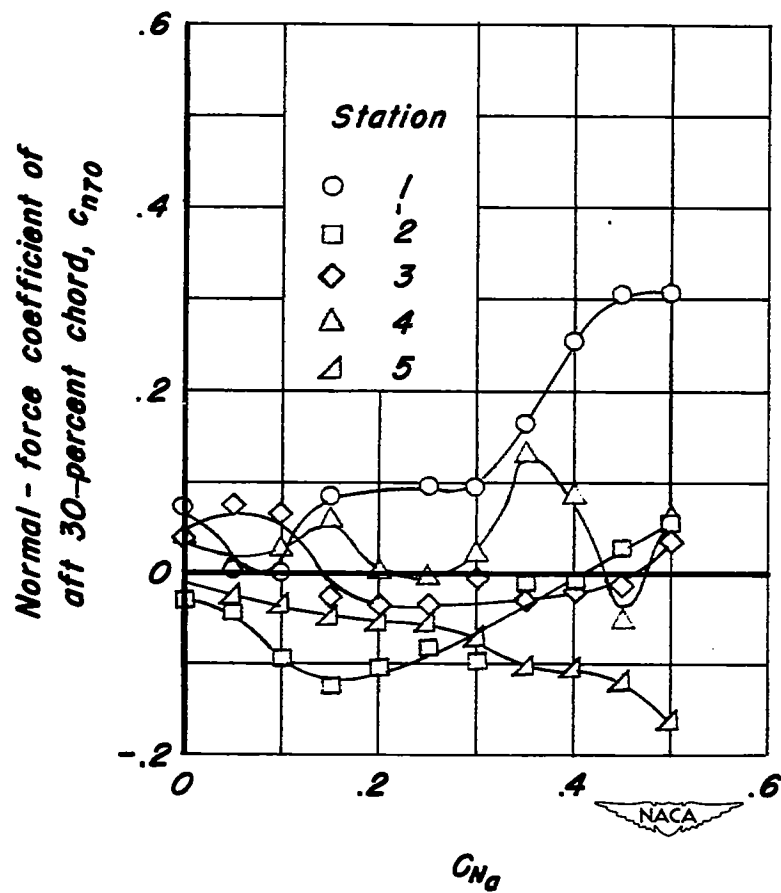
(b) $M_n = 0.87$

Figure 16. - Continued.



(c) $M_n = 0.90$

Figure 16. - Continued.



(d) $M_n = 1.02$

Figure 16. - Concluded.

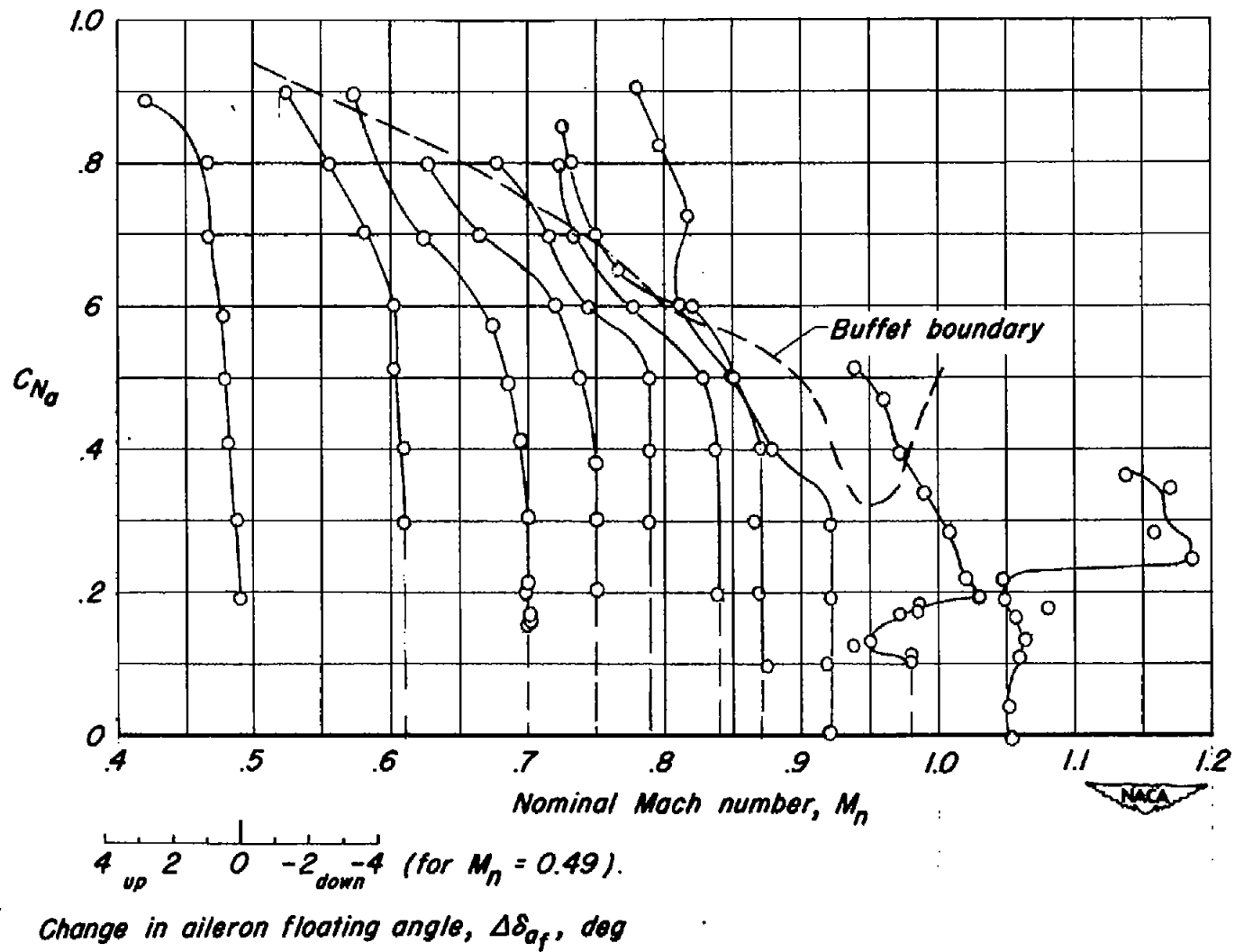


Figure 17.- Aileron floating characteristics.



(a) $C_{N_a} = 0.05$



(b) $C_{N_a} = 0.19$

Figure 18.— Tuft and aileron behavior at $M = 1.10$.

SECURITY INFORMATION

~~CONFIDENTIAL~~

NASA Technical Library



3 1176 01434 8313

~~CONFIDENTIAL~~